

Dynamics of Resolved Polar Clouds

Thesis by
Xiyue Zhang

In Partial Fulfillment of the Requirements for the
Degree of
Doctor of Philosophy

The logo for the California Institute of Technology (Caltech), featuring the word "Caltech" in a bold, orange, sans-serif font.

CALIFORNIA INSTITUTE OF TECHNOLOGY
Pasadena, California

2018
Defended May 15 2018

© 2018

Xiyue Zhang

ORCID: 0000-0002-6031-7830

All rights reserved except where otherwise noted

“If the clouds could be rationally and convincingly explained, without recourse to superstition or prejudice, then so could anything else in nature, for they represented the most extreme manifestation of the ungraspable.”

– Richard Hamblyn, *The Invention of Clouds*

ACKNOWLEDGEMENTS

First and foremost, I thank my family, especially my parents, for their unconditional support while I am far away from home.

I am extremely lucky to have met Marcelo during our time at Caltech. His company made graduate school more enjoyable and worthwhile. Thank you!

I would like to thank my advisor Tapio Schneider for his guidance, support, and encouragement throughout my time at Caltech. He will always be someone I look up to in my career. I thank Simona Bordoni for being the female role model for many of us. I thank Andy Thompson for introducing me to the seals. It was great fun working on that project. I want to thank the rest of my committee members João Teixeira, and John Seinfeld for their helpful discussions.

This thesis would not have been possible without the help from friends and colleagues in Tapio's group, especially Kyle and Colleen who developed PyCLES, and Zhihong who always has answers to my questions. I am grateful to all the group members I have interacted and shared adventures with throughout the years.

I thank Ho-Hsuan and Qiong who entered ESE at the same time with me. I enjoyed our countless discussions and sharing our struggles: I learned so much from you. I thank Bettina for her discussion and support as well, and especially for taking me to the backstage of the Hollywood Bowl. I wish all of you the best in your next chapters!

I thank Gerard Roe and Cecilia Bitz for introducing me to the field of climate science. Your advice and support have gone beyond my time at UW.

Last but not least, I want to thank my friends from home and abroad, especially Rita and Jessica for always being there. I am grateful to my friends from Svalbard, who taught me how to knit.

The simulations in this thesis were performed on ETH Zurich's EULER computing clusters.

ABSTRACT

The polar regions have been experiencing rapid warming and ice loss as greenhouse gas concentrations have risen. The projected warming in the Arctic varies significantly across climate models, part of which is attributed to polar cloud feedbacks. This thesis addresses the question of what drives the changes in polar clouds as the climate warms, using a large eddy simulation (LES) model. LES is a powerful high-resolution model that resolves the most energetic turbulence relevant for clouds. First, we focus on the Arctic boundary layer clouds through three observation based case studies. The cloud and boundary layer characteristics simulated by the LES agree reasonably well with observations and model intercomparisons. We found that during polar night over sea ice, cloud water path increases with temperature and free-tropospheric relative humidity, but it decreases with inversion strength across the cloud top. Most of these changes can be explained by a mixed-layer model. The strength of the estimated positive cloud longwave feedback largely depends on the cloud top inversion strength. Next, we extend the LES domain to cover the entire polar troposphere, and use output from an idealized GCM as forcing to drive the LES. This novel framework allows changes in the large-scale circulation to be parameterized in the LES. The simulated seasonal cycle of liquid clouds resembles observations. In a warmer climate, there is a significant decrease of the low-level liquid clouds during summer and autumn. In spring and winter, liquid clouds increase at all levels. Both the liquid and ice cloud tops rise as the climate warms. Offline radiative transfer calculations estimate a positive cloud feedback that is dominated by longwave feedback.

PUBLISHED CONTENT AND CONTRIBUTIONS

Zhang, X., Thompson, A. F., Flexas, M. M., Roquet, F. & Bornemann, H. Circulation and meltwater distribution in the Bellingshausen Sea: From shelf break to coast. *Geophysical Research Letters*, 43: 6402-6409. DOI: 10.1002/2016GL068998 (2016).

X.Z. participated in the conception of the project, analyzed the data, and participated in the writing of the manuscript.

All contents are reprinted with the permission of the American Geophysical Union (copyright holder).

TABLE OF CONTENTS

Acknowledgements	iv
Abstract	v
Published Content and Contributions	vi
Table of Contents	vii
List of Illustrations	ix
List of Tables	xvi
Chapter I: Introduction	1
1.1 Polar Clouds and Climate	1
1.2 Modeling Approach	2
1.3 Thesis Outline	3
Chapter II: Arctic Stratocumulus in Large Eddy Simulations and a Mixed- layer Model	4
2.1 Abstract	4
2.2 Introduction	4
2.3 Model Descriptions	6
2.4 Experimental Setup	10
2.5 Results	13
2.6 Discussion and Conclusions	29
2.7 Appendix: List of Symbols	31
2.8 Appendix: MLM entrainment parameterization	32
Chapter III: Case Studies of Arctic Boundary Layer Clouds	34
3.1 Abstract	34
3.2 Introduction	34
3.3 LES Setup	35
3.4 SHEBA Case Study	36
3.5 M-PACE Case Study	39
3.6 Conclusions	44
Chapter IV: Idealized Climate Change of Polar Clouds under Consistent Large-Scale Forcing	48
4.1 Abstract	48
4.2 Introduction	48
4.3 Model Setup	51
4.4 Results	56
4.5 Discussion	68
4.6 Conclusions	74
Chapter V: Circulation and Meltwater Distribution in the Bellingshausen Sea: From Shelf Break to Coast	76
5.1 Abstract	76
5.2 Introduction	76

5.3 Data	78
5.4 Results	79
5.5 Discussion	84
5.6 Conclusions	86
Chapter VI: Conclusions	87
Bibliography	89

LIST OF ILLUSTRATIONS

<i>Number</i>	<i>Page</i>
1.1 Visible (left) and false color (right) image of the Arctic from the Moderate Resolution Imaging Spectroradiometer (MODIS) on NASA's Terra satellite. The North Pole is at the center left of the image, Greenland is at the bottom, Barents and Kara Sea are on the right. On the false color image, deep blue shows the ocean surface, magenta and red shows sea ice and ice sheet. Light orange and cyan show high and low clouds correspondingly. (NASA images by Robert Simmon and Jesse Allen, based on MODIS data.)	2
2.1 Schematic of the ISDAC-i θ_{li} and q_t initial conditions. The cloud layer is indicated in blue. The BL with height z_i has constant θ_{li} and q_t , where q_t is determined by the relative humidity (blue dotted line) near the surface \mathcal{H}_0 . The BL is capped by an inversion of $\Delta\theta_{li}$, above which potential temperature increases with height at the rate Γ_θ . Relative humidity above the BL, \mathcal{H}_f , does not vary with height, and it is used to determine q_t above z_i	12
2.2 Domain mean profiles of (a) liquid ice potential temperature, (b) total water specific humidity, (c) cloud liquid water specific humidity, and (d) the sum of cloud ice and snow water specific humidity. Black dotted lines are the initial condition profiles. Gray shading shows the LES intercomparison range in Ovchinnikov <i>et al.</i> [32]. The pink dots show the aircraft observations of flight 31 of ISDAC campaign on April 27, 2008. The horizontal lines indicate the 15–85 percentile range for the measurements binned every 50 m.	14
2.3 Timeseries of (top) liquid water path and (bottom) the sum of cloud ice and snow water path. Gray shading shows the LES intercomparison range in Ovchinnikov <i>et al.</i> [32]. The pink bars show the range of observed values estimated using ISDAC flight 31 data in Figure 2.2.	15

2.4	ISDAC-i domain mean profiles of (a) liquid ice potential temperature, (b) total water specific humidity, (c) liquid water specific humidity, and (d) the sum of cloud ice and snow water specific humidity. Solid lines are from simulations with RH=60%, and the dashed lines are with RH=70%.	17
2.5	ISDAC-i timeseries of (a) cloud thickness, (b) liquid water path, (c) near-surface snow flux. Colors are the same as in Figure 2.4. Data are smoothed over 1 hour periods for better visualization.	18
2.6	ISDAC-i domain mean profiles of (a) vertical velocity variance, and (b) vertical flux of virtual potential temperature, representing buoyancy production of TKE. Colors are the same as in Figure 2.4. Solid lines are from simulations with RH=60%, and the dashed lines are with RH=70%.	19
2.7	ISDAC-i domain mean profiles of (a) clear sky radiative heating rate, and (b) radiative heating rate due to cloud. Colors are the same as in Figure 2.4. Solid lines are from simulations with RH=60%, and the dashed lines are with RH=70%.	19
2.8	Liquid water path (LWP), ice water path (IWP), and snow water path (SWP) in LES ISDAC-i simulations averaged over the 24th hour. The horizontal axis shows the inversion strength, and the vertical axis shows uniform temperature change. Top panels show simulations with $\mathcal{H}_f = 60\%$, and bottom panels show simulations with $\mathcal{H}_f = 70\%$	20
2.9	Same as Figure 2.8, but for LES cloud top height z_i , cloud base height z_b , and cloud thickness z_c	21
2.10	Same as Figure 2.8, but for LES estimated fractional LWP sensitivity $\delta\text{LWP}/\text{LWP}$, sensitivity due to fractional liquid lapse rate changes $\delta\Gamma_l/\Gamma_l$, and sensitivity due to fractional cloud thickness changes $2\delta z_c/z_c$. All sensitivities are referenced to the <i>baseline</i> simulation indicated by the black dots. (2.9) for definition of the terms in the text.	23
2.11	(Left) liquid water lapse rate and (right) fractional change of liquid water lapse rate with respect to temperature at 900 hPa. Typical values for Arctic and Subtropical temperatures are annotated.	23
2.12	TOA longwave cloud radiative effect (W m^{-2}) for LES simulations with (left) $\mathcal{H}_f = 60\%$ and (right) $\mathcal{H}_f = 70\%$	24

2.13	LWP and IWP in MLM ISDAC-i simulations averaged over the 24th hour. The horizontal axis shows the inversion strength, and the vertical axis shows uniform temperature changes. Top panels show simulations with $\mathcal{H}_f = 60\%$, and bottom panels show simulations with $\mathcal{H}_f = 70\%$	25
2.14	Same as Figure 2.13, but for MLM fractional LWP sensitivity $\delta\text{LWP}/\text{LWP}$, sensitivity due to fractional liquid lapse rate changes $\delta\Gamma_l/\Gamma_l$, and sensitivity due to fractional cloud thickness changes $2\delta z_c/z_c$. All sensitivities are referenced to the <i>baseline</i> simulation indicated by the black dots.	26
2.15	Scatter plots of (a) LWP, (b) cloud thickness z_c , (c) inversion strength $\Delta\theta_{li}$, and (d) specific humidity jump q_t , from ISDAC-i simulations averaged at the last hour from MLM (x-axis) and LES (y-axis). The gray lines indicate the 1:1 slope.	27
2.16	Same as Figure 2.13, but for MLM cloud top height z_i , cloud base height z_b , and cloud thickness z_c	29
2.17	Entrainment rates diagnosed from ISDAC-i LES simulations using Eq. (2.2), and parameterized using Eq. (2.5). The slope coefficient $a = 0.85$ and the intercept $w_0 = 0.0004 \text{ m s}^{-1}$ are from a linear fit, with $r^2 = 0.89$. Blue markers show simulations with $\mathcal{H}_f = 60\%$, and red with $\mathcal{H}_f = 70\%$. Marker types distinguish inversion strengths: 3 K (triangles), 5 K (circles), 7 K (squares), 9 K (stars).	33
3.1	Liquid fraction as a function of temperature, computed using the formulation in Kaul <i>et al.</i> [38] with the exponent equals 0.1.	36
3.2	SHEBA domain mean profiles of (a) liquid ice potential temperature θ_{li} , (b) total water specific humidity q_t (with water vapor specific humidity in green), (c) cloud liquid water specific humidity q_l , and (d) total ice water specific humidity ($q_i + q_{snow}$). Dashed lines show the initial profiles, and blue lines show the average over the last 30 minutes.	39
3.3	SHEBA time series of (a) liquid water path, and (b) total ice water path. Also shown are the LES intercomparison ranges in gray shadings, and the observed ranges of values in red.	40

3.4	SHEBA domain mean profiles of time tendencies for (a, c) specific entropy ds/dt , and (b, d) total water specific humidity dq_t/dt . Averages are calculated for the first (top) and the 12th (bottom) simulated hours. Gray shading corresponds to the liquid layer.	41
3.5	M-PACE domain mean profiles of (a) liquid ice potential temperature, (b) total water specific humidity, (c) cloud liquid water specific humidity, and (d) total ice water specific humidity. Black dotted lines show the initial conditions, blue lines show PyCLES averaged for the last 9 hours of the simulation. Gray shadings show the LES intercomparison results from Klein <i>et al.</i> [62].	44
3.6	M-PACE time series of (a) liquid water path, and (b) total ice water path. Also shown are the LES intercomparison range in gray shading, and the observed range of values in red.	45
3.7	M-PACE domain mean profiles of time tendencies for (a, c) specific entropy ds/dt , and (b, d) total water specific humidity dq_t/dt . Averages are calculated for the first (top) and the 12th (bottom) simulated hours. Gray shading corresponds to the liquid layer.	46
3.8	M-PACE domain mean profiles of time tendencies for snow water specific humidity $\partial q_{snow}/\partial t$. Different terms represent autoconversion (AUT), accretion (ACC), deposition/sublimation (DEP), and transport (TRANS) which includes both sedimentation and vertical flux. Averages are over the last 9 simulation hours. Gray shading corresponds to the liquid layer.	47
4.1	Seasonal cycle of monthly mean profiles averaged over the Arctic Ocean (70–82 N) during 2006–2011, showing (a) liquid-containing and (b) ice-dominated cloud fraction from satellite derived dataset CALIPSO-GOCCP. Red dashed lines define the low- and mid-level clouds. Modified from Figure 2 in Cesana <i>et al.</i> [67]. © American Geophysical Union.	50
4.2	Schematics of the surface boundary conditions in the GCM.	54
4.3	Seasonal cycle of domain mean liquid water specific humidity profile (kg kg^{-1}) in the reference climate.	57
4.4	Seasonal (50-day averages) domain mean profiles of liquid water specific humidity (kg kg^{-1}) in reference climate (black) and warm climate (red).	58

4.5	Seasonal cycle of liquid water path, ice water path, rain water path, and snow water path in kg m^{-2} . The reference climate is shown in black, and the warm climate (1.50x) is shown in red.	59
4.6	Seasonal cycle of domain mean ice water specific humidity profile (kg kg^{-1}) in the reference climate.	59
4.7	Time series of the surface energy budget of the reference climate. Time axis shows the days since vernal equinox. Positive values indicate a warming effect on the surface temperature.	60
4.8	Time series of surface temperature (K) in reference climate (black) and warm climate (red). Time axis shows the days since vernal equinox.	61
4.9	Time series of sea ice thickness (m) in reference climate (black) and warm climate (red). Time axis shows the days since vernal equinox.	61
4.10	Seasonal (50-day averages) domain mean profiles of vertical velocity variance $\overline{w'w'}$ ($\text{m}^2 \text{s}^{-2}$) in reference climate (black) and warm climate (red).	62
4.11	Seasonal (50-day averages) domain mean profiles of temperature (K) in reference climate (black) and warm climate (red).	64
4.12	Surface energy budget of the warm climate. Positive values indicate a warming effect on the surface temperature.	64
4.13	Seasonal (50-day averages) domain mean profiles of liquid-ice potential temperature θ_{li} (K) in reference climate (black) and warm climate (red).	65
4.14	Seasonal cycle of domain mean liquid water specific humidity profile (kg kg^{-1}) in warm climate (1.50x longwave optical thickness).	65
4.15	Seasonal cycle of domain mean ice water specific humidity profile (kg kg^{-1}) in warm climate (1.50x longwave optical thickness).	66
4.16	Seasonal (50-day averages) domain mean profiles of static stability ($d\theta_{li}/dz$, in K km^{-1}) in reference climate (black) and warm climate (red).	66
4.17	Seasonal cycle of cloud radiative effects at (top) top-of-atmosphere and (bottom) surface, estimated off-line with RRTMG and domain mean profiles in the reference climate. Each data point is calculated from a 25-day average. The time axis is shifted so that it is equivalent to a regular calendar year starting from January. Red shows LWCRE, cyan shows SWCRE, and the net CRE is in black. Numbers show the annual mean values of each category.	69

4.18	Same as Figure 4.17, but showing the difference between the warm and reference climate.	70
4.19	Annually mean TOA and surface CRE (black), LWCRE (red), and SWCRE (cyan) plotted against mean SST. Solid circles show equinox simulations with various longwave optical thicknesses from a factor of 0.4 to 2.5. Triangles show the reference and warm climates with seasonal cycle and sea ice. Squares show the reference and warm climates with seasonal cycle without sea ice. Open circles show the observed values averaged over the Arctic Ocean by Kay <i>et al.</i> [27].	71
5.1	Map of western and central Bellingshausen Sea. Dots show the locations of all MEOP-CTD profiles used in this study. Colors indicate the different years. Contours show 0, 500 (thickened), 1000, 1500, 2000, 2500 m isobaths from IBCSO bathymetry [116]. Gray shadings indicate the ice shelves in the region: Abbot Ice Shelf (AIS), Venable Ice Shelf (VIS), Stange Ice Shelf (SIS), George VI Ice Shelf (GVIIS), Bach Ice Shelf (BIS), and Wilkins Ice Shelf (WIS). Other features include: Belgica Trough (BT), Latady Trough (LT), Eltanin Bay (EB), and Ronne Entrance (RE). Dashed lines are the Southern ACC front and the Southern Boundary defined by Orsi <i>et al.</i> [117]. The black boxes shows the regions on Figure 5.2 and 5.3. The insert shows the location of the studied region in Antarctica.	79
5.2	Depth-latitude cross-shelf/slope sections at the shelf break. (a) Map of the boxed region on Figure 5.1. (b) θ - S diagram of the sections' profiles, with on shelf ones in grey and offshore in black. The blue lines show select neutral density surfaces. Water masses are labeled in red. See the text for details. (c) Temperature ($^{\circ}\text{C}$, colors) and salinity (contours) for the section near 93°W in August 2010. (d) Geostrophic velocity (m s^{-1} , colors) referenced to the lowest data level and neutral density (kg m^{-3} , contours) for the section near 93°W in August 2010. The contour interval is 0.1 kg m^{-3} . Positive velocity indicates eastward flow. (e) and (f) are the same as (c) and (d), but for the section near 92°W in June 2010. Triangles indicate the latitude of the profiles.	80

- 5.3 (Left) Depth of the Belgica Trough (m) and position of synoptic seal sections. The background shading of the map only shows bathymetry shallower than 1000 m, with the 500 m bathymetry highlighted in black line. Black circles indicate profile locations. (Right) Potential temperature ($^{\circ}\text{C}$, colors) and salinity (contours) sections in the Belgica Trough. Sections (a)–(f) were taken in 04/2010, 12/2013, 02/2008, 12/2013, 03/2008, and 03/2009, respectively. 82
- 5.4 Map of all casts that do (color) and do not (grey) fall within the Gade envelope; see Appendix A for Gade envelope criteria. Shallow casts are removed from Gade envelope analysis. The color indicates the mean meltwater mixture layer depth (m), and the sizes of the circles show the meltwater mixture layer thickness. The inserts show the Eltanin Bay region (red box) in 2009 and winter 2013-2014. 83

LIST OF TABLES

<i>Number</i>	<i>Page</i>
2.1 List of parameters and ranges over which they are varied in the sensitivity studies with ISDAC-i. Baseline parameter values in bold. .	11
3.1 Observed LWP and IWP (both cloud ice and snow) from three Arctic boundary layer cloud model intercomparison case studies. The observational sources come from Morrison <i>et al.</i> [41], McFarquhar <i>et al.</i> [52], and Klein <i>et al.</i> [62]. Averaged values from PyCLES are shown in the brackets.	46
4.1 Estimated cloud feedback parameters in $\text{W m}^{-2} \text{K}^{-1}$, using various LES simulations and off-line RRTMG calculations. For the equinox simulations, the warmest climate is excluded for feedback estimation, and all other cases follow a linear CRE relationship with SST (Figure 4.19).	72

Chapter 1

INTRODUCTION

1.1 Polar Clouds and Climate

The Earth's poles, loosely defined as poleward of 70 degrees latitude, are characterized by extreme seasonal cycles and the presence of sea ice and ice sheets. Although limited in areal extent, the polar regions strongly interact with the lower latitudes via feedbacks and teleconnections, and thus are essential components of Earth's climate.

Some of the most visible and dramatic changes are happening in the polar regions, as greenhouse gas concentrations are rising. Arctic surface temperature has been rising significantly more than that of the lower latitudes [e.g., 1–3]. Arctic sea ice extent shows downward trends in all seasons according to the modern satellite record [4]. The presence of a continent and the surrounding Southern Ocean make Antarctica different from the land-surrounded Arctic Ocean. One of the most dramatic changes there is associated with the loss of Antarctic ice shelves, which are the floating extension of the ice sheets [5].

These changes are projected to continue if not accelerate in climate models. In fact, one of the most robust features in climate projections since the earliest general circulation models (GCM) studies is polar amplification, namely the polar region warms much more than the global mean when CO₂ concentration is doubled [6]. It has been recognized that not a single but multiple processes contribute to this phenomenon, such as ice-albedo feedback, atmospheric and oceanic heat transport, cloud feedback, etc. [7, 8]. This thesis focuses on one of the most uncertain components of the polar climate: polar cloud dynamics.

The polar regions are among the cloudiest places on Earth. Figure 1.1 shows a satellite view of the summer Arctic Ocean. From this visible image, one can hardly distinguish between clouds, sea ice, and land ice. In fact, clouds are often found over all surfaces in the Arctic. The brightness of clouds and their sharp albedo contrast with the dark ocean surface make Arctic clouds a robust reflector of shortwave radiation during sunlit months. At the same time, the low-level liquid-rich clouds also act as an efficient longwave insulator for the surface throughout the year. The net radiative effect of clouds in the Arctic is to warm the surface in the annual mean

[9], which is the opposite from clouds in the lower latitudes. Exactly how clouds respond to climate change in the polar regions can have immediate impact on the surface energy budget and the sea ice state. The chapters in this thesis address one central theme: how do polar clouds respond to climate change? What processes drive the polar cloud response?

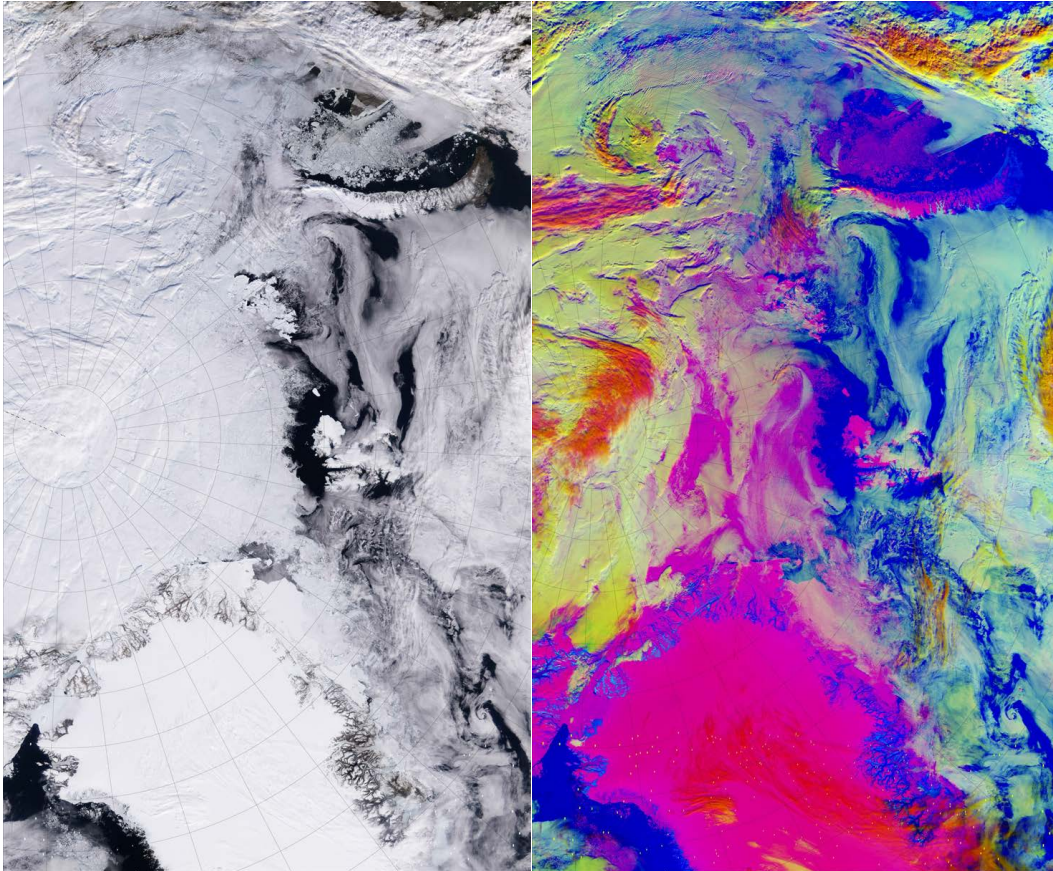


Figure 1.1: Visible (left) and false color (right) image of the Arctic from the Moderate Resolution Imaging Spectroradiometer (MODIS) on NASA's Terra satellite. The North Pole is at the center left of the image, Greenland is at the bottom, Barents and Kara Sea are on the right. On the false color image, deep blue shows the ocean surface, magenta and red shows sea ice and ice sheet. Light orange and cyan show high and low clouds correspondingly. (NASA images by Robert Simmon and Jesse Allen, based on MODIS data.)

1.2 Modeling Approach

The dynamics of clouds involve motions of multiple scales, from the global-scale circulation that provides boundary conditions to scales of individual cloud particles that undergo changes in morphology and phases. This makes clouds especially hard to parameterize in GCMs whose horizontal resolution is on the order of 10–100 km.

Turbulence and cloud parameterizations are often developed and tuned for lower latitudes where most of the observations are made, which makes it even harder to interpret GCM results of polar clouds.

Therefore, our studies use large eddy simulations (LES) to explicitly resolve the most energetic motions that are essential for cloud dynamics. LES has become a standard tool for studying the boundary layer (BL) and cloud response to climate change in the subtropics [e.g., 10–13]. Here we exploit LES further by pushing its limit toward resolving an entire polar troposphere column, and exploring the response of polar clouds to climate change under consistent large-scale forcing.

Although LES gives us reliable simulations of clouds, it may still be hard to have a mechanistic understanding of the underlying dynamics. Detailed budget analyses can be made for entropy, specific humidity, and precipitation to separate contributions from various processes. For well-mixed cloud topped BL with light precipitation, one can use mixed-layer theory [e.g., 14] to reproduce LES results. Therefore, a combination of modeling and theoretical tools will enable us to make progress in polar cloud dynamics.

1.3 Thesis Outline

This thesis presents the first results of Arctic clouds simulated by Python Cloud Large Eddy Simulation code (PyCLES, [15]). Because of the novelty of our LES model, we spend considerable effort on validation and exploring the parameter space. We use three Arctic case studies to compare results from PyCLES to observations and LES intercomparison models. Chapter 2 validates the LES model with a persistent Arctic boundary layer cloud over sea ice. We then conduct sensitivity studies on the BL response to warming and free-tropospheric humidity changes, which are motivated by projected Arctic climate change. We use mixed-layer theory to analyze the BL response. Chapter 3 provides two more case studies to further validate the LES model. The results are in reasonable agreement with observations and other LES models. Both Chapter 2 and 3 provide foundations for a more systematic study of Arctic cloud response to climate change in Chapter 4. This is the most novel part of the thesis, where we use a GCM to provide large-scale forcing for the LES model with a seasonal cycle and sea ice. Chapter 5 is independent from the rest, and focuses on oceanic circulation near ice shelves in Antarctica using seal-borne observations. Chapter 6 briefly concludes all studies, and provides an outlook for future research.

*Chapter 2***ARCTIC STRATOCUMULUS IN LARGE EDDY SIMULATIONS
AND A MIXED-LAYER MODEL****2.1 Abstract**

The stable and cloudy Arctic boundary layer (BL) is an essential component of the Arctic climate system and is often thought to contribute to Arctic amplification of global warming. However, regional and global climate models that depend on parameterized representations of BL turbulence and clouds show large spreads in simulated Arctic cloudiness. We use large eddy simulations (LES) that explicitly resolve BL turbulence and clouds to explore the sensitivities of Arctic BL clouds to idealized climate change. Condensed water path is found to increase with BL temperature and free-tropospheric relative humidity, but it decreases with inversion strength across the BL top. The condensed water changes are indicative of a positive longwave cloud feedback as the Arctic warms. The magnitude of the cloud feedback sensitivity depends on the vertical structure of warming. The trends shown by the LES climate change experiments can be largely reproduced by a mixed-layer model that excludes microphysical processes. Thus, these results offer encouragement that analysis methods used to explain the sensitivities of lower-latitude BL clouds to climate change can be usefully extended to Arctic BL clouds.

2.2 Introduction

The Arctic boundary layer (BL) is known for its ubiquitous temperature inversion and the prevalent mixed-phase low clouds [16]. Though the inversion strength and height vary from season to season, the overall inversion probability is as high as 90% [17]. Many of these inversions are elevated, capping a well-mixed layer below. Annual-mean cloud fraction is around 70%, with a maximum greater than 80% in autumn [9, 18]. These characteristics have manifold impacts on high-latitude climate. For example, Arctic clouds warm the surface in all seasons but summer because their longwave greenhouse effect predominates over shortwave effects, unlike for their subtropical counterparts [9, 19]. Therefore, Arctic cloud feedbacks may operate differently from those at lower latitudes. Moreover, anomalous spring-time clouds have been postulated to influence the autumn sea ice minimum through long-term effects on the surface energy balance [20].

Climate change in the polar regions has interested scientists since the first modeling studies of the effects of increased CO₂ concentrations. Climate models robustly show Arctic amplification under greenhouse warming [6, 7]. In recent decades, the Arctic indeed has been experiencing rapid changes. Arctic sea ice extent, most prominently in September, has shrunk substantially since the beginning of the modern satellite record [4]. Amplified warming in high northern latitudes has also been observed over the past decades, especially in winter [1, 3]. This warming has been observed to be surface intensified [21], with trends that can be discerned in observational records despite the large internal variability in high latitudes [22]. Furthermore, significant increases in specific humidity have been observed, but relative humidity changes are more complex [2, 23]. Cloud feedbacks and the trapping of heat under the stable inversion are thought to contribute to Arctic amplification of global warming [7, 24–26]. However, the sign of any cloud feedback in high latitudes is uncertain [27]. In GCMs, low clouds depends on parameterizations for turbulence and convection, which are developed mainly for lower latitudes. In fact, GCMs show large spread in the simulated seasonal cycle of Arctic cloud fraction [28, 29]. A key step towards constraining Arctic cloud feedbacks is to identify robust mechanisms of how the clouds respond to changes in temperature, inversion strength, and moisture content of the free troposphere.

Recent modeling studies have focused on microphysical and dynamical processes maintaining Arctic mixed-phase stratocumulus clouds. Savre *et al.* [30] investigated how the persistence of Arctic mixed-phase clouds depends on microphysical processes and moisture sources in the sub-cloud layer and in the free troposphere. They found that microphysical processes (ice sublimation) play an important role in controlling the BL structure. A more idealized study by Solomon *et al.* [31] found a similar role for ice microphysics in controlling BL moisture. One important question that was not addressed by either study is how Arctic mixed-phase clouds respond to climate change. How will the low cloud properties change as the Arctic warms?

Here we use large eddy simulations (LES) with the recently developed Python Cloud Large Eddy Simulation code (PyCLES) [15] to investigate systematically the response of Arctic BL clouds to different kinds of idealized changes. We base our study on the Indirect and Semi-direct Aerosol Campaign (ISDAC) LES intercomparison study [32]. In an idealized setup (hereafter ISDAC-i) mimicking conditions during the ISDAC observational campaign, we investigate the sensitivities

of Arctic mixed-phase stratocumulus clouds to temperature, cloud-top inversion strength, and free-tropospheric moisture. These are important factors controlling stratocumulus properties [33, 34], and understanding them is a first step toward understanding how Arctic low clouds respond to climate change. We then use a mixed-layer model (MLM) to elucidate the cloud response to perturbations seen in the LES. MLMs have been extensively used to study stratocumulus-topped BLs over subtropical oceans [14, 33, 35, 36], but rarely Arctic BL clouds. Yet they turn out to be similarly useful for providing insight into controls of Arctic stratocumulus clouds.

We begin by describing the LES and MLM used in the study. Then we specify the experimental setup of the original ISDAC LES intercomparison and ISDAC-i. We justify the ISDAC-i setup by characteristics of the projected Arctic warming. Next we show the results from ISDAC and ISDAC-i simulations, followed by discussion and conclusions.

2.3 Model Descriptions

LES Code

We work with the recently developed PyCLES code, which uses total water specific humidity and specific entropy as prognostic variables to solve the anelastic equations of motion [15]. PyCLES has been used successfully to simulate subtropical marine BL clouds [12, 13, 37]. This is its first application in a polar setting.

We use a nominally 5th-order Weighted Essentially Non-Oscillatory (WENO5) advection scheme for momentum and scalars, and a strong stability preserving 3rd-order, 3-stage Runge-Kutta method for time-stepping. The time-steps are adaptive with a target Courant number of 0.7. The numerical dissipation implicit in the WENO scheme is used in lieu of an explicit subgrid-scale dissipation scheme, as this has been found to lead to the most faithful simulation of subtropical stratocumulus [37]. We only use a Smagorinsky-Lilly subgrid-scale closure near the surface to transfer momentum between the LES domain and the surface. Monin-Obukhov similarity theory is used to compute the surface flux of momentum at the lower boundary. The roughness length is set to 4×10^{-4} m. The surface sensible and latent heat fluxes are zero for all simulations presented in this study, which is based on the assumption that turbulent heat fluxes are small over sea ice. The grid resolution is 50 m in the horizontal, with doubly periodic boundary conditions, and 10 m in the vertical. The computational domain extends $3.2 \text{ km} \times 3.2 \text{ km}$ in the horizontal and

is 2.56 km deep in the vertical.

Microphysics

The modeling of mixed-phase microphysics remains an active area of research. We use a relatively simple one-moment microphysics scheme that captures basic features of Arctic mixed-phase clouds [38]. Cloud condensates are diagnosed using an empirical partition function $f(T)$ that models the liquid fraction λ of the condensate as a function of temperature [15, 38, 39],

$$\lambda(T) = \begin{cases} 0 & \text{for } T < T_i, \\ \left(\frac{T - T_i}{T_f - T_i}\right)^n & \text{for } T_i \leq T \leq T_f, \\ 1 & \text{for } T_f < T, \end{cases} \quad (2.1)$$

where $T_f = 273.15$ K is the freezing point, and $T_i \approx 235$ K is the homogeneous nucleation temperature. The exponent n here is chosen to be 0.1 [38], justified by the fact that liquid fractions close to 80% at 240–250 K have been observed in Arctic low clouds [40].

The same partition function (2.1) is used to determine the effective specific latent heat L in the mixed phase and a thermodynamically consistent saturation vapor pressure [15]. Precipitation species (rain and snow) are prognostic. The processes that govern the transformation between species include autoconversion, aggregation, and phase changes. Sedimentation of cloud condensate is not taken into account. The scheme uses exponential particle size distribution functions for rain, ice, and snow. Cloud ice has a constant intercept parameter $N_{0,\text{ice}} = 1 \times 10^7 \text{ m}^{-4}$. The snow intercept parameter $N_{0,\text{snow}}$ is a diagnostic function of snow specific humidity [41]. More details of the scheme are given in Kaul *et al.* [38].

We made several minor modifications to the microphysical source terms in Kaul *et al.* [38]. The thermodynamic variable G , which represents the vapor diffusion of an ice-water sphere and determines the mass growth rate of liquid droplets or ice crystals, is taken without approximation, following Straka [42], as

$$G(T, P) = \left[\frac{\rho_{l/i} R_v T}{D p_v^*(T)} + \left(\frac{L}{R_v T} - 1 \right) \frac{L \rho_{l/i}}{\kappa T} \right]^{-1}.$$

Here, $\rho_{l/i}$ is the density of liquid or ice, depending on the process, L is the effective latent heat, and p_v^* is the saturation vapor pressure; D is the water vapor diffusivity,

which increases with temperature and decreases with pressure; and κ is the thermal conductivity, which depends approximately linearly on temperature. The detailed formulations of D and κ are given in Straka [42]. The function G increases approximately exponentially with temperature and is used in formation (autoconversion), evaporation, and deposition/sublimation of droplets and ice crystals.

The formation of precipitation and evaporation/sublimation of hydrometeors contribute to the entropy tendency. The small heat transfer and the aerodynamic drag during sedimentation are also included in the entropy source/sink terms, as specified in Pressel *et al.* [15].

Radiative Transfer

The default ISDAC longwave radiation scheme is idealized and depends solely on cloud liquid water content [32]. In order to capture radiative flux changes under climate change, we use the RRTMG [43] integrated into PyCLES. Additional information on temperature, humidity, and ozone above the LES domain is required to calculate radiative fluxes. Therefore, the standard atmospheric profiles from the Mixed-Phase Arctic Cloud Experiment (M-PACE) LES intercomparison project are patched to the ISDAC temperature and humidity profiles. RRTMG produces a more realistic radiative flux profile, which results in slightly warmer BL compared to the ISDAC simulations with idealized radiation. RRTMG is called every 60 simulated seconds in PyCLES.

The liquid effective radius entering the radiative transfer calculation uses the parameterization by Martin *et al.* [44] for warm stratocumulus clouds [10, 12]. The mean ice effective radius follows an empirical relation that depends on temperature and ice water content [45],

$$r_{e,\text{ice}} = 34.419 \mu\text{m} \times \left(\frac{\text{IWC}}{1 \text{ g m}^{-3}} \right)^{0.06} \exp [0.013 \text{ K}^{-1}(T - 273.15 \text{ K})],$$

where IWC is the ice water concentration (units of g m^{-3}). The mean ice effective radius is mainly a function of temperature and increases with temperature at a rate of $\sim 0.5 \mu\text{m K}^{-1}$. It is only sensitive to IWC at low IWC values [45]. Only cloud ice is included in the radiative transfer calculation. The ice effect on cloud infrared optical depth is minimal because the cloud layer is dominated by the optically thick liquid water.

Mixed-layer Model

We use a MLM with liquid-ice potential temperature θ_{li} , total water specific humidity q_t , and BL height z_i as prognostic variables [14, 33, 35]:

$$\frac{dz_i}{dt} = w_e + w_{LS}(z_i), \quad (2.2)$$

$$\frac{d\theta_{li}}{dt} = \frac{1}{z_i} \left(w_e \Delta\theta_{li} - \frac{\Delta F_R}{\rho_a c_p} \right), \quad (2.3)$$

$$\frac{dq_t}{dt} = \frac{1}{z_i} w_e \Delta q_t. \quad (2.4)$$

Here, w_e is the cloud-top entrainment rate, w_{LS} is the large-scale subsidence rate as a function of height, and ρ_a is the mean density of air. The Δ variables represent contrasts across the entire BL. For example, $\Delta F_R = F_R^+ - F_{R,0}$ represents the total radiative flux contrast between the fluxes at the BL top and at the surface (see Appendix 2.7 for a list of variables). The same phase partitioning (2.1) is used to diagnose cloud liquid and ice water specific humidity q_l and q_i . Microphysical processes are not included in the MLM. A standard saturation adjustment procedure is called to get q_l and q_i at every time step, which then go into radiative transfer calculations. Time-stepping uses a 2nd-order 2-stage Runge-Kutta method with fixed time steps of 300 s. Radiative transfer uses the same RRTMG scheme as PyCLES and is called at every time step. Only the longwave radiative flux profile from RRTMG is used to calculate the radiative fluxes in (2.3). After the BL values are obtained at each time step, vertical profiles are calculated using the prescribed free tropospheric conditions as upper boundary conditions. The MLM vertical resolution is 5 m.

An entrainment rate formula is needed to close the set of MLM equations. Because of the lack of surface heat fluxes, turbulence in the BL is mostly driven by cloud-top radiative cooling. We parameterize the entrainment rate as

$$w_e = a \underbrace{\frac{\Delta_i F_R}{\rho_a c_p \Delta\theta_{li}}}_{\text{direct}} + \underbrace{w_0}_{\text{indirect}}, \quad (2.5)$$

where $a = 0.85$ and $w_0 = 0.0004 \text{ m s}^{-1}$ are constants diagnosed from ISDAC-i LES simulations. This is in line with assuming a direct and an indirect contribution of radiation to the mean entrainment rate [46]. We define Δ_i to be the jump across the

entrainment zone, more specifically the difference in values between the top of the well-mixed layer and the level at which turbulence goes to zero. For the prognostic variables, Δ_i and Δ are equivalent. BL height z_i , predicted by the MLM, lies within the entrainment zone. We assume that $\Delta\theta_{li} \approx \Delta_i\theta_v$ and that the longwave radiative flux jumps nearly discontinuously by $\Delta_i F_R$ at the cloud tops, driving radiative cooling at the top and with it the mixed-layer turbulence. Note that $\Delta_i F_R$ is usually less than the total radiative flux contrast ΔF_R [47]. The direct term in (2.5) arises in an integration of the buoyancy budget across the BL top [48, 49]. Details of the entrainment parameterizations are described in Appendix 2.8.

2.4 Experimental Setup

ISDAC LES Intercomparison

The ISDAC LES intercomparison is based on observations of a long-lived mixed-phase stratocumulus cloud on April 26-27, 2008 north of Barrow, Alaska [32]. Soundings at Barrow show a stable surface layer below a well-mixed cloud layer. The boundary layer is capped by a strong potential temperature inversion, with a dry free atmosphere above.

Our setup generally follows the ISDAC LES intercomparison (see the Appendix A of Ovchinnikov *et al.* [32]). We define θ_{li} following Tripoli & Cotton [50] and Pressel *et al.* [15] as

$$\theta_{li} = \theta \exp\left(-\frac{L}{T c_p} \frac{q_l + q_i}{1 - q_t}\right), \quad (2.6)$$

where the effective specific latent heat L is a weighted sum of that for vaporization and sublimation, using the partition function (2.1) as weight. Surface heat fluxes are set to zero because the fluxes over sea ice were negligible during the field campaign [32]. Large-scale subsidence is specified to be linear with height below the initial inversion at 825 m altitude, and it is constant with height above:

$$w_{LS} = \begin{cases} -5 \times 10^{-6} \text{ s}^{-1} \cdot z, & z < 825 \text{ m}, \\ -4.125 \times 10^{-3} \text{ m s}^{-1}, & z \geq 825 \text{ m}. \end{cases} \quad (2.7)$$

This choice of subsidence profile is justified in Ovchinnikov *et al.* [32], and it is kept fixed for all simulations here. In addition to the large-scale subsidence, relaxation of the prognostic variables above 1200 m altitude toward the initial conditions is also included. Relaxation is specified as an additional source term in

Table 2.1: List of parameters and ranges over which they are varied in the sensitivity studies with ISDAC-i. Baseline parameter values in bold.

Variable	Range
$\theta_{li,0}$	261, 265 , 269, 273 K
$\Delta\theta_{li}$	3, 5 , 7, 9 K
\mathcal{H}_f	60 , 70%

the prognostic equations. We relax specific entropy s (a native PyCLES variable instead of the otherwise common liquid-ice potential temperature) and total water specific humidity q_t toward the initial profiles above 1200 m, with a relaxation timescale of 1 hour. Horizontal velocities are relaxed toward the initial profiles throughout the domain with a timescale of 2 hours. The simulation is run for 8 hour integration time.

ISDAC-i: Idealized Climate Change

The initially decoupled surface layer does not persist and becomes well-mixed in the ISDAC simulations. Therefore, we initialize ISDAC-i with well-mixed profiles of θ_{li} and q_t below the inversion at height z_i . This allows the free troposphere to be the only source of moisture for the cloud (apart from recycling of moisture), and it shortens the equilibration time of the simulations. The initial profiles are (Figure 2.1):

$$\theta_{li} = \begin{cases} \theta_{li,0}, & z \leq z_i \\ \theta_{li,0} + \Delta\theta_{li} + \Gamma_\theta(z - z_i), & z > z_i \end{cases}$$

$$q_t = \begin{cases} q_{t,0}, & z \leq z_i, \\ q_s(T)\mathcal{H}_f, & z > z_i. \end{cases}$$

Here, $q_{t,0} = q_s(T_0)\mathcal{H}_0$, where q_s is the saturation specific humidity, T_0 is the surface temperature, and $\mathcal{H}_0 = 0.8$ is a near-surface relative humidity. This setup allows q_t to respond to temperature changes for a fixed relative humidity. We assume potential temperature lapse rate Γ_θ and relative humidity \mathcal{H}_f that are constant with height above the cloud top. This setup enables us to explore different initial conditions that help us to gain insight into climate change in polar regions.

Idealized climate change studies are conducted by varying three variables (Table 2.1):

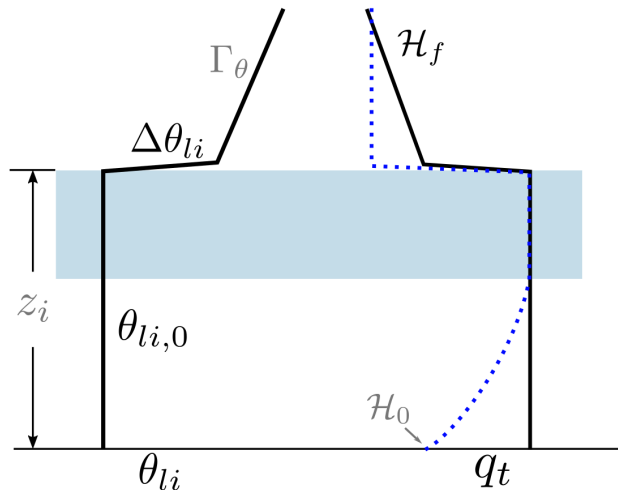


Figure 2.1: Schematic of the ISDAC-i θ_{li} and q_t initial conditions. The cloud layer is indicated in blue. The BL with height z_i has constant θ_{li} and q_t , where q_t is determined by the relative humidity (blue dotted line) near the surface \mathcal{H}_0 . The BL is capped by an inversion of $\Delta\theta_{li}$, above which potential temperature increases with height at the rate Γ_θ . Relative humidity above the BL, \mathcal{H}_f , does not vary with height, and it is used to determine q_t above z_i .

1. *Initial mixed-layer liquid-ice potential temperature $\theta_{li,0}$.* Changing only $\theta_{li,0}$ produces uniform warming or cooling in the entire domain. We vary $\theta_{li,0}$ from 4 K cooler to 8 K warmer, while the highest temperature at the surface is close to the freezing temperature. Beyond this temperature, we can no longer justify negligible surface heat fluxes when the surface is ice-free.
2. *Inversion strength $\Delta\theta_{li}$.* Temperature inversions are a common feature in and above the Arctic BL. The frequency of occurrence is as high as 90%, with a typical strength of 5–10 K [17]. Changing $\Delta\theta_{li}$ can be thought of as changing the horizontal advection in the free troposphere from lower latitudes, or as changing the degree to which warming is surface amplified. We expect the inversion to weaken in a warmer climate, as the warming is surface amplified [21]. The inversion strength directly affects entrainment processes at the cloud top and the amount of free-tropospheric moisture. We would like to distinguish the inversion strength from the commonly used lower-tropospheric stability (LTS), generally defined as the potential temperature difference between at 700 hPa and the surface [51]. LTS cannot distinguish surface inversions from the elevated inversions that occur in all seasons in the Arctic, and it does not directly determine the cloud-top entrainment process. Thus, the inversion

strength on which we focus is more directly relevant for BL processes.

3. *Relative humidity in the free troposphere \mathcal{H}_f .* Typical values of relative humidity in the lower free troposphere at 70N are about 60% to 70%. The projected relative humidity change with warming in climate models is negligible in this region [23]. Therefore, we run a set of simulations with $\mathcal{H}_f = 60\%$, then compare them to those with $\mathcal{H}_f = 70\%$. We fix the value of \mathcal{H}_f and determine $\Delta q_t = q_s(T^+) \mathcal{H}_f - q_{t,0}$ from temperature and relative humidity across the cloud top. Although Δq_t is the relevant variable for cloud-top entrainment, prescribing Δq_t can lead to unreasonable relative humidity \mathcal{H}_f , which in reality is controlled by the large-scale circulation. For example, if we fix Δq_t instead of \mathcal{H}_f while changing $\theta_{li,0}$ and $\Delta\theta_{li}$, \mathcal{H}_f varies from 40 to 80%.

We ran 32 simulations with different initial conditions, each for 24 hours. Due to the setup of ISDAC-i, there is no surface heat flux to balance the cloud-top entrainment. Most simulations cannot reach a steady state over the simulated time we consider here. Therefore, we analyze both the end states and the time tendencies of the BL sensitivities.

2.5 Results

Comparison with LES Intercomparison

Figure 2.2 shows the domain-mean profiles of liquid-ice potential temperature θ_{li} , total-water specific humidity q_t , liquid-water specific humidity q_l , and the sum of ice and snow specific humidity $q_i + q_{\text{snow}}$, all averaged over the last hour of the simulation. Observations gathered by the National Research Council of Canada Convair-580 aircraft from ISDAC flight 31 are also shown for comparison [52]. Data are binned at a vertical interval of 50 m for the in-cloud measurements of temperature, humidity, and liquid and ice water contents. Also shown are the mean and 15–85 percentile range of the ISDAC LES model intercomparison [32]. As in the simulations in the ISDAC LES intercomparison study, the BL in our simulation becomes well mixed as turbulence generated by cloud-top radiative cooling mixes the cloud and sub-cloud layer. The initially stable layer near the surface is not maintained in our simulations; cloud-top radiative cooling leads to a BL that is cooler than was observed. A mixed-phase cloud layer of ~ 300 m thickness persists throughout the simulation (Figure 2.3). Although the initial liquid water specific humidity q_l is within the observed range, it becomes greater than observed at the

end of the simulation. This is consistent with the cooler θ_{li} profile, allowing more condensation than the initial conditions. The ISDAC intercomparison setup lacks large-scale forcing, which could keep the BL from cooling and deviating away from the initial conditions. The resulting biases can reinforce themselves through cloud-top radiative cooling, until radiation and subsidence warming become comparable.

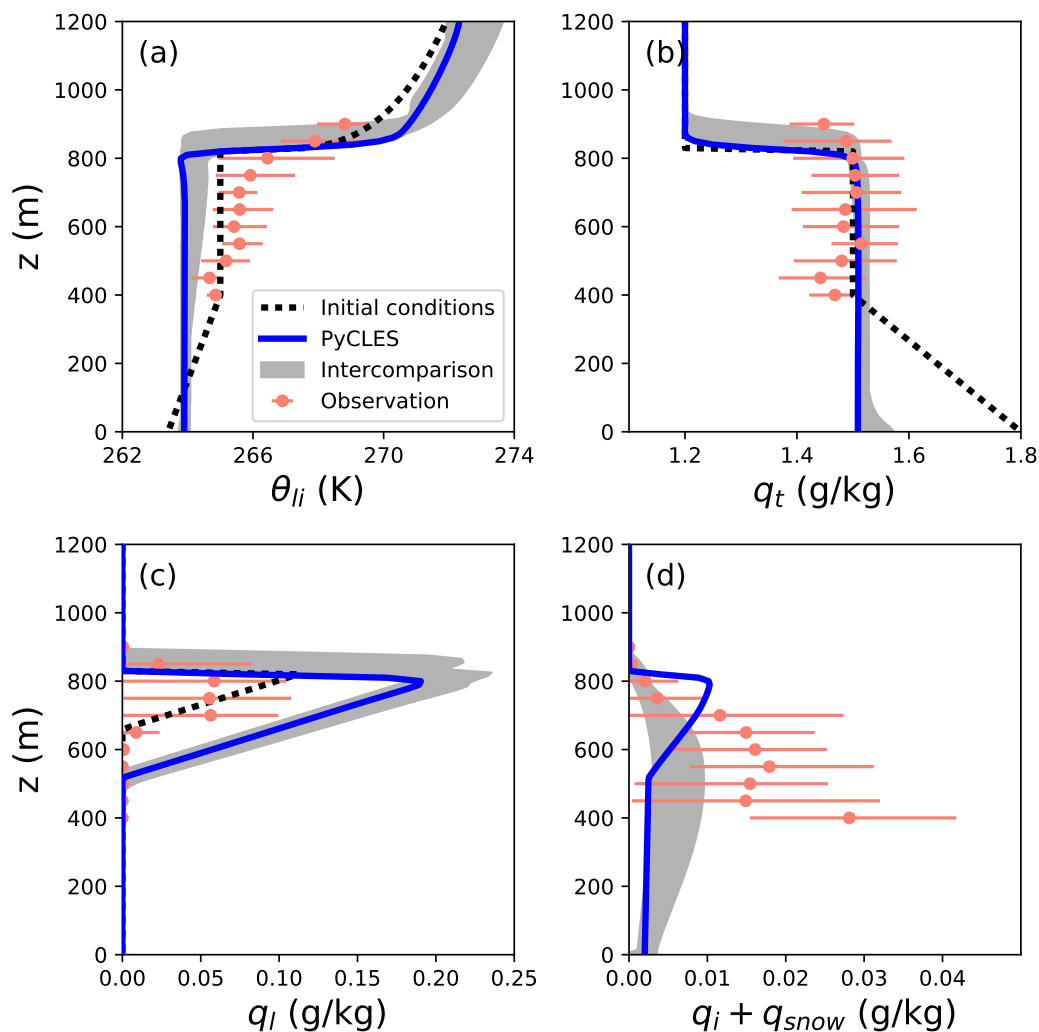


Figure 2.2: Domain mean profiles of (a) liquid ice potential temperature, (b) total water specific humidity, (c) cloud liquid water specific humidity, and (d) the sum of cloud ice and snow water specific humidity. Black dotted lines are the initial condition profiles. Gray shading shows the LES intercomparison range in Ovchinnikov *et al.* [32]. The pink dots show the aircraft observations of flight 31 of ISDAC campaign on April 27, 2008. The horizontal lines indicate the 15–85 percentile range for the measurements binned every 50 m.

The observed total ice water specific humidity, which includes cloud ice and snow

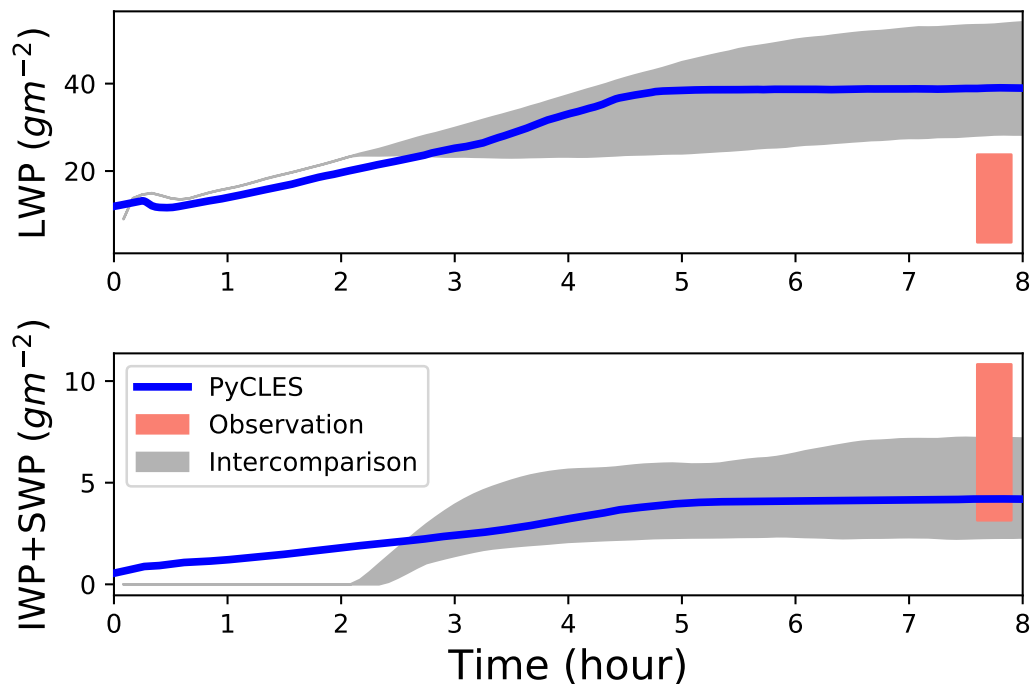


Figure 2.3: Timeseries of (top) liquid water path and (bottom) the sum of cloud ice and snow water path. Gray shading shows the LES intercomparison range in Ovchinnikov *et al.* [32]. The pink bars show the range of observed values estimated using ISDAC flight 31 data in Figure 2.2.

(observations do not distinguish cloud ice from snow), shows large variance (Figure 2.2d). Our LES overestimates q_i at the cloud top, but it underestimates the snow below. The shape of our ice profile arises because q_i is diagnosed and takes the same shape as q_l , while q_{snow} is prognostic and has a peak at cloud base. Liquid water path (LWP) at the end of the eighth hour in our simulation is 39 g m^{-2} , which is within the range of the intercomparison values (Figure 2.3). The sum of ice water path (IWP) and snow water path (SWP) is 4 g m^{-2} , also within the range of the intercomparison [32]. Using data from the ISDAC flight 31, we estimate the LWP to be $3.7\text{--}24 \text{ g m}^{-2}$, and IWP to be $3.1\text{--}11 \text{ g m}^{-2}$. Other studies have estimated different values, for example, Fan *et al.* [53] suggest LWP and IWP to be of comparable magnitudes of $5\text{--}8 \text{ g m}^{-2}$. Savre *et al.* [54] use LWP of $8\text{--}16 \text{ g m}^{-2}$ and IWP of $4\text{--}10 \text{ g m}^{-2}$ as the observational references for their benchmark simulation. One should also be aware of the uncertainties associated with the aircraft observations. Fan *et al.* [53] implies that the measured ice water content's uncertainty is up to 100%. Nevertheless, both PyCLES and the LES intercomparison tend to overestimate LWP and produce IWP at the lower end of the observations.

Models with more complex bulk microphysics schemes still tend to underestimate q_i and IWP [32]. However, LES with bin microphysics schemes produce higher IWP, and so do bulk schemes whose particle slope distribution is fitted to resemble that of the bin schemes. Unfortunately, such ice properties cannot be derived from observations so far [55]. We recognize the underproduction of ice compared to observations, and focus our study on the macrophysical dynamics. Given our relatively simple treatment of microphysics, our LES captures the main features of the BL during ISDAC as well as other LES in the intercomparison.

To check for convergence of the simulations, we ran the ISDAC case with increased domain size and reduced horizontal grid spacing. Doubling the domain size and/or the horizontal resolution (halving the grid spacing) produced no significant changes to the results (not shown, in agreement with [38]).

ISDAC-i

LES

We first show the domain mean profiles at the 24th hour (Figure 2.4) and timeseries (Figure 2.5) of three selected cases to demonstrate the different simulations. In addition to the *baseline* simulation that is close to the ISDAC intercomparison ($\theta_{li,0} = 265$ K, $\Delta\theta_{li} = 5$ K), we also choose to present a *warm* case ($\theta_{li,0} = 273$ K, $\Delta\theta_{li} = 3$ K), and a *cold* case ($\theta_{li,0} = 261$ K, $\Delta\theta_{li} = 9$ K). We choose these three cases as examples because warming in the Arctic is surface intensified, and we can interpret it as a combined effect of uniform warming and a weakened elevated inversion. Therefore, we use the term “surface intensified warming” to refer to increasing $\theta_{li,0}$ together with decreasing $\Delta\theta_{li}$. On the other hand, “uniform warming” refers to changing only $\theta_{li,0}$. All three cases consist of well-mixed BLs with light snow. The most significant feature in the θ_{li} and q_t profiles is the increase of inversion height z_i from *cold* to *warm* (Figure 2.4a and b), which corresponds to an increase of cloud thickness z_c (Figure 2.5a).

Cloud liquid q_l increases with Arctic warming (Figure 2.4c, Figure 2.5b), yet the cloud ice shows a non-monotonic response (Figure 2.4d, Figure 2.5c). The amount of ice depends on the liquid fraction λ and total cloud condensate, which both vary with temperature. Given a fixed total cloud condensate amount, ice water decreases with Arctic warming because λ increases with temperature. Although the total cloud condensate still increases under uniform warming in ISDAC-i, λ increases more rapidly, leading to a lowered ice water amount under surface intensified warm-

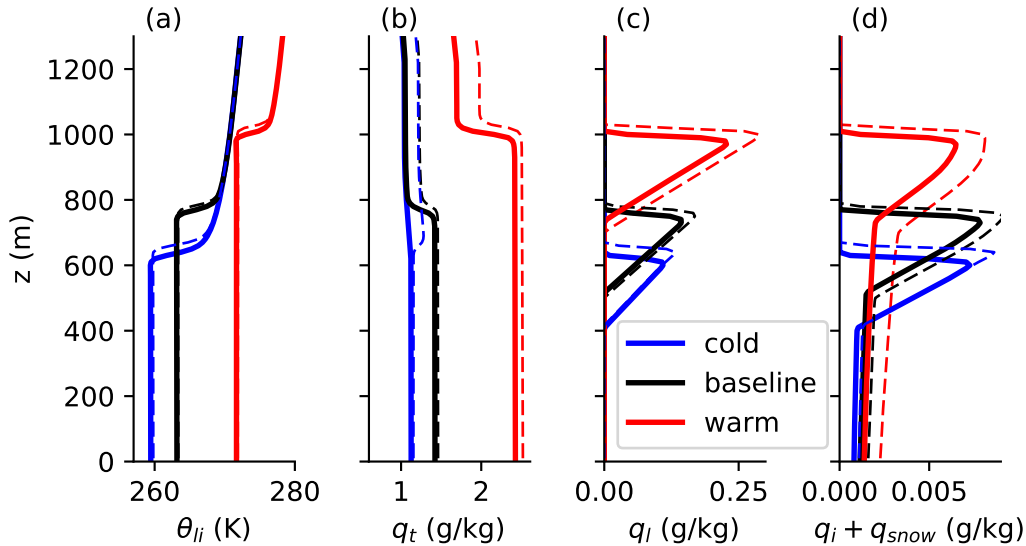


Figure 2.4: ISDAC-i domain mean profiles of (a) liquid ice potential temperature, (b) total water specific humidity, (c) liquid water specific humidity, and (d) the sum of cloud ice and snow water specific humidity. Solid lines are from simulations with $RH=60\%$, and the dashed lines are with $RH=70\%$.

ing. But snow, unlike cloud ice, is a prognostic variable. Its amount depends on microphysical processes. Autoconversion is the dominant source term for snow, and it increases significantly under surface intensified warming. SWP increases monotonically with Arctic warming, similarly to LWP (Figure 2.5d). There is no significant rain in the ISDAC-i simulations.

To further emphasize that the BLs are indeed well-mixed in ISDAC-i, Figure 2.6 shows the profiles of vertical velocity variance $\overline{w'w'}$ and vertical flux of virtual potential temperature $\overline{w'\theta'_v}$ (approximating the buoyancy production of TKE) for the three cases. A single peak in $\overline{w'w'}$ is found for each case, as is common in well-mixed BLs. The shape of the $\overline{w'\theta'_v}$ profile is the result of a combination of cloud processes [56]. The negative peak at the cloud top is indicative of entrainment, and the positive peak in the cloud is the evidence of longwave radiative cooling. The flux vanishes at the surface due to the absence of surface heating. The positive $\overline{w'\theta'_v}$ below the cloud layer confirm the lack of decoupling in all three cases. This means that microphysical processes in ISDAC-i are too weak to cause decoupling, which is observed in other Arctic cases [31]. The significant increase of turbulent fluxes with surface intensified warming is mainly driven by stronger cloud radiative cooling due to higher q_l . Figure 2.7 shows the clear sky and cloudy radiative heating rates. Note

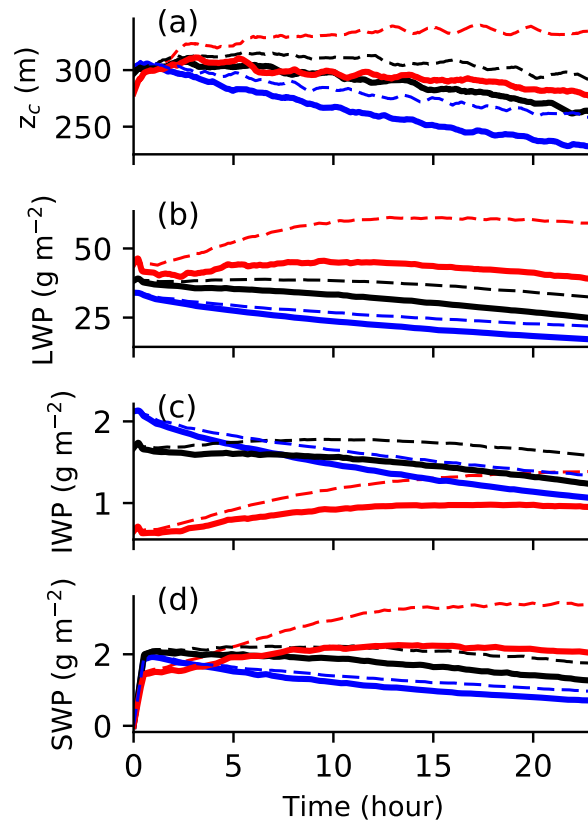


Figure 2.5: ISDAC-i timeseries of (a) cloud thickness, (b) liquid water path, (c) near-surface snow flux. Colors are the same as in Figure 2.4. Data are smoothed over 1 hour periods for better visualization.

that the clear sky values are an order of magnitude smaller than the radiative heating rates due to clouds. The cloudy radiative heating rate maximum nearly doubles as we move from the *cold* to the *warm* case.

When we increase the relative humidity above the inversion \mathcal{H}_f from 60% to 70%, similar sensitivities to Arctic warming are seen (dashed lines in Figure 2.4 to 2.7). Free-tropospheric specific humidity increases accordingly, reducing the entrainment drying at the cloud top. In the *cold* case, a weak moisture inversion, a frequently observed feature in the Arctic BL [16, 57], is present (Figure 2.4b). Turbulence is slightly weakened in the *baseline* and the *warm* cases (Figure 2.6), despite an increase in LWP with \mathcal{H}_f (Figure 2.5). One may expect that higher LWP is associated with stronger cloud-top radiative cooling, which drives increased turbulent mixing. This is indeed the case when \mathcal{H}_f is fixed while the other two parameters are varied. However, when we only increase \mathcal{H}_f , LWP increases, and turbulence weakens as

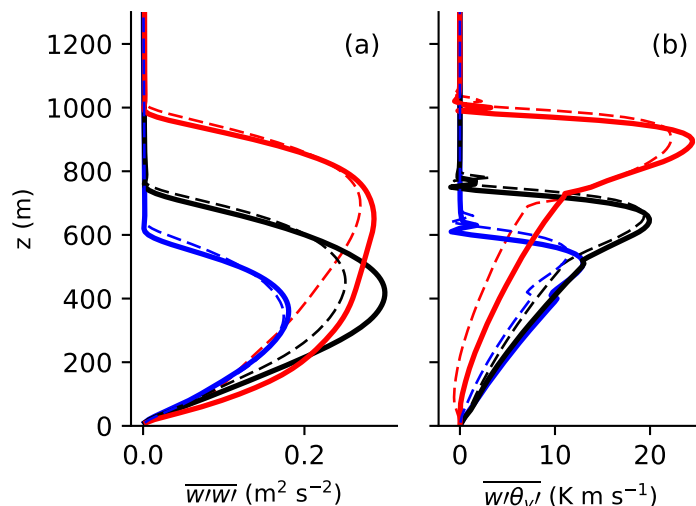


Figure 2.6: ISDAC-i domain mean profiles of (a) vertical velocity variance, and (b) vertical flux of virtual potential temperature, representing buoyancy production of TKE. Colors are the same as in Figure 2.4. Solid lines are from simulations with $\text{RH}=60\%$, and the dashed lines are with $\text{RH}=70\%$.

condensates increase.

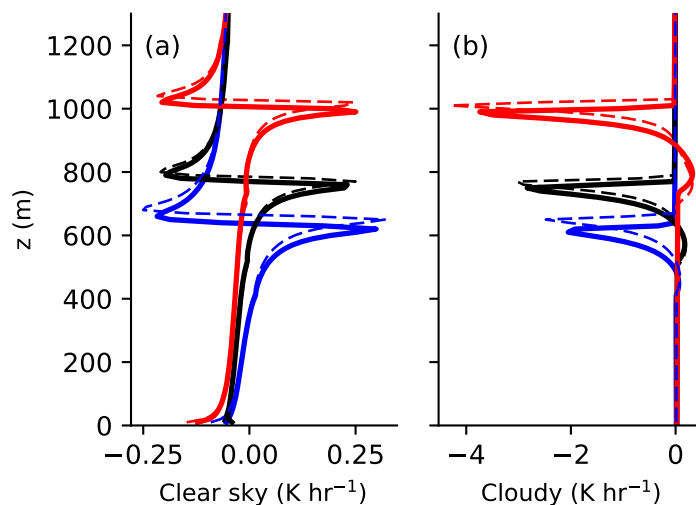


Figure 2.7: ISDAC-i domain mean profiles of (a) clear sky radiative heating rate, and (b) radiative heating rate due to cloud. Colors are the same as in Figure 2.4. Solid lines are from simulations with $\text{RH}=60\%$, and the dashed lines are with $\text{RH}=70\%$.

Having looked at the individual cases, next we present domain mean quantities averaged for the last hour of each simulation. We display the results in a gridded parameter space spanned by inversion strength (x -axis) and uniform temperature

change (y-axis). We first focus on cases with $\mathcal{H}_f = 60\%$. Figure 2.8 (top panels) show the LWP, IWP, and SWP of 16 simulations with $\mathcal{H}_f = 60\%$. LWP is sensitive to both the inversion strength and temperature: it decreases as the cloud-top inversion strengthens, and increases as the atmosphere warms uniformly. IWP, on the other hand, shows an opposite sensitivity to uniform warming. This is because with uniform warming, the ice fraction $1 - \lambda$ decreases strongly, notwithstanding that the total water path increases. Therefore, IWP decreases with uniform warming. In general, the amount of cloud ice is an order of magnitude less than cloud liquid, and it has negligible radiative effects on the BL. SWP responds mainly to inversion strength; it decreases as the inversion strengthens.

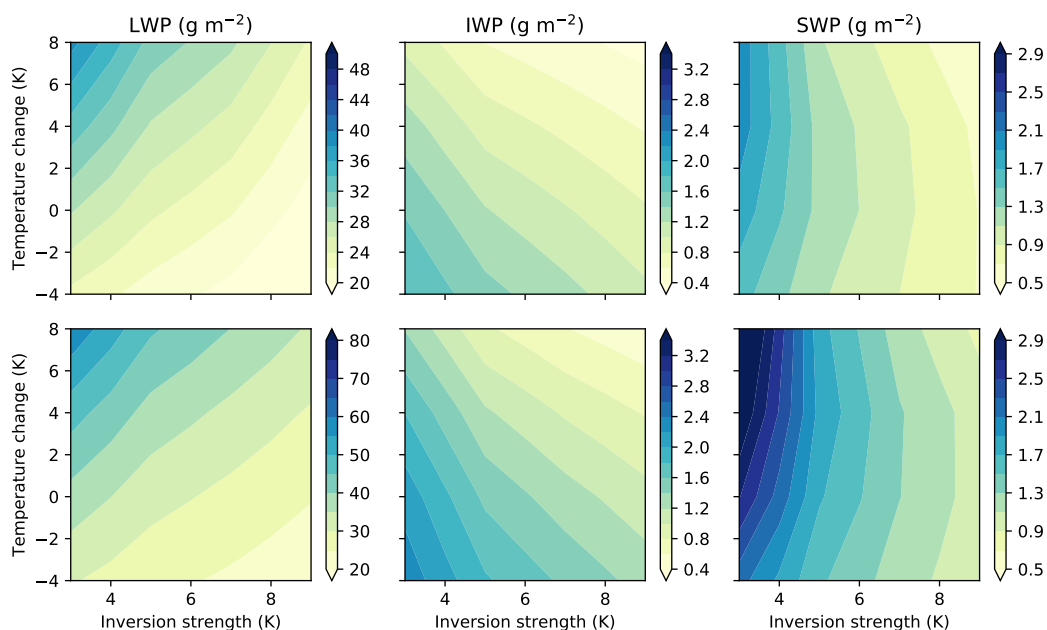


Figure 2.8: Liquid water path (LWP), ice water path (IWP), and snow water path (SWP) in LES ISDAC-i simulations averaged over the 24th hour. The horizontal axis shows the inversion strength, and the vertical axis shows uniform temperature change. Top panels show simulations with $\mathcal{H}_f = 60\%$, and bottom panels show simulations with $\mathcal{H}_f = 70\%$.

Another relevant quantity is the BL height z_i , here defined as the cloud top height (the first level from the top down that has non-zero q_l or q_i). As shown in Figure 2.9, z_i is mostly a function of inversion strength. The main processes that determine z_i are cloud-top entrainment and large-scale subsidence, as made explicit in the mass balance (2.2) of the MLM. In the MLM framework, w_e is inversely proportional to the inversion strength, as suggested by (2.5). Large-scale subsidence is fixed for

all cases. We thus expect z_i to decrease monotonically with inversion strength, as long as $\Delta_i F_R$ does not increase to compensate. Cloud base height z_b shows a similar sensitivity to z_i . Both z_i and z_b increases slightly with uniform warming. However, cloud thickness ($z_c = z_i - z_b$) decreases with uniform warming. This suggests that parameters in addition to w_e influence the sensitivity of z_b to uniform warming. We will discuss this further in the MLM section.

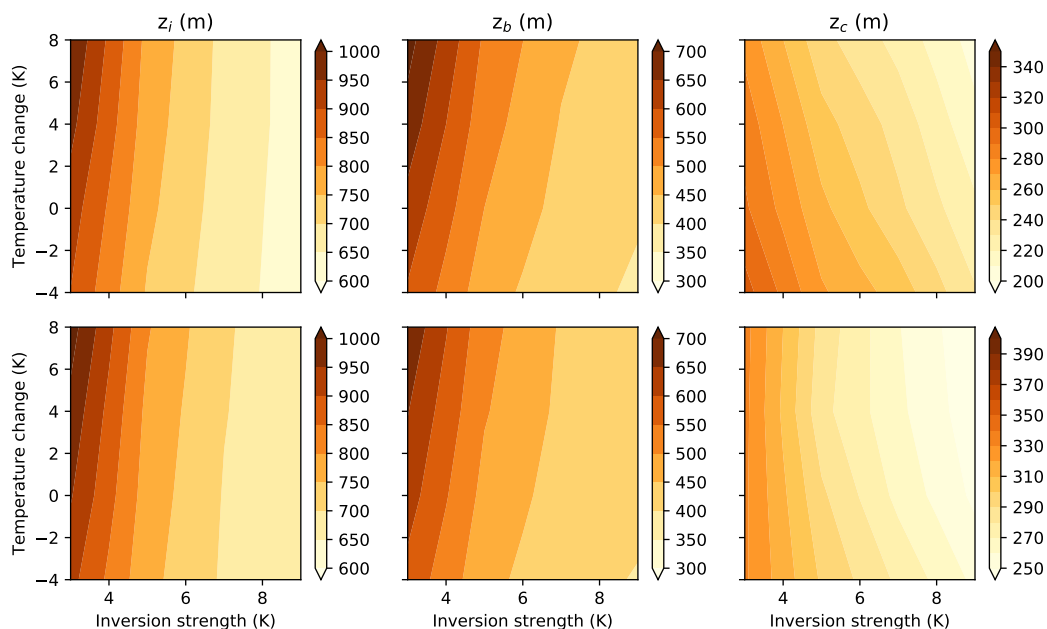


Figure 2.9: Same as Figure 2.8, but for LES cloud top height z_i , cloud base height z_b , and cloud thickness z_c .

Next we examine theoretically how LWP varies with temperature and inversion strength. The nearly adiabatic liquid layers in the ISDAC-i LES simulations allow us to approximate LWP as

$$\text{LWP} \approx \frac{1}{2} \rho_a z_c^2 \Gamma_l, \quad (2.8)$$

where Γ_l is the liquid water lapse rate. Hence, we can further decompose the fractional changes in LWP into contributions from fractional changes in z_c and Γ_l :

$$\frac{\delta \text{LWP}}{\text{LWP}} \approx \frac{\delta \Gamma_l}{\Gamma_l} + 2 \frac{\delta z_c}{z_c}. \quad (2.9)$$

Figure 2.10 shows the decomposition of LWP fractional changes referenced to the *baseline* simulation. LWP increases diagonally towards warmer and weaker inversion cases, resembling Figure 2.8 for the LES qualitatively. The increase of

LWP with temperature is due to increased Γ_l , as can be seen from the expression for Γ_l in the absence of precipitation,

$$\Gamma_l \equiv \frac{dq_l}{dz} = -\frac{dq_s(T)}{dz}. \quad (2.10)$$

For a saturated cloud layer, the moist static energy is conserved if hydrostaticity is assumed. Therefore,

$$c_p dT + g dz + L_v dq_s = 0,$$

which we can rearrange to get

$$\frac{dq_s}{dz} = -\frac{c_p}{L_v} \left(\frac{g}{c_p} + \frac{dT}{dz} \right). \quad (2.11)$$

By combining (2.10) and (2.11), we have an analytical expression for Γ_l :

$$\Gamma_l = \frac{c_p}{L_v} (\Gamma_d - \Gamma_m). \quad (2.12)$$

Figure 2.11 shows Γ_l and the fractional change of Γ_l with respect to temperature at 900 hPa, both plotted as functions of temperature. Because Γ_l is higher at warmer temperatures, its fractional change $(1/\Gamma_l)(d\Gamma_l/dT)$ decreases with temperature. Therefore, the liquid lapse rate effect is more potent at cold temperatures [58]. The ISDAC cloud base temperature is about 258 K, which gives 5.7% increase in Γ_l per K. This is more than three times the value for subtropical BL clouds (1.6 % per K increase at 290 K). The second term on the right hand side of (2.9) changes similarly to the cloud thickness (compare the third panels in Figures 2.9 and 2.10). Both $\delta\Gamma_l/\Gamma_l$ and $2\delta z_c/z_c$ are of comparable magnitudes given the parameter variations in ISDAC-i.

When \mathcal{H}_f is increased from 60% to 70%, the patterns of the main BL variables discussed above remain unchanged (compare bottom panels to top panels in Figures 2.8, 2.9, and 2.10). The most significant changes are the magnitudes of LWP and z_i . This is evident in Figure 2.10, where $2\delta z_c/z_c$ in the *warm* case becomes more dominant as \mathcal{H}_f increases. Cloud base height z_b is insensitive to \mathcal{H}_f , and thus the increase in z_c is due to higher z_i (Figure 2.9). In fact, the entrainment rate increases slightly with \mathcal{H}_f . One might expect that a drier free troposphere promotes

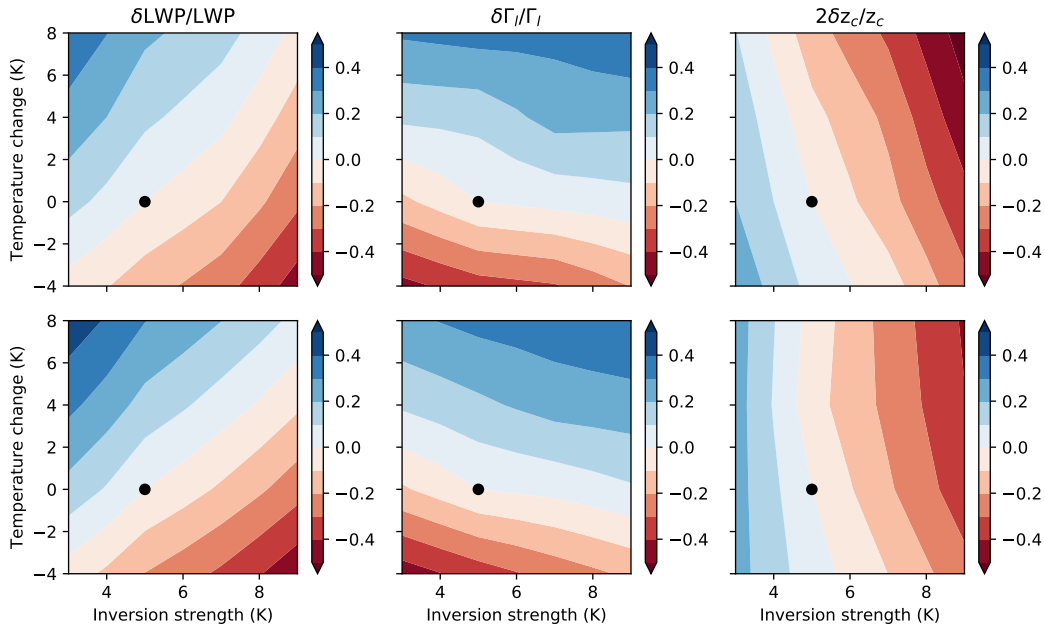


Figure 2.10: Same as Figure 2.8, but for LES estimated fractional LWP sensitivity $\delta\text{LWP}/\text{LWP}$, sensitivity due to fractional liquid lapse rate changes $\delta\Gamma_l/\Gamma_l$, and sensitivity due to fractional cloud thickness changes $2\delta z_c/z_c$. All sensitivities are referenced to the *baseline* simulation indicated by the black dots. (2.9) for definition of the terms in the text.

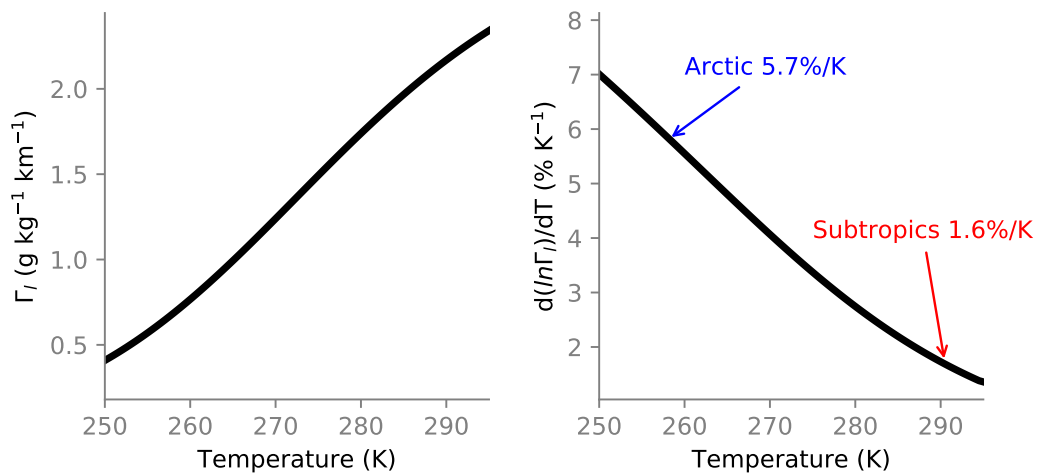


Figure 2.11: (Left) liquid water lapse rate and (right) fractional change of liquid water lapse rate with respect to temperature at 900 hPa. Typical values for Arctic and Subtropical temperatures are annotated.

stronger entrainment via the cloud top entrainment instability (CTEI) mechanism [59, 60]. We do not observe such mechanism in our ISDAC-i simulations. All of the

simulations without specific humidity inversion at the cloud top satisfy neither the original nor the modified CTEI criteria [60]. Here w_e increases with \mathcal{H}_f because more moisture is entrained from the cloud top to form liquid water, which increases the cloud-top radiative cooling rate and hence entrainment.

The use of a full radiative transfer model allows us to infer cloud radiative feedbacks from ISDAC-i simulations by looking at the top-of-atmosphere (TOA) cloud radiative effect (CRE_{LW}). It is defined as the difference between the all-sky and clear-sky TOA net longwave fluxes. Positive CRE_{LW} means the presence of clouds warms the atmosphere. As shown in Figure 2.12, CRE_{LW} decreases weakly with uniform warming, but much more prominently with a stronger temperature inversion. As the Arctic warms, CRE_{LW} increases, implying a positive LW cloud feedback at TOA. From *cold* to *baseline*, a near-surface temperature increase of 4 K is associated with 1.5 W m^{-2} increase of CRE_{LW} . From *baseline* to *warm*, the near surface temperature increase is 8 K, doubling that from *cold* to *baseline*, but CRE_{LW} only increases by 1.8 W m^{-2} . The estimated sensitivities are 0.37 and $0.23 \text{ W m}^{-2} \text{ K}^{-1}$ accordingly. If we look at the entire parameter range, the weakest sensitivity is associated with warming uniformly without changing the inversion strength. On the other hand, the strongest sensitivity involves minor uniform warming but significantly weaker inversions. The values vary from 0.015 to $0.85 \text{ W m}^{-2} \text{ K}^{-1}$, suggesting an important role the vertical structure of warming plays in high-latitude LW cloud feedbacks. By contrast, for a 10% increase in \mathcal{H}_f , changes in CRE_{LW} are negligible.

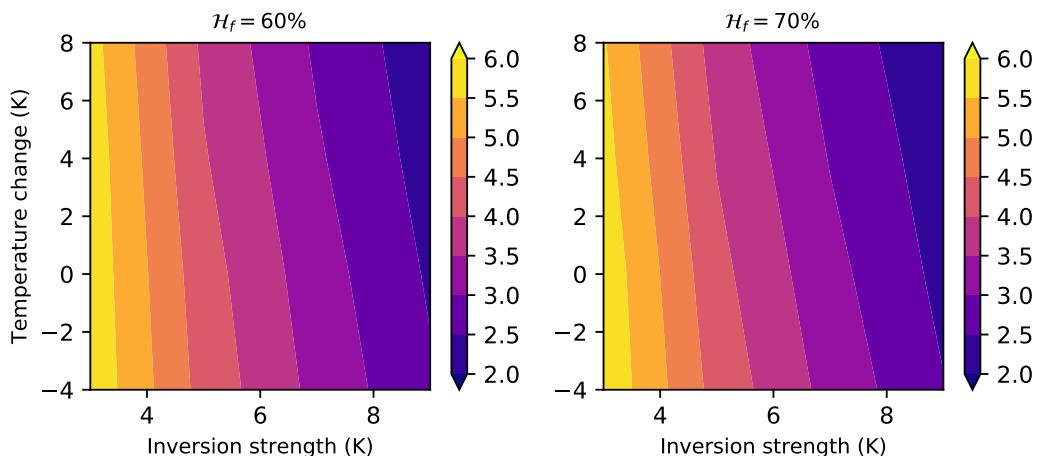


Figure 2.12: TOA longwave cloud radiative effect (W m^{-2}) for LES simulations with (left) $\mathcal{H}_f = 60\%$ and (right) $\mathcal{H}_f = 70\%$.

MLM

The same set of ISDAC-i simulations are run using the MLM. We will again analyze the results in the parameter space of inversion strength and temperature. Figures 2.13 to 2.14 are to be compared with Figures 2.8 to 2.10. Figure 2.15 compares the magnitudes of LWP, z_i and inversion properties in the two models. The most significant difference is in LWP, where the MLM produces a pattern with curved rather than linear contours (Figure 2.13). Most of the LWP gradients occur at cases with stronger inversions. LWP decreases with inversion strength and is insensitive to temperature change for cases with stronger inversion ($\Delta\theta_{li} \geq 7$ K). The minimal LWP occurs at $\Delta\theta_{li} = 9$ K, $\theta_{li,0} = 273$ K, whereas for LES it occurs at $\Delta\theta_{li} = 9$ K, $\theta_{li,0} = 261$ K.

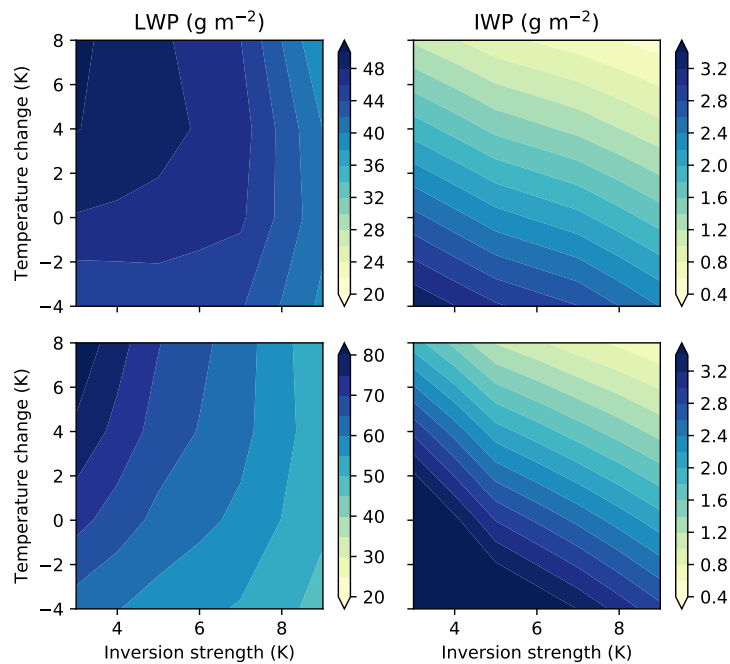


Figure 2.13: LWP and IWP in MLM ISDAC-i simulations averaged over the 24th hour. The horizontal axis shows the inversion strength, and the vertical axis shows uniform temperature changes. Top panels show simulations with $\mathcal{H}_f = 60\%$, and bottom panels show simulations with $\mathcal{H}_f = 70\%$.

The magnitude of LWP is significantly higher in MLM, especially for cases with $\mathcal{H}_f = 70\%$ (Figure 2.15a). The difference between MLM and LES LWP due to \mathcal{H}_f changes is nearly constant across cases, shown by the distance to the 1:1 line on Figure 2.15a. IWP is higher in the MLM than in LES, but how it varies with inversion strength and uniform temperature changes is very similar in the two models.

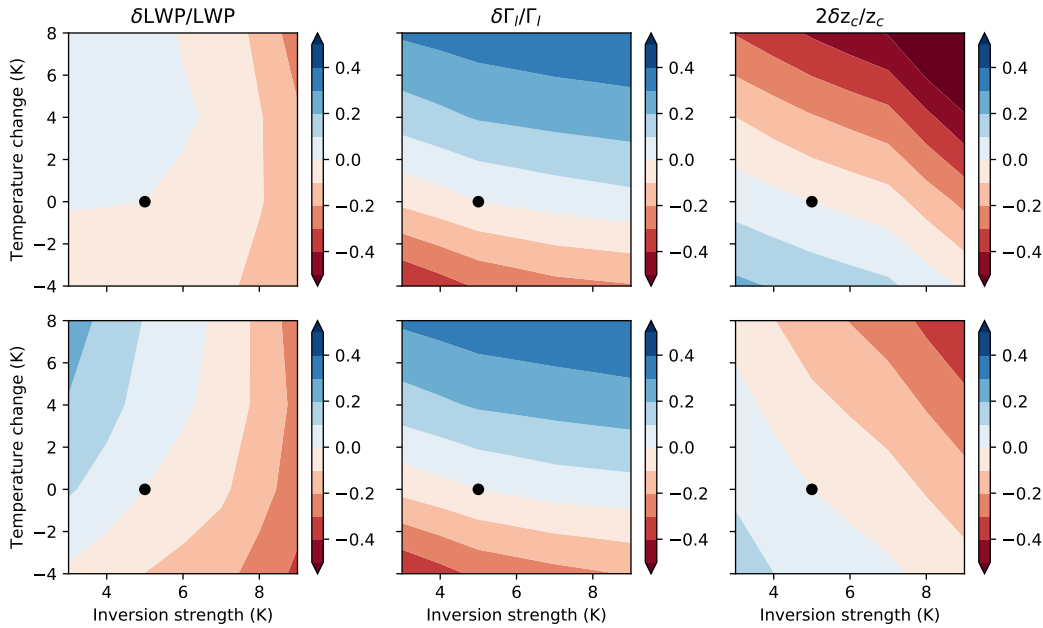


Figure 2.14: Same as Figure 2.13, but for MLM fractional LWP sensitivity $\delta\text{LWP}/\text{LWP}$, sensitivity due to fractional liquid lapse rate changes $\delta\Gamma_l/\Gamma_l$, and sensitivity due to fractional cloud thickness changes $2\delta z_c/z_c$. All sensitivities are referenced to the *baseline* simulation indicated by the black dots.

The higher condensate amount in MLM can be attributed to thicker cloud layers (Figure 2.16 and Figure 2.15b). On average, clouds are 50 m thicker in MLM than in LES. When the inversion is weak, cloud thickness is insensitive to uniform temperature changes in LES (z_i and z_b change at the same rate). This is not the case in MLM, due of a lack of direct response of entrainment to uniform temperature changes (see Eq. (2.5)). There is also a bias in z_b , mostly due to a mismatch in q_t . Because precipitation is weak in the ISDAC-i simulations, cloud-top entrainment is the main process that determines q_t .

In MLM, everything above z_i is prescribed and does not vary with time. In LES, processes such as radiation and subsidence can change the profiles of θ_{li} and q_t above the cloud top up to 1200 m. Above 1200 m, θ_{li} and q_t are nudged toward the initial profiles. The lapse rate right above the cloud top is smoothed due to radiative cooling, especially for cases with a strong inversion. Therefore, $\Delta\theta_{li}$ in MLM is slightly biased high compared to LES (Figure 2.15c). This explains the difference in entrainment rates between the models. Furthermore, right above z_i , subsidence dries the air and creates a vertically uniform q_t profile (instead of q_t decreasing with height in LES), making Δq_t in MLM biased high (Figure 2.15d). This leads to a

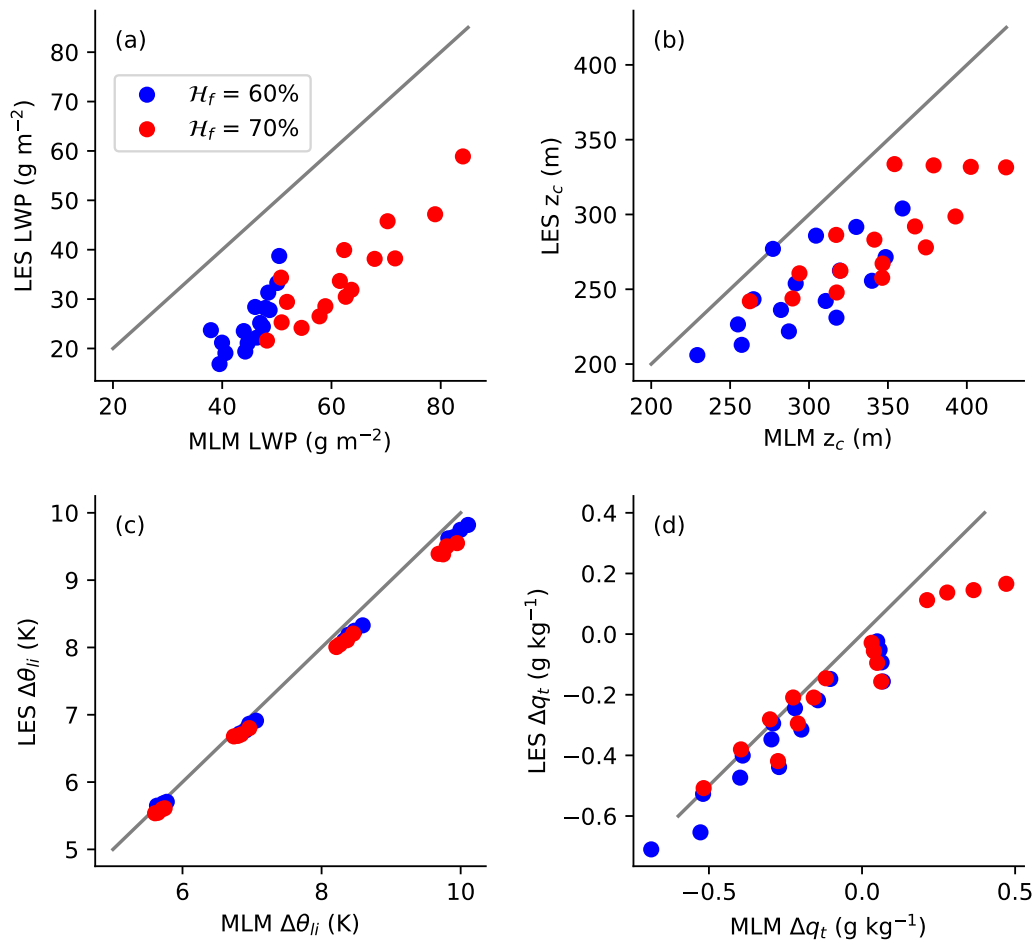


Figure 2.15: Scatter plots of (a) LWP, (b) cloud thickness z_c , (c) inversion strength $\Delta\theta_{li}$, and (d) specific humidity jump q_t , from ISDAC-i simulations averaged at the last hour from MLM (x-axis) and LES (y-axis). The gray lines indicate the 1:1 slope.

positive bias in MLM q_t values, which makes z_b lower than in LES.

In order to understand how cloud thickness changes, it is necessary to know what governs the changes of cloud base height z_b . We can derive the rate of change of z_b in the MLM framework. Start by defining

$$z_b = \frac{1}{\Gamma_d} (T_0 - T_{\text{LCL}}),$$

where Γ_d is the dry adiabatic lapse rate, and T_{LCL} is the temperature at the lifting condensation level, which is assumed to coincide with z_b . To compare the rate of

change of z_b to the mass balance (2.2), we differentiate

$$\frac{dz_b}{dt} = \frac{1}{\Gamma_d} \left(\frac{dT_0}{dt} - \frac{dT_{LCL}}{dt} \right). \quad (2.13)$$

The rate of change of surface temperature T_0 is implied by the energy balance (2.3). The temperature at z_b is T_{LCL} , defined as

$$q_t = q_s(T_{LCL}).$$

We can take the time derivative and use the chain rule to get the time rate of change of T_{LCL} ,

$$\frac{dT_{LCL}}{dt} = \frac{dq_t}{dt} \beta, \quad (2.14)$$

where

$$\beta = \left(\frac{dq_s}{dT} \Big|_{T_{LCL}} \right)^{-1}.$$

By plugging (2.14) into (2.13) and using

(2.3), (2.4), and (2.5), we find

$$\frac{dz_b}{dt} = \frac{1}{\Gamma_d z_i \rho_a c_p} \left[a \Delta_i F_R \left(1 - \beta \frac{\Delta q_t}{\Delta \theta_{li}} \right) - \Delta F_R \right]. \quad (2.15)$$

Cloud base height, unlike cloud top height, not only depends on entrainment rate, but also on temperature (through β), the total radiative flux contrast across the BL, and the specific humidity jump Δq_t .

Cloud base height z_b is controlled by several factors, and we focus on their relative importance. The first term in the squared bracket on the right hand side of (2.15) involves mostly entrainment processes such as contrasts of F_R , q_t , and θ_{li} across the cloud top. Embedded in the first term is the dependence on temperature through β , where β decreases with temperature. However, both Δq_t and $\Delta \theta_{li}$ increase strongly with inversion strength, which overcomes the temperature dependence of β . Consequently, the first term dominates z_b changes in the parameter ranges of ISDAC-i (Figure 2.16).

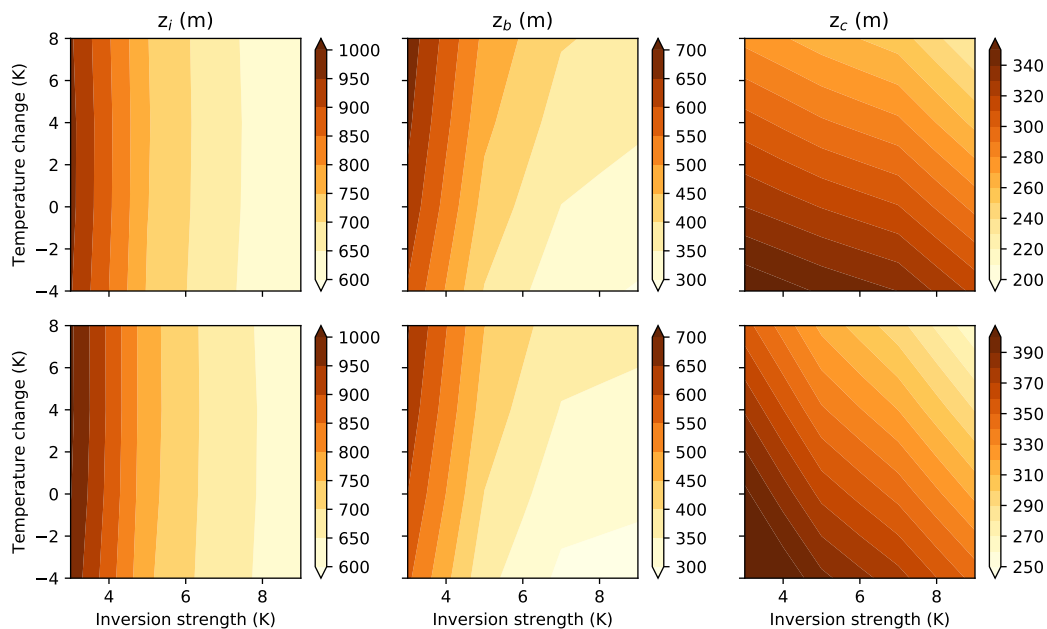


Figure 2.16: Same as Figure 2.13, but for MLM cloud top height z_i , cloud base height z_b , and cloud thickness z_c .

2.6 Discussion and Conclusions

To improve our understanding of the sensitivity of Arctic low clouds to climate change, we simulated a mixed-phase stratocumulus using the recently developed LES code PyCLES. The setup was based on the ISDAC LES intercomparison project, and the simulated BL agrees reasonably well with aircraft observations. Subsequently, we conducted sensitivity experiments in a modified ISDAC setup.

By varying parameters that control the initial BL structure, such as temperature, inversion strength, and free-tropospheric relative humidity, we explored the BL response to different climates in an idealized setting (termed ISDAC-i experiments). We showed that Arctic stratocumulus can be represented well with a MLM, as long as the BL does not become strongly decoupled. Most cases studied here have a cloud layer dominated by liquid, with amounts close to be adiabatic, despite an increase of sub-adiabaticity in cases with high free-tropospheric relative humidity.

The adiabatic LWP increases with $\theta_{li,0}$ and \mathcal{H}_f , and it decreases with $\Delta\theta_{li}$. This can be understood in the MLM framework through the dependence of the liquid water lapse rate and cloud thickness on the three parameters. Most of the LES have similar parameter dependencies as those exposed by the MLM, despite differences in the magnitude of the LWP sensitivities. The LWP response suggests a positive longwave

cloud feedback at TOA, as the Arctic moves toward a warmer state that is surface intensified so the inversion weakens. The sensitivity depends on the structure of warming, which varies from 0.015 to $0.85 \text{ W m}^{-2} \text{ K}^{-1}$. Cloud ice amounts are an order of magnitude smaller than liquid amounts, and ice has a small radiative effect on TOA budgets.

The ability of the MLM to reproduce LES results depends on the fact that the BL remains coupled in our ISDAC-i simulations. Microphysical processes have the potential to decouple the BL by transporting moisture from the cloud layer downward. Sublimation of snow in the sub-cloud layer may cool the air, thus leading to decoupling. In our simulations, microphysics alone were unable to decouple the BL in ISDAC-i. External forcing such as large-scale advection appears to be needed to maintain a decoupled surface layer [30].

The three parameters we chose to vary have implications for Arctic climate change. For example, surface amplified warming is likely to reduce the inversion strength capping the BL. When this occurs over sea ice, where surface fluxes are weak, we expect LWP to increase based on our experiments. A positive longwave cloud feedback results. If a decrease of free-tropospheric relative humidity accompanies warming in the Arctic, it would imply a change in LWP sensitivity to inversion strength and uniform warming (Figure 2.13).

Our study of the sensitivity of Arctic stratocumulus is largely inspired by the subtropical marine stratocumulus literature [33, 34]. The cloud thinning with uniform warming that we found in ISDAC-i is consistent with studies of subtropical stratocumulus. However, the LWP in subtropical stratocumulus decreases with uniform warming and cloud thinning, which is opposite to what we see in ISDAC-i. This is due to the fact that in ISDAC-i, q_l remains close to adiabatic and its response to warming overcomes the cloud thinning. As shown in Figure 2.11, we expect the fractional change of liquid water lapse rate to decrease in warmer temperatures. This seems to explain the weaker liquid water lapse rate effect in the subtropics. Also, our temperature perturbation is much larger than the 2-K perturbation that is used in most subtropical studies. The longwave cloud radiative effect we find from ISDAC-i is weak but positive. The strength of this LW cloud feedback also depends on inversion strength, and hence on the vertical structure of warming. Two features distinguish our study from the subtropical ones. First, surface heat fluxes are set to zero, so the surface fluxes do not respond to perturbations. Second, decoupling of the BL does not occur in the parameter ranges we explored.

The simplified ISDAC-i setup has its limitations. For example, we have not tested the sensitivities of the BL and clouds to surface fluxes. As sea ice extent continues to decline in the Arctic Ocean, surface heat fluxes will become more important in driving BL turbulence. A closed surface energy budget is needed to explore radiative feedbacks in a consistent manner. A next step is to investigate how such surface flux changes and other changes in the large-scale circulation can affect Arctic low-cloud cover more broadly.

2.7 Appendix: List of Symbols

Unless otherwise noted, subscripts 0 indicate near-surface values, superscripts + indicate values right above the BL top.

Γ_θ Potential temperature

Γ_d Dry adiabatic lapse rate

Γ_l Liquid water lapse rate

Γ_m Moist adiabatic lapse rate/lapse rate in the free troposphere

Δ Contrast across entire BL

Δ_i Contrast across entrainment zone

θ_{li} Potential temperature

θ_v Virtual potential temperature

κ Thermal conductivity of air

ρ_a Density of air

ρ_i Density of cloud ice

ρ_l Density of cloud liquid

a Entrainment coefficient

c_p Specific heat of air at constant pressure

D Water vapor diffusivity

F_R Longwave radiative flux

\mathcal{H}_f Relative humidity in the free troposphere

L Effective latent heat

L_v Latent heat of vaporization

- n Exponent in liquid fraction
- q_i Cloud ice water specific humidity
- q_l Cloud liquid water specific humidity
- q_s Saturation specific humidity
- q_{snow} Snow water specific humidity
- q_t Total water specific humidity
- R_v Gas constant for water vapor
- T Temperature
- T_f Freezing temperature of water
- T_i Homogeneous nucleation temperature
- T_{LCL} Temperature at lifting condensation level
- w_e Entrainment rate
- z_b Cloud base height
- z_c Cloud thickness
- z_i Cloud top/BL height

2.8 Appendix: MLM entrainment parameterization

Cloud-top entrainment rates w_e are diagnosed for all ISDAC-i LES simulations, using the mass balance equation (2.2). To parameterize w_e for MLM, we also diagnose $\Delta_i F_R$ and $\Delta\theta_{li}$ from the LES to get the linear-fit slope and intercept. The results are shown in Figure 2.17. Overall, we obtain a good fit for ISDAC-i simulations using (2.5). Nearly 90% of the entrainment comes from the direct contribution of cloud-top radiative cooling.

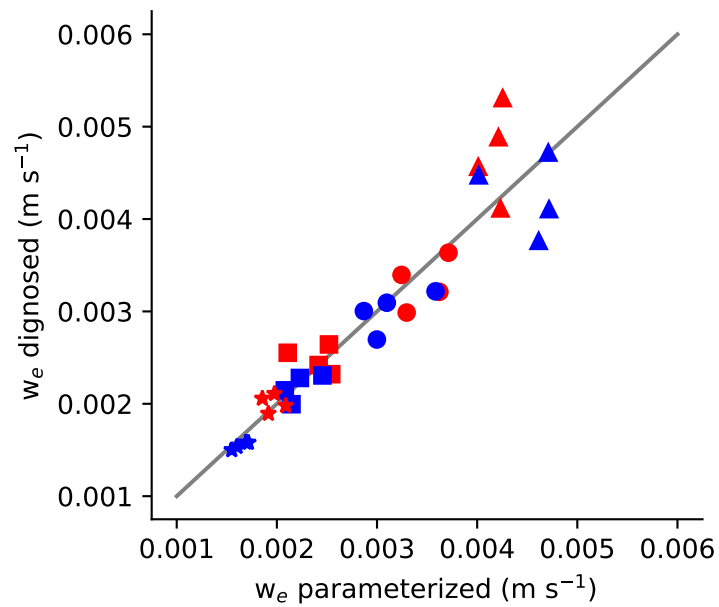


Figure 2.17: Entrainment rates diagnosed from ISDAC-i LES simulations using Eq. (2.2), and parameterized using Eq. (2.5). The slope coefficient $a = 0.85$ and the intercept $w_0 = 0.0004 \text{ m s}^{-1}$ are from a linear fit, with $r^2 = 0.89$. Blue markers show simulations with $\mathcal{H}_f = 60\%$, and red with $\mathcal{H}_f = 70\%$. Marker types distinguish inversion strengths: 3 K (triangles), 5 K (circles), 7 K (squares), 9 K (stars).

CASE STUDIES OF ARCTIC BOUNDARY LAYER CLOUDS

3.1 Abstract

A proper representation of the cloudy Arctic boundary layer is essential for getting the correct surface energy balance. We simulated two Arctic model intercomparison cases using the Python Cloud Large Eddy Simulation code, and compared our results to observations and model intercomparison results. Overall, our model captures the main features of Arctic boundary layer clouds, though further development on the microphysical scheme is needed to better simulate the vertical structure of ice condensates.

3.2 Introduction

The objective of this chapter is to provide further validation for the Python Cloud Large Eddy Simulation code (PyCLES) to simulate Arctic boundary layer clouds. In addition to the ISDAC case presented in the previous chapter, we present two more commonly used case studies that are based on field campaigns and have model intercomparison studies. They both contain a number of LES or cloud-resolving model (CRM), and observational data to be compared with PyCLES.

The Surface Heat Budget of Arctic Ocean (SHEBA) experiment is a year-long field campaign that provides continuous observations of an atmosphere-ocean column in the Arctic in 1997-1998. On May 7, 1998, a persistent mixed-phase boundary layer was observed together with aircraft measurements from the First ISCCP Regional Experiment – Arctic Cloud Experiment. A modeling intercomparison based on observations was conducted by Morrison *et al.* [41].

The Mixed-Phase Arctic Cloud Experiment (M-PACE) is a field campaign conducted over northern Alaskan coast that focuses on mixed-phase cloud processes. The field campaign inspired two model intercomparison studies, one focuses on multilayered mixed-phase cloud system [61], and the other focuses on a single-layer mixed-phase cloud [62]. Here we will focus on the latter case.

These two cases span a wide range of cloud conditions. The cloud in SHEBA is very thin (low LWP) and polluted (high droplet number concentration), while the cloud in M-PACE is thick (high LWP) and clean (low droplet number concentration).

The cloud in ISDAC, presented in the previous chapter, lies somewhere in between SHEBA and M-PACE. The dominant microphysical processes also vary, where SHEBA is dominated by light snow, and M-PACE is dominated by snow and riming. In terms of difficulty in representing the microphysical processes, SHEBA is often considered the simplest case study since no collisional processes are active [55].

We will briefly describe the LES setup, and then present the results from SHEBA and M-PACE separately, followed by conclusions.

3.3 LES Setup

We use PyCLES [15] to simulate two LES intercomparison case studies. The model setup closely follows the ISDAC intercomparison study presented in Chapter 2. We use WENO5 advection scheme for momentum and scalars, and 3rd-order Runge-Kutta scheme for time-stepping. The Smagorinsky-Lilly SGS scheme is only active for momentum transfer between the surface and the lowest LES level [37]. Radiative transfer is calculated with the RRTMG model [43], where the domain is divided into sub-columns for RRTMG calculations. Ice generalized effective size needed for RRTMG is calculated based on empirical formula by Boudala *et al.* [45]. The horizontal resolution is 50 m, and the vertical resolution is 10 m. The domain size is $3.2 \text{ km} \times 3.2 \text{ km} \times 2.5 \text{ km}$.

Intercomparison studies usually prescribe large-scale forcing based on reanalysis data. For horizontal advection, profiles of temperature and moisture tendencies are provided. We convert these tendencies to specific entropy tendency for PyCLES. For subsidence, large-scale vertical velocity is usually provided. Given that our model uses specific entropy instead of liquid-ice potential temperature, the vertical advection is computed directly with applying the subsidence on specific entropy.

We use a single-moment ice microphysics scheme that is adapted for Arctic mixed-phase stratocumulus [38, 39]. It uses a temperature-dependent function to diagnose cloud liquid and ice that are at thermodynamic equilibrium with water vapor. Figure 3.1 shows the liquid fraction as a function of temperature, computed using the formulation in Kaul *et al.* [38]. This function ensures about 80% of liquid at 240 K, which is often observed in the Arctic stratocumulus. Snow and rain are prognostic, and have their own prognostic sedimentation velocities, while the cloud condensates are stationary. We use a constant particle size distribution function (PSDF) intercept parameter $N_{0,ice}$ of 10^7 m^{-4} for the ice number concentration. The details of the microphysics can be found in Kaul *et al.* [38] and Chapter 2.

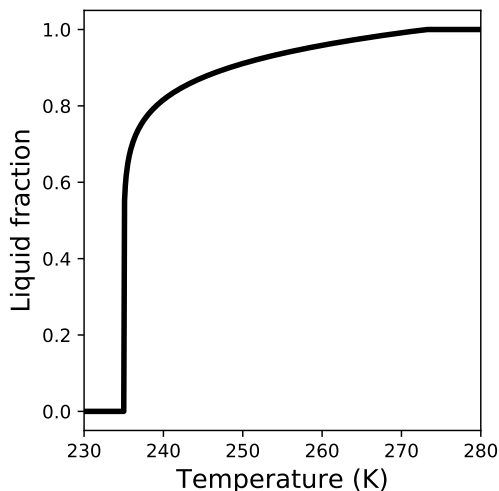


Figure 3.1: Liquid fraction as a function of temperature, computed using the formulation in Kaul *et al.* [38] with the exponent equals 0.1.

3.4 SHEBA Case Study

Case Description

During the year-long campaign of SHEBA, a case of persistent mixed-phase BL cloud on May 7 1998 was selected for CRM and LES intercomparison study [41]. The observed cloud during 1200 to 2400 UTC May 7 1998 was above sea ice, and had light snow showers reaching the surface. The BL was relatively well-mixed from the surface, primarily driven by cloud top cooling. Surface buoyancy flux is weak due to the presence of sea ice. The inversion strength at the cloud top was 5–6 K, while the BL height decreased during this period from 630 m to 400 m with a corresponding decrease of LWP. The large-scale forcing is based on the ECMWF analysis data constrained by SHEBA observations. There is uncertainty associated with the analysis data used to provide the large-scale forcing fields [41]. The PyCLES setup follows the intercomparison closely [41]. In order to match the observed temperature and liquid water profiles, we recalculated the initial θ_l and q_t profiles, using the definition of θ_l in Ovchinnikov *et al.* [32], which is possibly different from the θ_l definition in Morrison *et al.* [41].

Results

Figure 3.2 shows the domain mean profiles averaged over the last 30 minutes of the simulation. The BL height has decreased from 465 m to 445 m. The free troposphere has cooled slightly, and the BL has warmed and moistened. The inversion across

the cloud top has weakened for about 2 K. The total water is well-mixed in the BL, while a water vapor q_v inversion lies above the liquid layer (Figure 3.2b). This is consistent with the often-observed humidity inversion in Arctic stratocumulus [16]. The q_l maximum has doubled from 0.1 to 0.2 g kg⁻¹, while the cloud base is almost at the surface at the end of the simulation (Figure 3.2c). The total ice condensate amount that combines cloud ice and snow is an order of magnitude less than q_l (Figure 3.2d). The total ice number concentration at the cloud top is 1.75 L⁻¹, which is very close to the prescribed value of 1.7 L⁻¹ in the intercomparison.

Figure 3.3 shows the time series of liquid and total ice water paths for the 12-hour period. Both quantities steadily increase for the first 6 hours of the simulation, then reach a steady-state around the 8th hour. LWP averaged for the last 30 minutes is 64 g m⁻², and IWP and SWP combined is 6.5 g m⁻².

We can compare our simulation with model results from Morrison *et al.* [41]. The intercomparison models disagree on the BL height at the end of the simulation, which vary from 350 to 450 m. Domain mean profiles of θ_l and q_t show significant spread across the model intercomparison. The BL θ_l varies between 256 to 258.3 K, while PyCLES lies within this spread (Figure 3.2a). The θ_l spread is attributed to the different radiative cooling rate profiles across models, which are determined by the cloud condensate amounts. In the free troposphere, PyCLES has a cooler θ_l than nearly all intercomparison models. The BL q_t varies between 0.85 to 1.1 g kg⁻¹ in the intercomparison, while PyCLES is at the moist end (Figure 3.2b).

Given the large spread in the simulated BL states in the intercomparison, we expect the cloud condensates to vary widely as well. Indeed, the cloud liquid maximum ranges from 0.06 to 0.22 g kg⁻¹. In the model with the highest cloud liquid amount, the liquid layer has reached the surface with a mixing ratio of 0.05 g kg⁻¹. The spread is also evident in the ice mixing ratio profiles, where it varies between 0.001 to 0.015 right above the surface. The simulated LWP and total IWP at the end of the simulations by the intercomparison models are shown on Figure 3.3. The spread is significant in both quantities, and one of the models even has zero LWP due to total glaciation of the cloud, which is certainly in disagreement with the observations. Although our simulation lies within the range of the model intercomparison results, there is an obvious over-estimation of cloud condensates and precipitation when compared to observed water paths during the entire 12-hour period.

In order to better understand the differences between results from PyCLES and the model intercomparison, we conduct a budget analysis for the conserved variables.

Figure 3.4 shows the decomposition of s and q_t tendencies at the beginning and the end of the simulation. We split the tendencies into four categories: radiative tendency (not for q_t), tendency due to microphysics, advective tendency that is dominated by resolved vertical advection, and forcing tendency. Forcing consists of the prescribed large-scale horizontal advection that is time-invariant, and subsidence with prescribed vertical velocities.

For specific entropy, radiative cooling is largely balanced by vertical advection and subsidence warming in the cloud (Figure 3.4a). The initial subsidence warming is greater than radiative cooling at the cloud top. At the end of the simulation, subsidence warming is significantly reduced at the cloud top (Figure 3.4c). This is because of the weakened cloud top inversion, as entrainment and the large-scale forcing continue to cool the free troposphere and warm the BL (Figure 3.2). Throughout the entire period, microphysics contribute little to the entropy budget. This is not surprising, given that q_{snow} is more than an order of magnitude less than q_l (Figure 3.2c and d). In the free troposphere, the prescribed large-scale cooling is meant to balance subsidence warming. However, in our simulation the radiative cooling right above the cloud top is significant due to q_v inversion (Figure 3.2b).

The moisture budget shows a different time evolution. Initially, the most significant tendency is due to large-scale forcing (Figure 3.4b). The prescribed q_t horizontal advection rapidly moistens the BL, while the free troposphere q_t remains at the initial value. At the cloud top, subsidence drying is partially offset by turbulence moistening. Eventually the q_t gradient at the cloud top is enhanced. At the end of the simulation, a q_t balance at the cloud top is achieved where subsidence drying and microphysical removal of water are counteracted by turbulence moistening (Figure 3.4d). The microphysical processes become more active as the cloud layer grows and thickens.

In Morrison *et al.* [41], the water vapor budget reflects a leading balance between condensation and q_v flux convergence. These terms are nearly an order of magnitude greater than the large-scale forcing. In our q_t analysis, forcing and microphysical processes have the same order of significance in the cloud. This difference may arise from different microphysical parameterizations and numerical schemes.

A sensitivity test in Morrison *et al.* [41] involves changing the total ice number concentration. We also tested the sensitivity of PyCLES by increasing the ice PSDF intercept parameter $N_{0,ice}$ to $3 \times 10^7 \text{ m}^{-4}$. The simulated LWP is 14 g m^{-2} lower, and IWP is 0.4 g m^{-2} higher. These changes are consistent with the trends in

Morrison *et al.* [41], but complete glaciation of cloud does not happen in PyCLES, and only one of the six intercomparison models behaves similarly to PyCLES. Here, the decrease in LWP and IWP are attributed to increased depletion of moisture by autoconversion and sedimentation of snow [38].

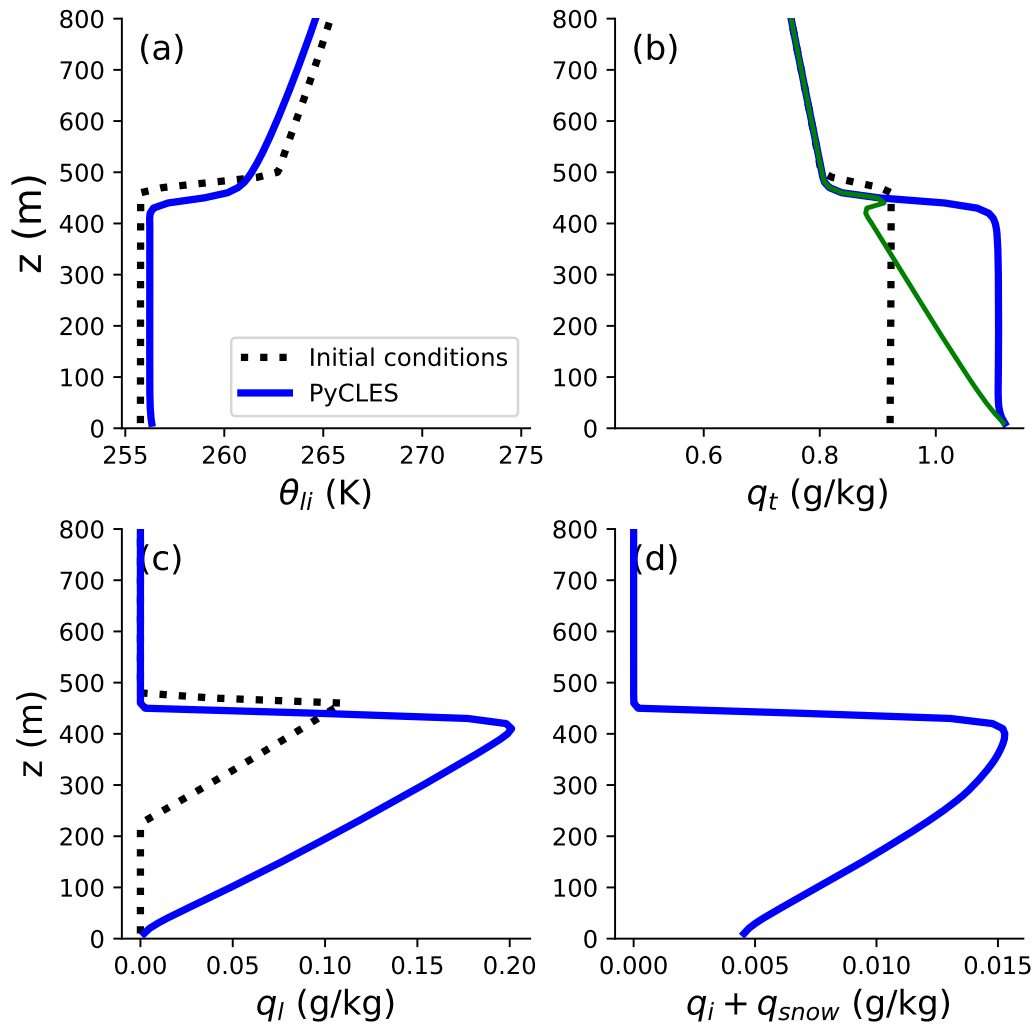


Figure 3.2: SHEBA domain mean profiles of (a) liquid ice potential temperature θ_{li} , (b) total water specific humidity q_t (with water vapor specific humidity in green), (c) cloud liquid water specific humidity q_l , and (d) total ice water specific humidity ($q_i + q_{snow}$). Dashed lines show the initial profiles, and blue lines show the average over the last 30 minutes.

3.5 M-PACE Case Study

Case Description

The observed single-layer stratocumulus during 1700 UTC 9 October to 0500 UTC 10 October 2004 formed under cold-air outbreak conditions. Cold air above sea

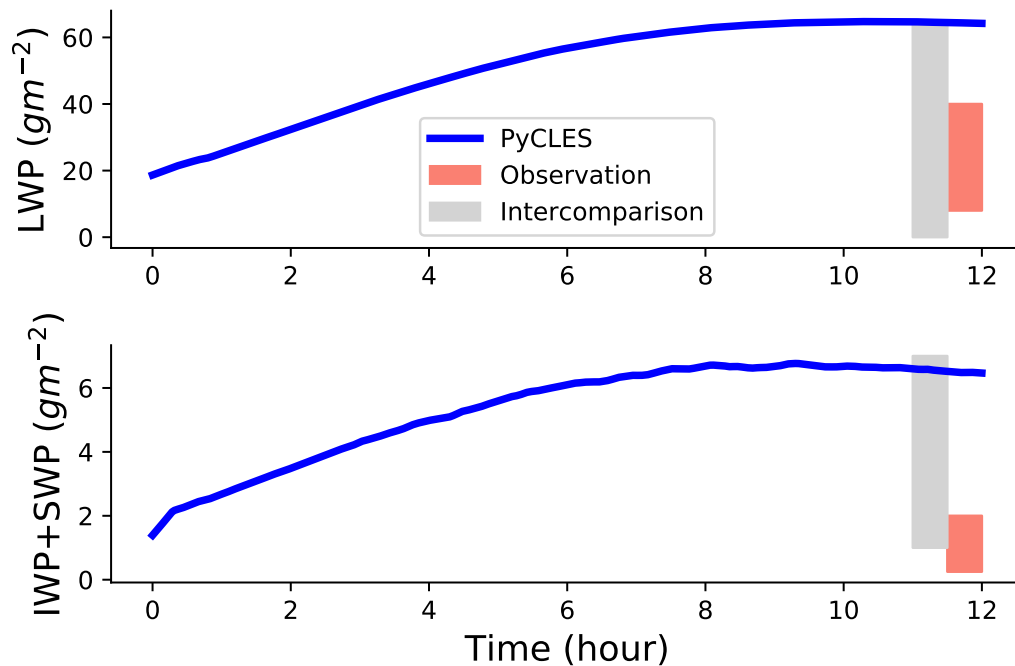


Figure 3.3: SHEBA time series of (a) liquid water path, and (b) total ice water path. Also shown are the LES intercomparison ranges in gray shadings, and the observed ranges of values in red.

ice northeast of Alaska flowed over the ice-free Beauford Sea north of Barrow and Oliktok Point, Alaska. Significant surface sensible and latent heat fluxes were observed, which provided heat and moisture for the well-mixed boundary layer. Although the BL dynamics and microphysical processes in M-PACE are more vigorous than SHEBA, it is still not complicated by multilayer cloud system, nor strong cloud feedbacks. The ample and high-quality observational data also make the case suitable for bench-marking LES models [62].

The initial conditions are based on sounding profiles at 1700 UTC 9 October 2004 at Barrow. Large-scale forcing is based on analysis data from the European Centre for Medium-Range Weather Forecasts (ECMWF). The PyCLES setup follows Klein *et al.* [62] closely.

Results

Domain mean profiles are shown in Figure 3.5. The BL experiences a slight cooling of less than 1 K and drying of about 0.2 g kg^{-1} during the simulation, while the BL deepens for about 150 m. The surface is noticeably warmer and moister than the BL, as a result of significant prescribed sensible and latent heat fluxes. The water

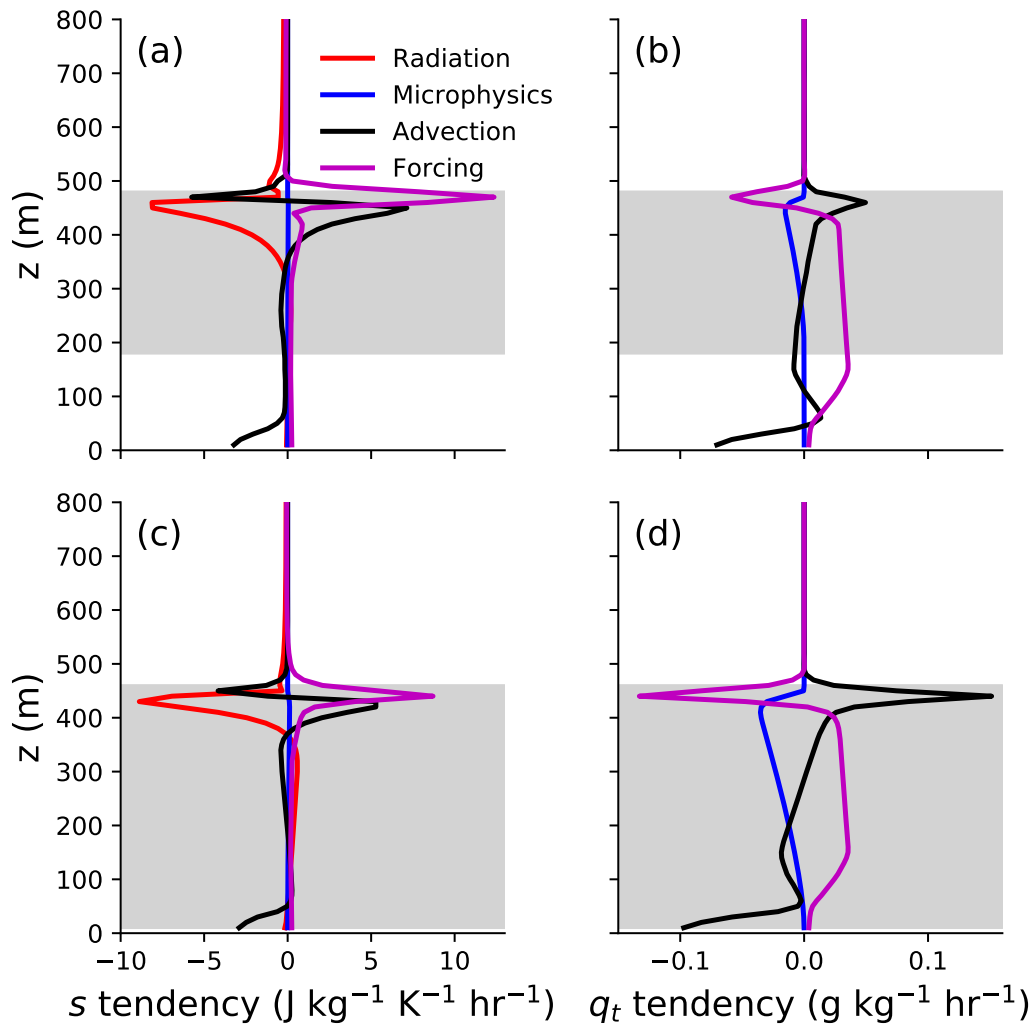


Figure 3.4: SHEBA domain mean profiles of time tendencies for (a, c) specific entropy ds/dt , and (b, d) total water specific humidity dq_t/dt . Averages are calculated for the first (top) and the 12th (bottom) simulated hours. Gray shading corresponds to the liquid layer.

vapor q_v profile shows no moisture inversion at the cloud top (Figure 3.5b), different from the SHEBA case (Figure 3.2b). The liquid cloud layer has a q_l gradient that is very close to adiabatic (Figure 3.5c). The peak cloud ice q_i is 10% of q_l , and there is a significant amount of snow reaching the surface (Figure 3.5d).

Next, we compare results from PyCLES to those from the cloud-resolving models (CRM) in Klein *et al.* [62]. Single-column model (SCM) results are excluded for comparison, because a SCM works very differently from LES/CRM. While θ_{li} and q_t are within the LES intercomparison range, the maximum of q_l is slightly higher

than the intercomparison. The maximum ice specific humidity is comparable to the intercomparison value, but the vertical structure is drastically different. The peak occurs at cloud top in PyCLES, while the other LES models have their peaks at cloud base. The snow profile q_{snow} also has its peak at the cloud base in PyCLES (not shown). Since there is no sedimentation of cloud ice, q_i takes the same shape as q_l , which has a cloud-top maximum. Near the surface, q_{snow} in PyCLES is nearly twice as much as the maximum LES intercomparison result. The maximum in-cloud total ice number concentration is 2.5 L^{-1} , close to the aircraft observed value of 2.0 L^{-1} . Although the intercomparison model median agrees well with the observation, the range varies for five orders of magnitude.

There is significant variability in the aircraft observed cloud condensation amounts, given that the dataset consists of 32 vertical profiles over cloud “rolls” [62]. We can still compare the cloud top liquid water content (LWC) observed by aircraft with our results. The observed LWC median is 0.33 g m^{-3} , and the maximum reaches 0.5 g m^{-3} . The spread in the observed ice water content (IWC) is even larger, with a median of 0.026 g m^{-3} at the cloud base, and the total range covers 0 to 0.2 g m^{-3} . Our cloud top LWC is 0.4 g m^{-3} , and cloud base IWC is 0.02 g m^{-3} . Thus, our results reach reasonable agreement with the observed cloud state during M-PACE.

Figure 3.6 shows the time series of cloud water paths. LWP steadily increases and reaches 220 g m^{-2} at the end of the simulation, higher than all LES intercomparison values, but agrees well with ground-based retrieved value at Barrow [62]. The ground-based LWP at Barrow is much higher than aircraft observations, given the geographical variability of the cloud properties. For example, the combined flights LWP is $98.3 - 135.7 \text{ g m}^{-2}$, while the LWP from SHUPE-TURNER at Barrow ranges from 172.3 to 280.8 g m^{-2} . For IWP, PyCLES lies within the LES intercomparison range, but slightly below the observed values at Barrow that ranges from 19.2 to 42.8 g m^{-2} .

Our results are closer to observations than the majority of the CRMs which has a median LWP of 57.3 g m^{-2} . Although in their study, Klein *et al.* [62] pointed out that models with more sophisticated microphysics tend to have higher LWP that is closer to the observed LWP, our results contradict their point. Only one of the CRMs in Klein *et al.* [62] uses a single-moment scheme with temperature-dependent partitioning, and its estimated LWP is only 23.3 g m^{-2} . The three models that have LWPs higher than 100 g m^{-2} use either bin microphysics or double-moment schemes, and their IWPs are still lower than the observed range. This points out that

microphysics is not the only factor that leads to disagreement across models.

Budget analysis of the prognostic scalars s and q_t are shown on Figure 3.7 for the beginning and the end of the simulation. For s budget, there is little change with time except for processes at the cloud top. The prescribed large-scale horizontal advection acts to cool and dry the BL. In the sub-cloud layer, resolved vertical advection balances the cooling by transport heat upward from the surface. Microphysics again plays a minor role in the entropy budget, but becomes increasingly important for q_t . The microphysical tendency for q_t in M-PACE is nearly an order of magnitude greater than in SHEBA. Precipitation forms in the cloud layer, and transport water downward via sedimentation, then sublimation of snow occurs in the sub-cloud layer.

Given that microphysics is more active in M-PACE than in SHEBA, we can further analyze the budget of q_{snow} . Figure 3.8 shows the various components of the snow budget in the BL. Autoconversion, accretion, and vapor deposition are the main processes that form snow in the cloud layer. These are balanced by transport, mainly sedimentation of snow. In the sub-cloud layer, resolved vertical turbulent transport and sublimation of snow nearly balance each other. One thing that distinguishes M-PACE from SHEBA and ISDAC is the accretion term. In both SHEBA and ISDAC, accretion is negligible (also see Kaul *et al.* [38]). Observations suggest that during M-PACE, the cloud temperature favors dendrites, and the high LWP condition of M-PACE encourages active riming that eliminates dendrites. The colder temperatures during SHEBA do not favor dendritic growth, and thus accretion is hardly active [55]. Although we do not resolve different snow species in our microphysics scheme, our results are generally consistent with the observed features of Arctic stratocumulus.

We conducted a liquid-only simulation to further compare PyCLES to the intercomparison models. LWP is 327 g m^{-2} in PyCLES, while it varies between 65 to 330 g m^{-2} in Klein *et al.* [62]. The model that simulated a LWP of 330 g m^{-2} without ice microphysics has very different LWP and IWP in the baseline simulation compared to PyCLES. Mainly, the ice precipitation is so efficient at removing moisture in this model that LWP is only 23.3 g m^{-2} . Klein *et al.* [62] concluded that the liquid to ice conversion in most of the intercomparison models is too exaggerated, which led to an overall underestimation of LWP.

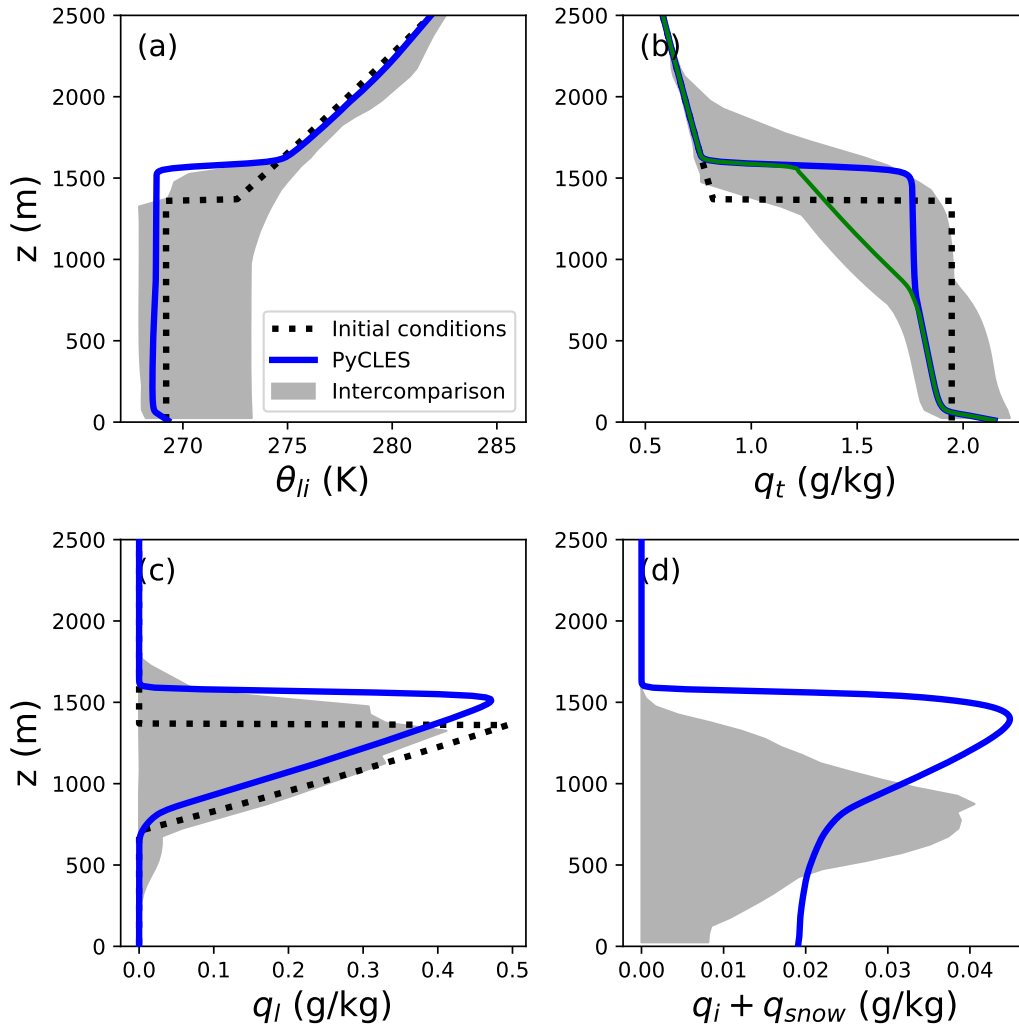


Figure 3.5: M-PACE domain mean profiles of (a) liquid ice potential temperature, (b) total water specific humidity, (c) cloud liquid water specific humidity, and (d) total ice water specific humidity. Black dotted lines show the initial conditions, blue lines show PyCLES averaged for the last 9 hours of the simulation. Gray shadings show the LES intercomparison results from Klein *et al.* [62].

3.6 Conclusions

We have presented two case studies of Arctic BL clouds based on observation: SHEBA with a persistent stratocumulus layer, and M-PACE with rolled clouds during a cold-air outbreak event. In both cases, PyCLES maintains well-mixed cloud-topped BLs.

For SHEBA, our simulated LWP lies in the upper range of the model intercomparison. The BL has moistened significantly due to the prescribed forcing, and the cloud layer has nearly reached the surface. The evolution of the BL differs from the

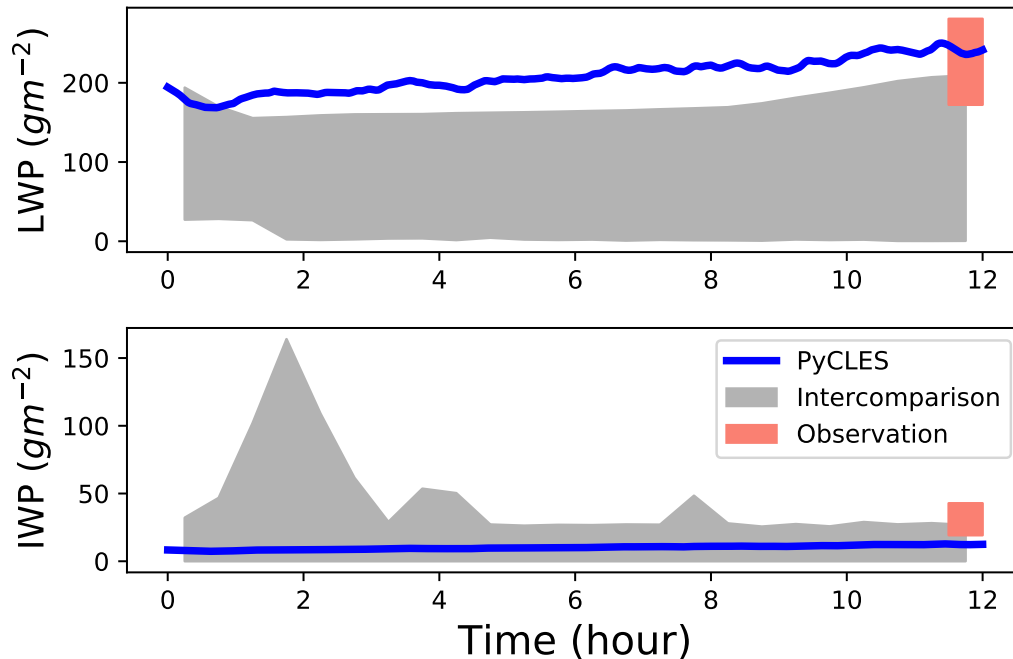


Figure 3.6: M-PACE time series of (a) liquid water path, and (b) total ice water path. Also shown are the LES intercomparison range in gray shading, and the observed range of values in red.

observations: the observed BL shallowed and the LWP decreased through the 12 hours, but we find a steady increase in LWP in PyCLES. Observed precipitation in SHEBA was weak, thus the discrepancy in the modeled BL evolution is mainly due to the inconsistent prescription of large-scale forcing.

M-PACE is associated with a liquid-rich stratocumulus with more intense precipitation than SHEBA. The thermodynamic structure of our simulated BL is within the intercomparison range. Although our LWP is slightly above the intercomparison range, it is within the observational range. IWP agrees with the intercomparison models, but is slightly underestimated when compared to observations.

More attention should be paid to the setup of intercomparison studies, especially in the large-scale forcing fields. For example, M-PACE did a better job in prescribing the large-scale forcing profiles, given that the BL does not drift significantly from the initial conditions. Klein *et al.* [62] also included more observational data in the study than SHEBA so that it is easier for models to use M-PACE as a benchmark for simulating Arctic stratocumulus.

The results from the two case studies are overall encouraging. We summarize the

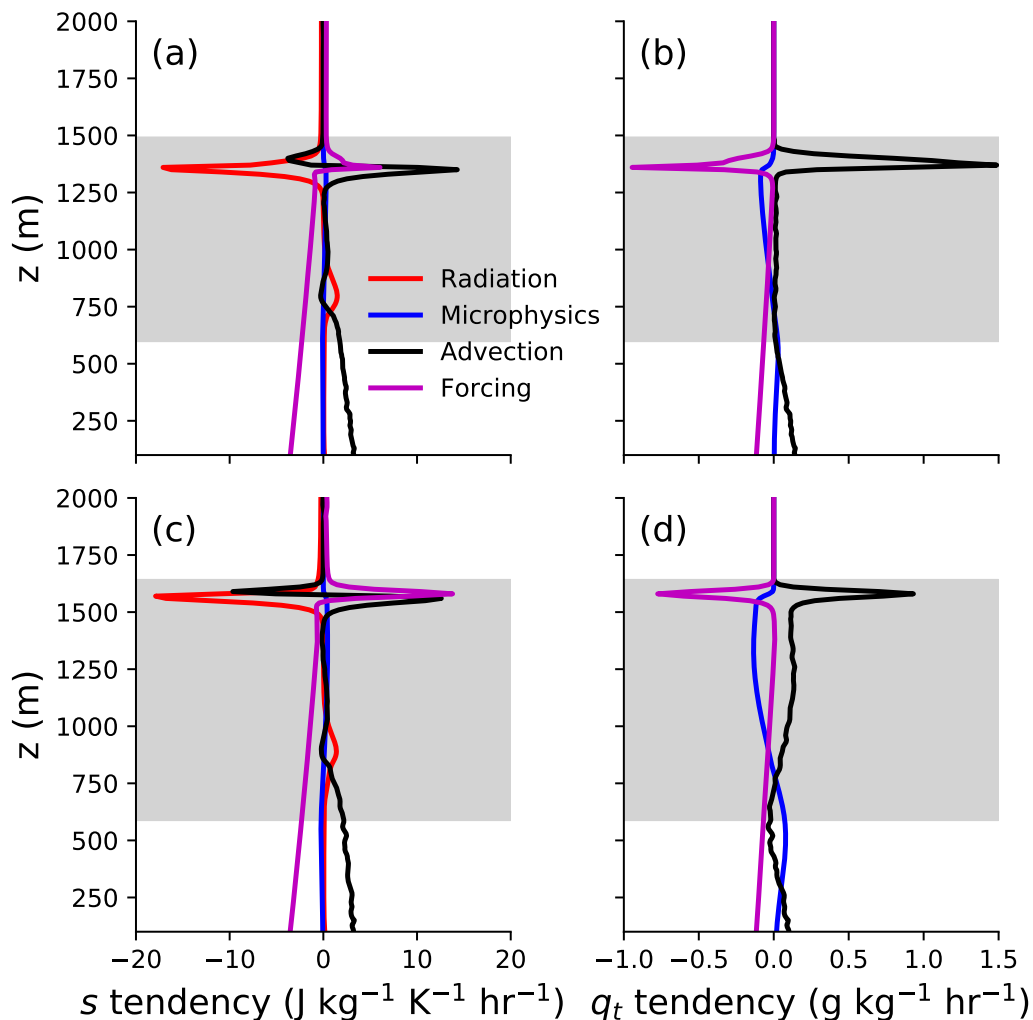


Figure 3.7: M-PACE domain mean profiles of time tendencies for (a, c) specific entropy ds/dt , and (b, d) total water specific humidity dq_t/dt . Averages are calculated for the first (top) and the 12th (bottom) simulated hours. Gray shading corresponds to the liquid layer.

Case	Observational Period (UTC)	LWP (g m^{-2})	IWP (g m^{-2})
SHEBA	May 7, 1998	8.0–40 (64)	0.25–2.0 (6.5)
M-PACE	Oct. 9-10, 2004	172–281 (235)	19.2–42.8 (51.9)
ISDAC	Apr. 26-27, 2008	3.7–24 (39)	3.1-11 (4)

Table 3.1: Observed LWP and IWP (both cloud ice and snow) from three Arctic boundary layer cloud model intercomparison case studies. The observational sources come from Morrison *et al.* [41], McFarquhar *et al.* [52], and Klein *et al.* [62]. Averaged values from PyCLES are shown in the brackets.

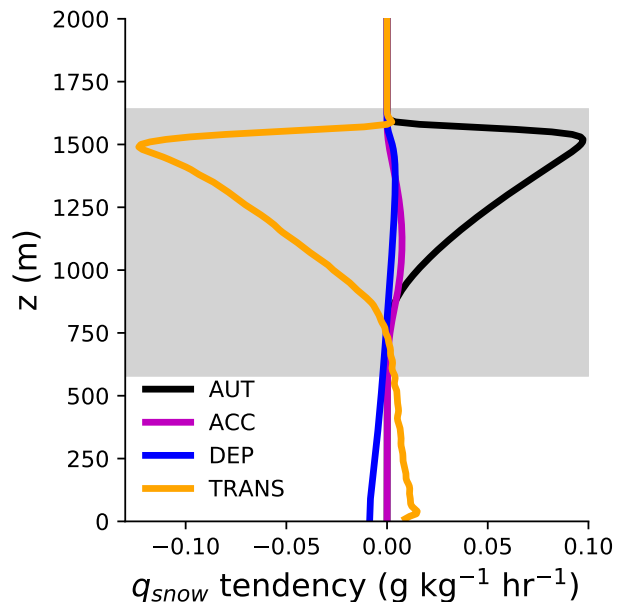


Figure 3.8: M-PACE domain mean profiles of time tendencies for snow water specific humidity $\partial q_{snow}/\partial t$. Different terms represent autoconversion (AUT), accretion (ACC), deposition/sublimation (DEP), and transport (TRANS) which includes both sedimentation and vertical flux. Averages are over the last 9 simulation hours. Gray shading corresponds to the liquid layer.

observed and simulated LWP and IWP in all three Arctic cases in Table 3.1. Even with a simple microphysics scheme, we were able to recover some general features of the microphysics in addition to the macrophysics. In particular, accretion of snow is more active in M-PACE than in SHEBA. The total ice number concentration in M-PACE is closer to observations than models with more complex microphysical schemes. Therefore, we feel confident in using PyCLES to capture the features of first-order importance in the polar BL.

Some challenges remain. In particular, the vertical structure of cloud ice differs from observations and intercomparison models. This is limited by the fact that our cloud ice is diagnosed to have the same vertical structure as liquid, and is not allowed to sediment. Furthermore, the collisional processes in our microphysics may not be active enough to form snow and decrease its residence time, which may contribute to the over-estimation of LWP in SHEBA/ISDAC, and IWP in SHEBA/M-PACE (Table 3.1).

*Chapter 4***IDEALIZED CLIMATE CHANGE OF POLAR CLOUDS UNDER
CONSISTENT LARGE-SCALE FORCING****4.1 Abstract**

The uncertainty in polar cloud feedbacks calls for process understanding of cloud response to climate warming. We adopted a novel modeling framework that uses GCM output of horizontal advection and surface fluxes to parameterize large-scale dynamics in a large eddy simulation (LES) model. We ran simulations with a seasonal cycle and sea ice, and varied longwave optical thickness to mimic climate change. Water vapor and cloud radiative feedbacks are not represented in the gray radiative transfer in both GCM and LES. The seasonal cycle of liquid clouds in the reference climate is consistent with observations, mainly with maximum low cloud fraction occurring during summer and autumn. In the warm climate, liquid low clouds decrease significantly during summer and autumn, while cloud top is elevated in all seasons. The decreased liquid cloud fraction is attributed to a drier and less statically stable lower troposphere, which is opposite to the instantaneous response of clouds to sea ice loss, as suggested by observational studies. Offline radiative transfer calculations suggest a net cloud radiative feedback of $0.6 \text{ W m}^{-2} \text{ K}^{-1}$, where longwave cloud radiative effect dominates over shortwave in the annual mean.

4.2 Introduction

As the Arctic warms and sea ice declines rapidly, it becomes more pressing to reduce the uncertainties associated with polar climate change. One of the most robust features of global climate projections is the polar amplified warming relative to the lower latitudes [7, 63]. As a consequence of higher air temperature, sea ice declines in coverage and volume. An ice-free summertime Arctic may be realized anytime between 2050 and well beyond 2100 [64], and models disagree on the timing of the ice-free Arctic under greenhouse gas forcing [65]. This uncertainty is not surprising, given that the projected Arctic surface temperature amplification ranges from 1.5 to 4.5 times the global mean warming [7].

One of the processes that contribute to Arctic climate change is the cloud radiative feedback. Clouds, depending on their amount, phases and altitudes, have different

radiative effects on the TOA and surface energy budgets. The polar regions differ from the lower latitudes in their limited incoming shortwave radiation and the frequent presence of ice droplets in addition to liquid in clouds. Although Arctic cloud feedback does not impose a first-order control on Arctic amplification, it is an important component influencing the magnitude of the amplification [27].

Early studies of Arctic cloud are often limited by the scarcity of observations. However, they have laid the groundwork for characterizing Arctic cloud and its seasonal cycle. For instance, Beesley & Moritz [66] was one of the earlier attempts to simulate the seasonal cycle of Arctic low clouds using a single-column model. In their study, lateral forcing provides a zeroth order control on the simulated cloud state. Forcing profiles based on reanalysis in summer and winter lead to a cloudy summer and a clear winter BL, which is consistent with the observed seasonal cycle of Arctic cloud. They also found that artificially shutting off surface evaporation in summer does not eliminate low cloud. Ice microphysics, as they pointed out, also play an active role in governing the cloudiness due to a shorter residence time of ice droplets compared to liquid ones. The authors suggest that in a warmer Arctic, the summertime cloudy season would be longer, hence increases low cloud amount with warming. However, given that the lateral forcing may also change as the climate warms, representing the changes in forcing may have a dominant effect on Arctic cloudiness.

Advances in satellite observations since the last decade have provided unprecedented 3D coverage of clouds in the polar regions. Figure 4.1 shows the observed seasonal cycle of vertical profiles of Arctic cloud fraction. Liquid-containing cloud fraction maximum occurs during late spring to early autumn in the boundary layer, while liquid clouds in the boundary layer persist throughout the year. Satellite observations are also used to study the variability in cloudiness. For example, Wall *et al.* [68] found increased cloud fraction over open water as a result of cold-air advection off of the sea ice in the Southern Ocean during winter. In the Arctic, Kay & Gettelman [69] also suggest higher cloud fraction over open water compared to over sea ice in autumn but not summer. A more careful study that restricts analysis to sea ice variations further indicates that liquid clouds respond to sea ice loss in all seasons except for summer [70]. As the Arctic moves toward an ice-free state, changes in optically thick low cloud may impact the rate of sea ice loss. It is ever more urgent to improve our understanding of the cloud response to high-latitude warming.

The sign of net cloud radiative feedback in the polar regions is highly uncertain

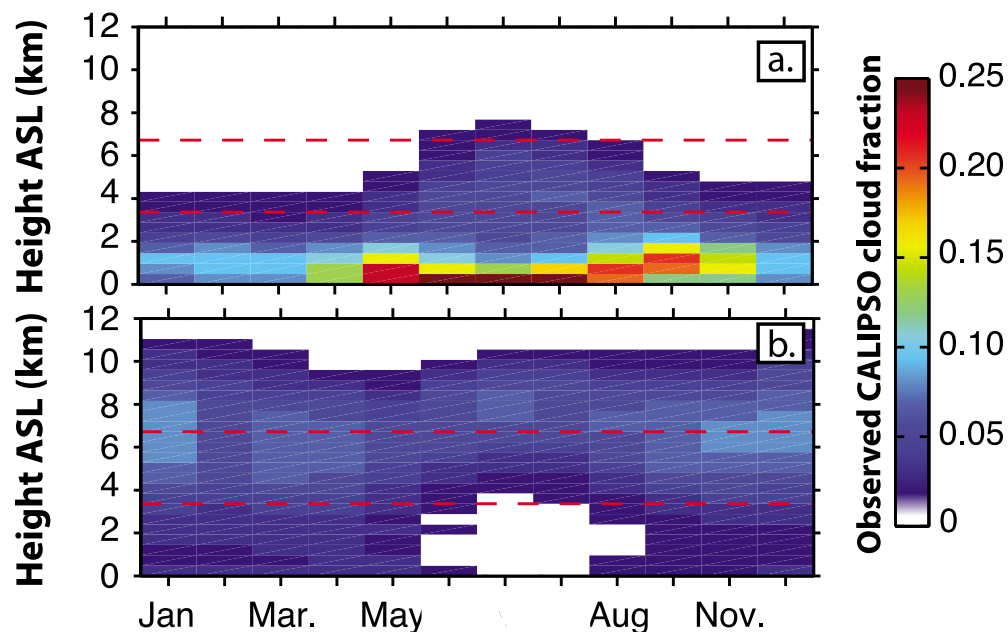


Figure 4.1: Seasonal cycle of monthly mean profiles averaged over the Arctic Ocean (70–82 N) during 2006–2011, showing (a) liquid-containing and (b) ice-dominated cloud fraction from satellite derived dataset CALIPSO-GOCCP. Red dashed lines define the low- and mid-level clouds. Modified from Figure 2 in Cesana *et al.* [67]. © American Geophysical Union.

in comprehensive GCM simulations [27]. In general, climate models agree on the sign of the LW cloud feedback being positive, and the SW cloud feedback being negative in the polar regions. However, the magnitudes of the LW and SW feedbacks vary dramatically across models, which leads to disagreement on the sign of the net cloud feedback. In Antarctica, nearly all GCMs produce a SW cloud feedback that is stronger than the LW cloud feedback, thus the total cloud feedback at 60°S is between 0 to $-2 \text{ W m}^{-2} \text{ K}^{-1}$. In the Arctic at 60°N, the total cloud feedback ranges between -1.6 to $1.0 \text{ W m}^{-2} \text{ K}^{-1}$ [71]. Given that the Arctic is expected to warm more than Antarctica overall [72], constraining the Arctic cloud feedback calls for priority.

Works motivated by paleoclimatic evidence of equable climates have proposed a positive convective cloud feedback at high-latitude regions [73–76]. The authors show through a series of model experiments that deep convective cloud over ice-free ocean during polar night presents a strong positive feedback, resulting a warm surface temperature and weak pole-to-equator temperature gradient. Under CO_2

quadrupling of pre-industrial concentration, Abbot *et al.* [75] also found the convective cloud feedback to be active, which contributes to winter sea ice loss, although other processes such as changes in oceanic heat transport are also indispensable.

Since most of the studies on polar cloud feedbacks use GCMs, and parameterizations in modern GCMs are often tuned to observations in the lower latitudes [77], the robustness of polar cloud projection becomes questionable. Therefore, we adopt a high-resolution modeling approach with a large eddy simulation (LES) model to explicitly resolve clouds and turbulence in the polar troposphere. The LES alone cannot support large-scale circulation due to its limited domain size, and we use the output from a GCM to provide large-scale forcing to drive the LES. The idea is similar to using GCM output or reanalysis to drive a single-column model, but without relying on cloud parameterizations. We also choose an idealized approach so that only the essential, first-order processes are included in the modeling framework. Examples of such processes include large-scale circulation, closed surface energy budgets, sea ice, and mixed-phase microphysics.

We would like to address the following questions: can we reproduce a reasonable seasonal cycle of Arctic cloud with our approach? Will the Arctic become cloudier or clearer as the climate warms? The following section describes the details of the modeling setup. Results are summarized in Section 3, followed by discussion and conclusion.

4.3 Model Setup

GCM

We use an idealized moist GCM to simulate large-scale dynamics of an Earth-like atmosphere [78–80]. Although the GCM is highly idealized, it has proven to be a useful tool to study many fundamental problems in the general circulation of the atmosphere. Some examples include the Hadley circulation, mid-latitude storm tracks, the hydrological cycle, the Walker circulation, monsoons, etc. [e.g., 80–84].

The lower boundary of the GCM is a mixed-layer ocean of 5 m thickness, and the surface energy budget is closed so that evaporation is constrained energetically by changes in external forcing. The GCM uses a gray radiation scheme with prescribed longwave optical thicknesses. The longwave optical thickness does not depend on water vapor, nor cloud water, thus water vapor and cloud feedbacks are not active in the GCM. The imposed changes in the longwave optical thickness represent changes in all longwave absorbers, including water vapor. Given that we are not focused

on any specific greenhouse gas, changing the longwave optical thickness directly is justifiable [80]. Shortwave radiation only varies with surface albedo. The default aquaplanet albedo is 0.38, but we changed it so that it depends on the presence of sea ice. Surface albedo is set to 0.3 for open water, and 0.5 for sea ice in this study. Clouds are not represented in the GCM. Any grid-scale supersaturation is removed immediately, and there is no reevaporation of the removed condensates. Surface roughness length is set to 5×10^{-3} m for momentum, and 1×10^{-3} m for scalars. All GCM simulations use T42 resolution.

One modification of the GCM specific to the current study is the saturation vapor pressure calculation. In order to obtain consistent thermodynamics, especially at cold temperatures, we implemented a look-up table in the GCM to get saturation vapor pressure and its temperature derivatives. The look-up table is obtained by integrating the Clausius-Clapeyron equation. At GCM runtime, the values are determined by linear interpolating the closest look-up table values. This treatment of saturation vapor pressure is consistent with the LES in this study [15].

We run the GCM with a seasonal cycle of 200 days, an obliquity of 23.5° , and zero eccentricity. The seasonal cycle is shortened to reduce the computational cost of LES simulations. Therefore, we refer four seasons as the 50-day averages (e.g., spring is the first 50 days, summer is day 50 to 100, etc.). In the reference climate, the longwave optical thickness at the equator and at the pole are $\tau_e = 7.2$ and $\tau_p = 1.8$. In the warm climate, τ_e and τ_p are set to 1.5 times the reference climate values. For experiments with a seasonal cycle, we run the GCM for 11 years, and use the last year to provide forcing for the LES. For equinox experiments, the GCM is run for 1000 days, and we take the last 25 days to provide the forcing. The default lower boundary condition of the GCM is a slab ocean without any prescribed oceanic heat flux. However, most of our study focuses on simulations with sea ice, which is described below. We also run seasonal cycle simulations without sea ice to compare the estimated cloud radiative effects. The equinox experiments are all run without sea ice, with a shallow 1 m slab ocean mixed-layer, and surface albedo of 0.38.

Sea Ice Model

A simple thermodynamic sea ice model is implemented in the GCM (Ian Eisenman, personal communication). It follows the Semtner [85] “zero-layer model”, with the following differences: 1) no surface snow layer; 2) the ice latent heat is kept constant; 3) ice surface temperature is calculated by assuming a steady-state surface

energy balance with the atmosphere, including the turbulent heat fluxes; and 4) ice frazil growth is included.

The sea ice model uses two prognostic variables: ice thickness h_{ice} and ice surface temperature T_{ice} . Figure 4.2 shows the schematic of the surface boundary condition without (left) and with (right) sea ice. At the base of the ice, temperature is assumed to be at the freezing point of water. First we compute the tendency of the ocean mixed-layer temperature,

$$\rho_w c_{pw} h_{ml} \frac{dT_{ml}}{dt} = F_Q - F_{base}, \quad (4.1)$$

where subscript w represents liquid water, ml stands for ocean mixed-layer, F_Q is the oceanic Q flux. F_{base} is the ice basal heat flux, approximated by

$$F_{base} = F_0(T_{ml} - T_f), \quad (4.2)$$

where where $T_f = 273.16$ K is the temperature at the sea ice base, taken to be the freezing temperature of water, and $F_0 = 120 \text{ W m}^{-2} \text{ K}^{-1}$ is the linear coefficient for heat flux from ocean to ice base. Next, we calculate the time tendency of the sea ice thickness

$$L_{ice} \frac{dh_{ice}}{dt} = -F_{atm} + F_{base}, \quad (4.3)$$

where $L_{ice} = 3.0 \times 10^8 \text{ J m}^{-3}$ is the latent heat of fusion. The flux exchange between surface and atmosphere F_{atm} includes radiation and turbulent heat fluxes,

$$F_{atm} = F_{rad} + F_{SH} + F_{LH}, \quad (4.4)$$

and we define F_{atm} to be positive when it contributes to atmospheric warming. If the updated T_{ml} at the current timestep is lower than the freezing temperature T_f , ice thickens by frazil growth at the bottom,

$$\delta h_{ice} = \frac{(T_{ml} - T_f) \rho_w c_{pw} h_{ml}}{L_{ice}}, \quad (4.5)$$

and T_{ml} is set to T_f .

At the sea ice surface, a steady-state is assumed for the surface energy balance:

$$F_{ice} - F_{atm} = 0. \quad (4.6)$$

A uniform heat flux in ice is given by

$$F_{ice} = k_i \frac{T_f - T_i}{h_{ice}}. \quad (4.7)$$

The time tendency of T_{ice} is then calculated implicitly based on surface energy balance.

When sea ice is not present, we have the default surface energy budget equation:

$$\rho_w c_{pw} h_{ml} \frac{dT_{ml}}{dt} = F_Q - F_{atm}, \quad (4.8)$$

where F_Q is the oceanic heat flux that is often prescribed in aquaplanet GCM with a slab ocean.

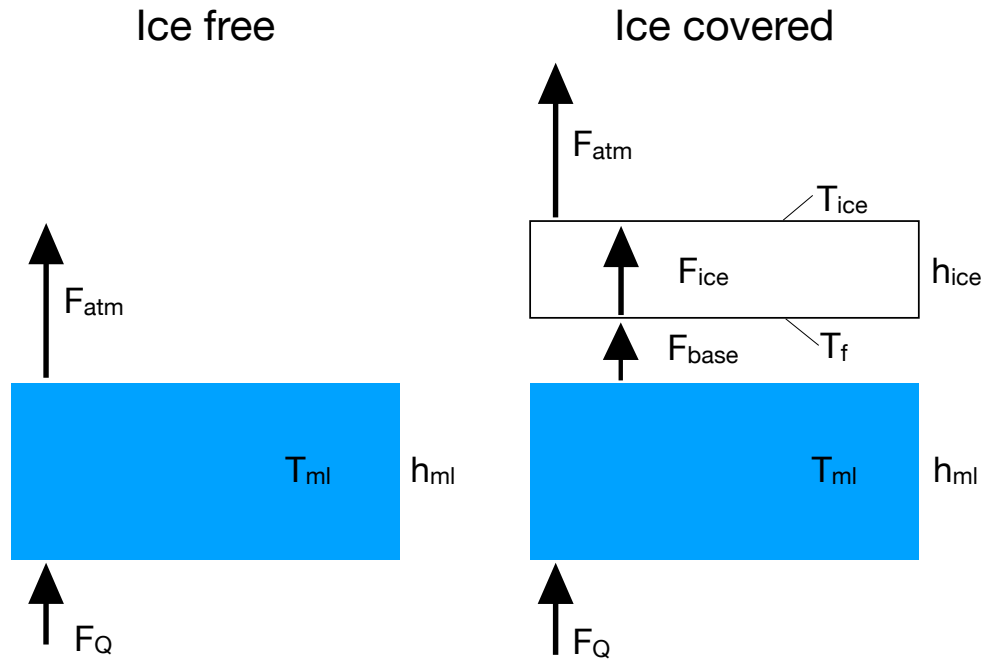


Figure 4.2: Schematics of the surface boundary conditions in the GCM.

Large-Scale forcing

In order to include large-scale dynamics, we use GCM output as forcing for the LES. These forcing fields are time tendency profiles applied at every LES timestep for each grid point, and are updated every 6 hours. The fields include both physical processes such as horizontal and vertical advection, and numerical effects such as spectral diffusion and conservation correction in the GCM. The addition of the numerical effects is to guarantee agreement in the LES mean states with the GCM.

The forcing fields are GCM zonal mean taken near 70°N . This has more relevance for the Arctic Ocean rather than the Southern Ocean, because poleward of 70°S the

presence of the Antarctic continent may influence the large-scale circulation, so that the circulation is quite different from that in an aquaplanet.

Because the GCM uses temperature as a prognostic variable, we will calculate the specific entropy tendencies for the LES, using temperature and specific humidity tendencies. The temperature tendency due to GCM large-scale (LS) forcing comprises the following terms:

$$\frac{\partial T^{LES}}{\partial t}_{LS} = \frac{\partial T^{GCM}}{\partial t}_{hadv} + w^{GCM} \frac{\partial T^{LES}}{\partial z} + \frac{\partial T^{GCM}}{\partial t}_{fino} + \frac{\partial T^{GCM}}{\partial t}_{SF} . \quad (4.9)$$

On the right-hand side, the first term represents the GCM temperature tendency due to horizontal advection. The second term represents the vertical advection, which uses an upwind advection scheme and takes the vertical gradient from the LES and the velocity from the GCM. This combined way to represent large-scale vertical advection allows the forcing to respond to simulated changes in the LES fields [86]. The third term represents the GCM temperature tendency due to pressure work, and the last term is the temperature tendency due to spectral filtering in the GCM. This term is not physical, but is included in the forcing because its instantaneous magnitude is comparable to other terms, and without it the LES may drift to a state that is significantly different from the GCM.

The specific humidity tendency is applied in a similar fashion:

$$\frac{\partial q_t^{LES}}{\partial t}_{LS} = \frac{\partial q_t^{GCM}}{\partial t}_{hadv} + w^{GCM} \frac{\partial q_t^{LES}}{\partial z} + \frac{\partial q_t^{GCM}}{\partial t}_{SF} . \quad (4.10)$$

The terms on the right-hand side are the q_t equivalent of equation (4.9), only without the pressure work term.

The specific entropy tendency due to GCM large-scale forcing depends on both temperature and specific humidity:

$$\frac{\partial s^{LES}}{\partial t}_{LS} = \frac{c_p}{T^{LES}} \frac{\partial T^{LES}}{\partial t}_{LS} + (s_v - s_d) \frac{\partial q_t^{LES}}{\partial t}_{LS} . \quad (4.11)$$

Note that s_v and s_d are the specific entropy of water vapor and dry air.

Equations (4.10) and (4.11) are applied to the prognostic equations as source terms in the LES.

Surface Forcing

In order to have consistent surface states, we apply surface forcing to the LES runs with a seasonal cycle. Surface temperature, sensible and latent heat fluxes are

prescribed in the LES with GCM values. When sea ice is present, the surface albedo is updated to be GCM sea ice value. All surface forcing fields are also updated every 6 hours.

One may ask whether prescribing sea surface temperature (SST) and surface fluxes in the LES lead to significant differences in the BL, given that the surface energy budget may no longer be closed in the LES. Because the SST is prescribed, a different atmospheric state in the LES will have a downward LW flux at the surface that is different from the GCM value. We tested the reference climate without sea ice with prescribed and closed surface energy budgets, and found only slight differences in simulated cloud liquid specific humidity. The vertical structure of cloud liquid is insensitive to whether surface forcing is prescribed.

LES

We work with the Python Cloud Large Eddy Simulation code (PyCLES) [15]. The model uses an anelastic framework, and ensures closed total water specific humidity and specific entropy budgets. PyCLES has been used successfully to simulate subtropical marine BL clouds [12, 13, 37], and also deep convective clouds (Kyle Pressel, personal communication).

The one-moment mixed-phase microphysical scheme follows Kaul *et al.* [38], and solves prognostic equations for snow and rain water specific humidity separately. Cloud condensates are diagnosed, and are part of the total water specific humidity q_t . Because the simulations are no longer limited to Arctic boundary layer clouds, I modified a few processes in the microphysical scheme ([38]) to be more general. The slope parameter of the particle slope distribution function (PSDF) for snow uses its default formulation in [39] instead of the empirical expression in Morrison *et al.* [41] (also see Appendix A in Kaul *et al.* [38]). Correspondingly, the intercept parameter of the snow PSDF follows the expression in Sekhon & Srivastava [87].

The LES uses the same gray radiation as the GCM. Because the LES reference pressure differ significantly from the GCM pressure, we use the GCM pressure and air density to calculate the radiative tendency in the LES.

4.4 Results

Reference Climate

Figure 4.3 shows the seasonal cycle of q_l profiles from the reference climate. The general pattern resembles that of the observed Arctic Ocean liquid cloud fraction

(Figure 4.1a). The maximum cloud liquid water is found in summer and early autumn, though a liquid layer with lower q_l persists in winter. These stratiform clouds extend to about 1 km above the surface. The highest liquid clouds are also found during summer and early autumn, whose top reaches 7.5 km. In winter, the top of liquid cloud is reduced to 2.5 km, and the maximum q_l value is a quarter of that in the summer. Spring is an interesting time for the liquid cloud, because the q_l maximum rises from below 1 km to 2 km in the first half of spring. In the late spring, intermittent low liquid cloud is accompanied by higher clouds that extend to 6 km.

Figure 4.4 shows the seasonally averaged (over 50 simulated days) domain mean profiles of q_l . The q_l peaks below 1 km in summer and autumn further indicate the presence of the stratiform layers. The seasonal cycle of the column integrated liquid water path (LWP) follows that of q_l (Figure 4.5). The maximum of 0.15 kg m^{-2} is found during late summer, and a minimum of nearly zero during winter.

Most of the clouds also contain ice phase, as seen in Figure 4.6. However, the low clouds are dominated by liquid. Ice clouds are mainly found in the upper troposphere above the liquid containing clouds. The q_i maximum is elevated through the year, from 7 km in spring to 10 km in winter. Although q_i maximum is about twice the q_l maximum, the ice water concentration ($q_i\rho$) maximum is lower than liquid water concentration maximum. There is minimal cloud ice water during spring to autumn in the mid to lower troposphere. The seasonal cycle of ice water path (IWP) is weaker than LWP. The maximum is found during late autumn to winter, while the minimum in early summer (Figure 4.5).

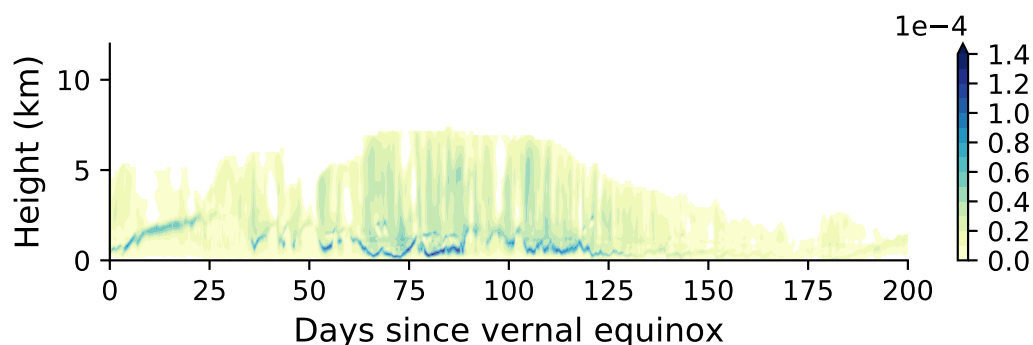


Figure 4.3: Seasonal cycle of domain mean liquid water specific humidity profile (kg kg^{-1}) in the reference climate.

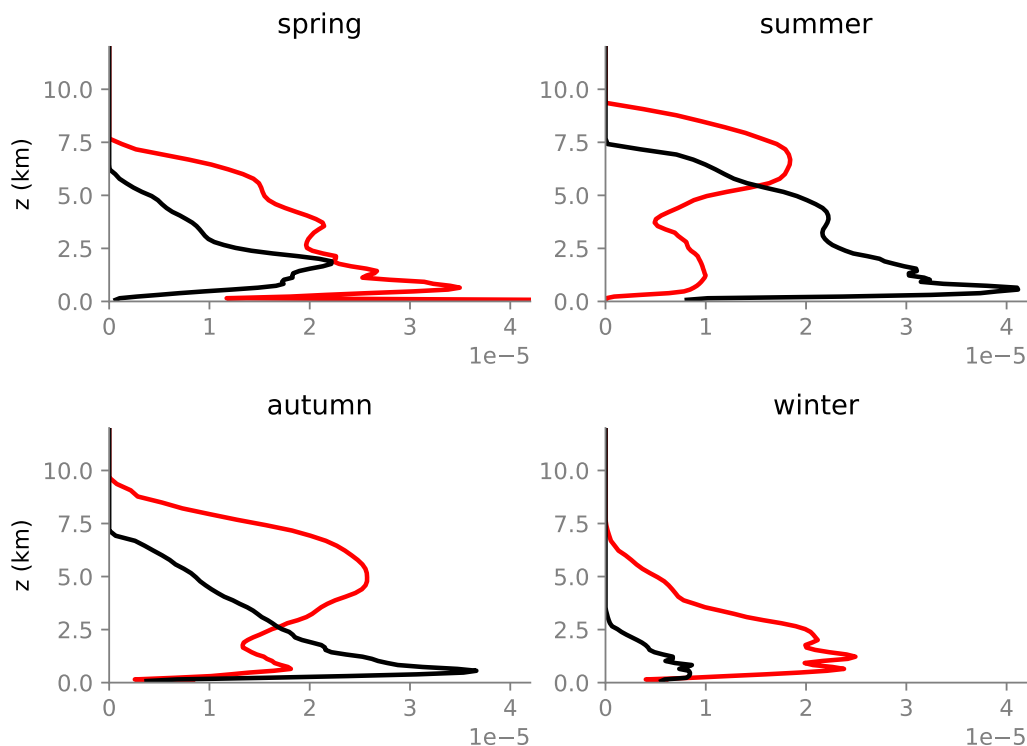


Figure 4.4: Seasonal (50-day averages) domain mean profiles of liquid water specific humidity (kg kg^{-1}) in reference climate (black) and warm climate (red).

In the reference climate, precipitation is dominated by snow (Figure 4.5). Most q_{snow} is found during late summer and early autumn, and the q_{snow} maximum is located at the base of the liquid stratiform layer, below 2 km (not shown). This is similar to simulations of Arctic BL clouds, described in the previous chapters. There is no snow above 5 km. This suggests that q_{snow} forms mostly from autoconversion of liquid water in mid to lower troposphere, instead of ice water in the upper troposphere.

Figure 4.7 shows the surface energy budget in the reference climate. During spring and summer, shortwave radiation dominates the surface energy budget. There is a net gain of energy at the surface, which is used to melt sea ice. In autumn and winter, the dominant balance involves longwave cooling and conductive heat flux through ice from the mixed-layer ocean. The turbulent heat fluxes are negligible, and the net surface flux is negative as sea ice grows. Sensible heat flux is generally negative (surface warmer than atmosphere), but becomes positive at the end of the melt season. This is when the surface temperature is kept at the freezing point during ice melt, but the atmosphere has already become warmer than the surface.

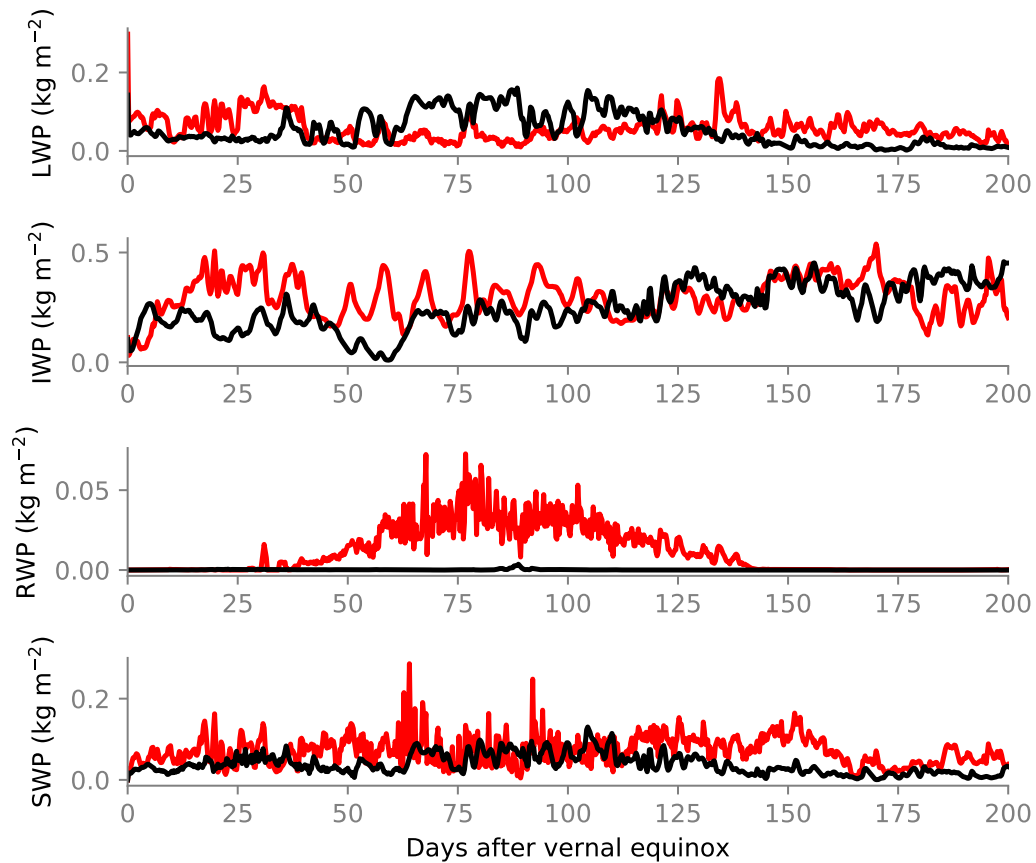


Figure 4.5: Seasonal cycle of liquid water path, ice water path, rain water path, and snow water path in kg m^{-2} . The reference climate is shown in black, and the warm climate (1.50x) is shown in red.

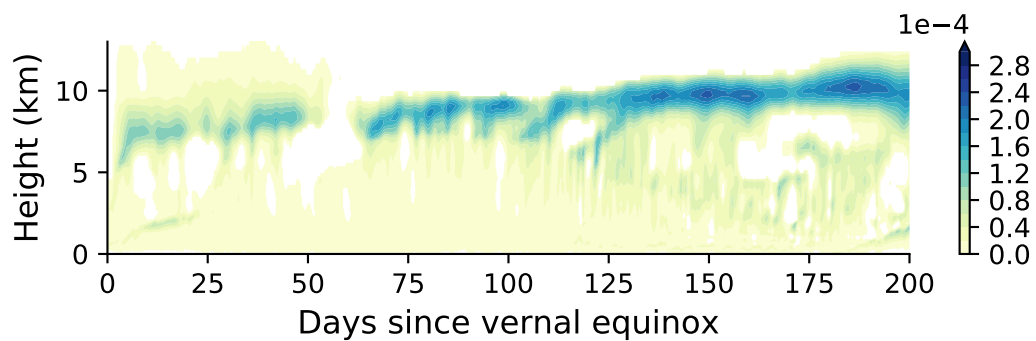


Figure 4.6: Seasonal cycle of domain mean ice water specific humidity profile (kg kg^{-1}) in the reference climate.

The presence of sea ice plays an active role in governing the surface temperature. Figure 4.8 shows the timeseries of surface temperature. In the reference climate,

the maximum surface temperature occurs in late summer, and is about 3 K above freezing. During late spring to mid-summer, surface temperature remains at the freezing temperature as sea ice melts from 1.4 m to zero at the end of summer (Figure 4.9). Surface temperature minimum occurs at the end of polar night at day 175 (mid-winter). The variation of surface temperature is about 30 K, less than the seasonal cycle observed during SHEBA campaign [88]. This may be due to the lack of a snow layer above the sea ice to provide extra insulation between the ocean and the atmosphere.

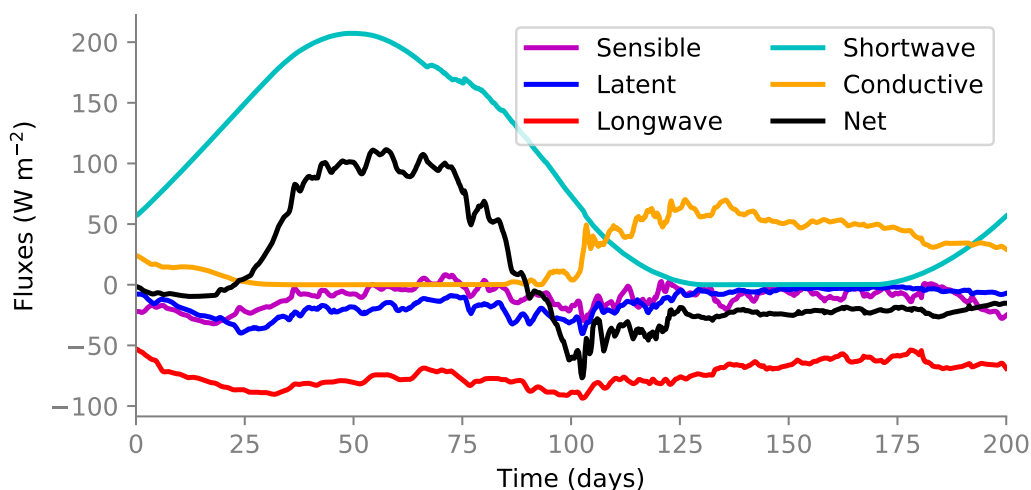


Figure 4.7: Time series of the surface energy budget of the reference climate. Time axis shows the days since vernal equinox. Positive values indicate a warming effect on the surface temperature.

Having looked at the thermodynamic fields in the LES, next we look at the turbulence structures. Figure 4.10 shows the vertical velocity variance, which is indicative of the depth of the buoyancy-driven turbulent layer in the domain. We can use these profiles to estimate the depth of the BL. The mean BL depth is around 2 km. In spring the BL is about 500 m higher, and the turbulence is the stronger than other seasons.

Response to Warming

When we increase the longwave optical thickness to be 1.5 times the reference climate values (i.e., $\tau_e = 10.8$, $\tau_p = 2.7$), atmospheric temperature increases in all seasons at all levels (Figure 4.11). However, the amount of warming varies with time and altitude. In all seasons except for spring, warming is strongest near the surface, consistent with GCM simulations of increased greenhouse gas concentration [e.g.,

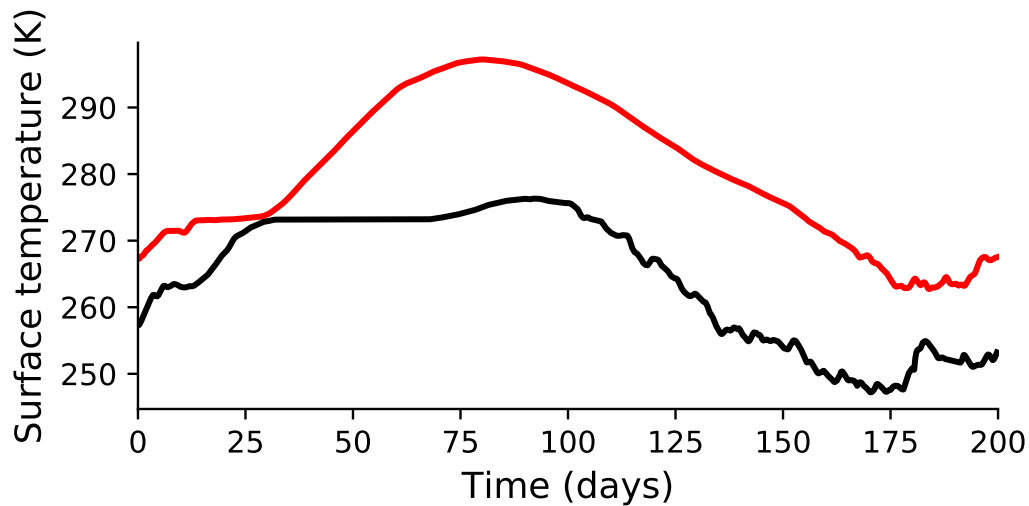


Figure 4.8: Time series of surface temperature (K) in reference climate (black) and warm climate (red). Time axis shows the days since vernal equinox.

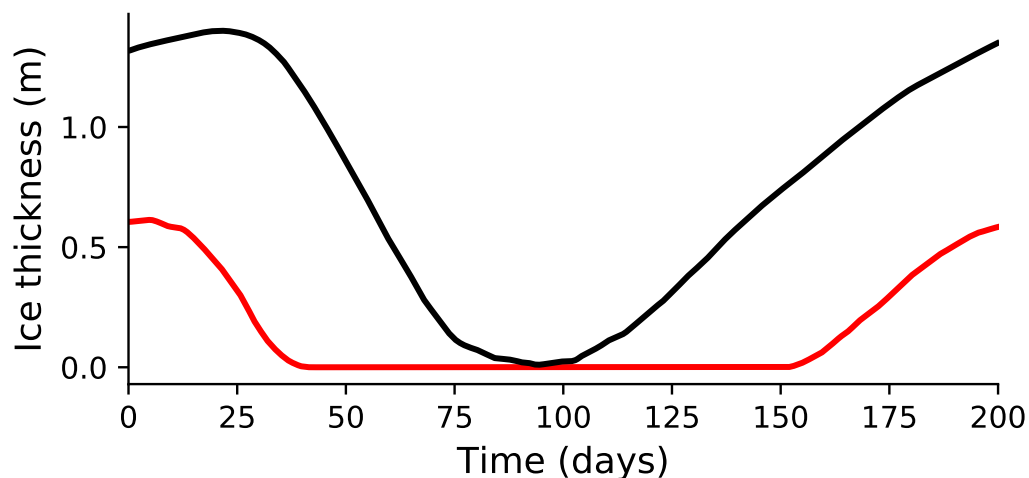


Figure 4.9: Time series of sea ice thickness (m) in reference climate (black) and warm climate (red). Time axis shows the days since vernal equinox.

6]. In autumn, the near-surface warming is greater than 20 K. There is also a secondary warming peak in mid to upper troposphere. Although the solar forcing is symmetric for spring and autumn, the lower troposphere is about 8 K warmer in spring in the reference climate. This asymmetry is flipped in the warm climate, where the autumn lower troposphere is about 10 K warmer than that in spring. This is associated with changes in the sea ice seasonal cycle.

Sea ice thickness shows significant decrease as the climate warms (Figure 4.9).

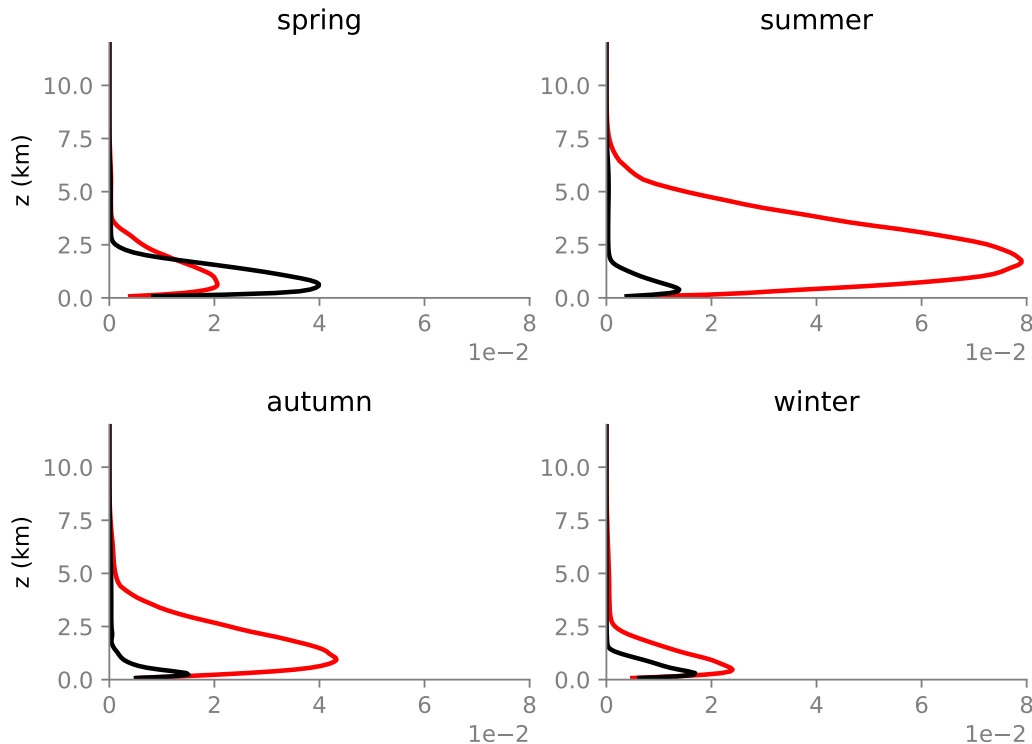


Figure 4.10: Seasonal (50-day averages) domain mean profiles of vertical velocity variance $\overline{w'w'}$ ($\text{m}^2 \text{s}^{-2}$) in reference climate (black) and warm climate (red).

The maximum ice thickness has reduced from 1.4 m to 0.6 m, less than half of its value in the reference climate. The ice melt onset is about 25 days earlier, and the melt season is significantly shortened from 50 days to 25 days. The growing season is delayed for about 50 days. In the warm climate, the domain remains ice-free during summer and autumn. As a consequence of reduced surface albedo, surface latent heat flux has increased significantly during the ice-free seasons (Figure 4.12). During summer, the latent heat flux is even more efficient in cooling the surface than the longwave flux.

Consequently, there are significant changes in the liquid cloud seasonal cycle as the climate warms (Figure 4.14). First of all, the stratiform liquid layer above the surface in summer and autumn is absent. Instead, lower q_l ($0.1\text{--}0.2 \text{ kg kg}^{-1}$) appears intermittently in the BL that is up to about 3 km deep from day 28 to 120. At the same time, a higher liquid cloud layer that extends to 7–9 km resides above the BL. In spring and winter, there is a significant increase of liquid water in the BL (see also Figure 4.4). The top of the liquid layer in spring and winter is also higher than in the reference climate. The spring liquid profiles in the warm climate are reminiscent

of the summer liquid profiles in the reference climate. The q_l profiles in a warmer climate all show significant upward shifts (Figure 4.4). In summer and autumn, the peak q_l occurs above 5 km instead of near the surface, and there is a secondary q_l peak that corresponds to the BL cloud. In both spring and winter, the q_l peaks are found around the same altitudes, but the values have nearly doubled.

The seasonal cycle of cloud ice under a warmer climate corresponds to an upward shift of q_i maximum of 2 to 3 km (Figure 4.15). The upward shift is also accompanied by an increase of q_i . Although precipitation is still dominated by snow, there is now significant amount of rain during the warmer half of the year (Figure 4.5). The q_{rain} layer coincides with the q_l layer in the lower troposphere during day 28 to 120 (Figure 4.14). Above this layer, snow is formed under the secondary q_l in mid-troposphere. Thus, the vertical structure of condensates in the troposphere during summer and autumn changes from (top-down) ice-liquid-snow in the reference climate to ice-liquid-snow-rain in the warm climate (not shown).

The changes in cloud characteristics are associated with stability changes in the warm climate. Figure 4.16 shows the static stability, defined as the vertical gradient of liquid-ice potential temperature $d\theta_{li}/dz$, for each season in the two climates. The most obvious change in the warm climate is the decreased static stability in all seasons at nearly all levels. Decreased static stability in the warm climate is consistent with enhanced convection and increased cloud top heights. As shown in Figure 4.10, vertical velocity variance has increased in all seasons except for spring. In spring, the BL is much more stable in the warm climate than the reference climate (Figure 4.16), which is consistent with decreased sensible heat flux at the surface during an earlier melt season (Figure 4.12).

Estimating Cloud Radiative Effects

Although the gray radiation does not allow cloud-radiation interactions in both GCM and LES, one can use an off-line radiative transfer model to estimate the radiative effects of the clouds in the LES. Here, we use the RRTMG radiative transfer model [43]. Domain mean profiles of temperature, specific humidity, pressure, density, and cloud condensates from 25-day averages (two per season) are used as input fields for RRTMG. Here, we define the longwave and shortwave cloud radiative effect (CRE)

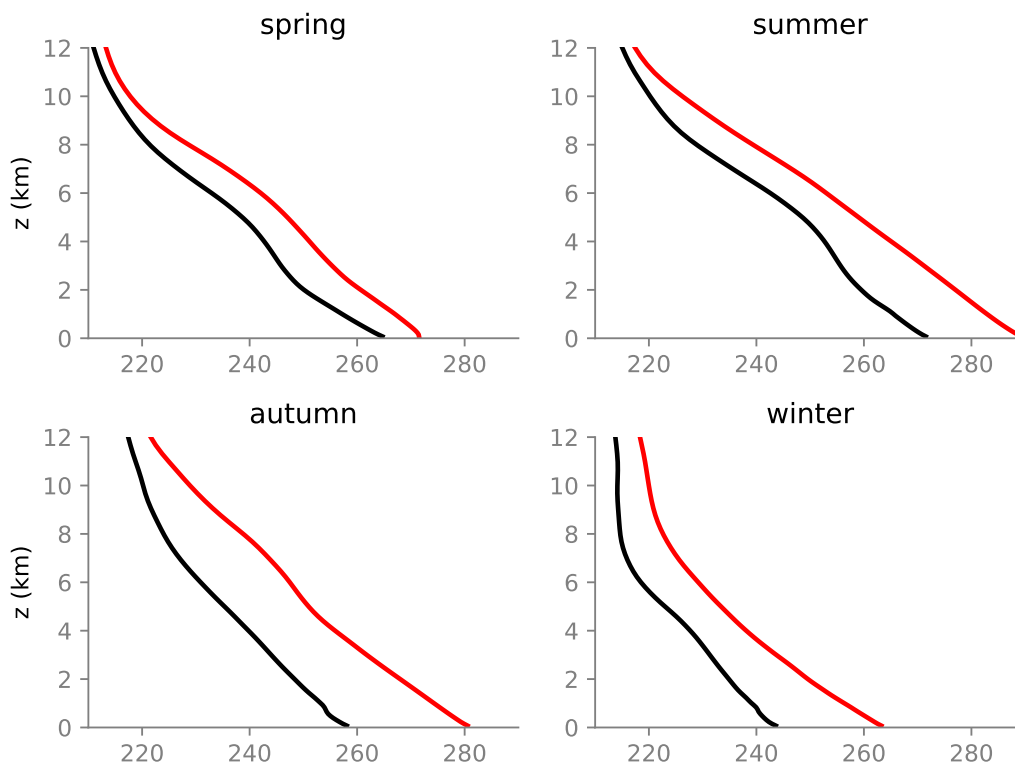


Figure 4.11: Seasonal (50-day averages) domain mean profiles of temperature (K) in reference climate (black) and warm climate (red).

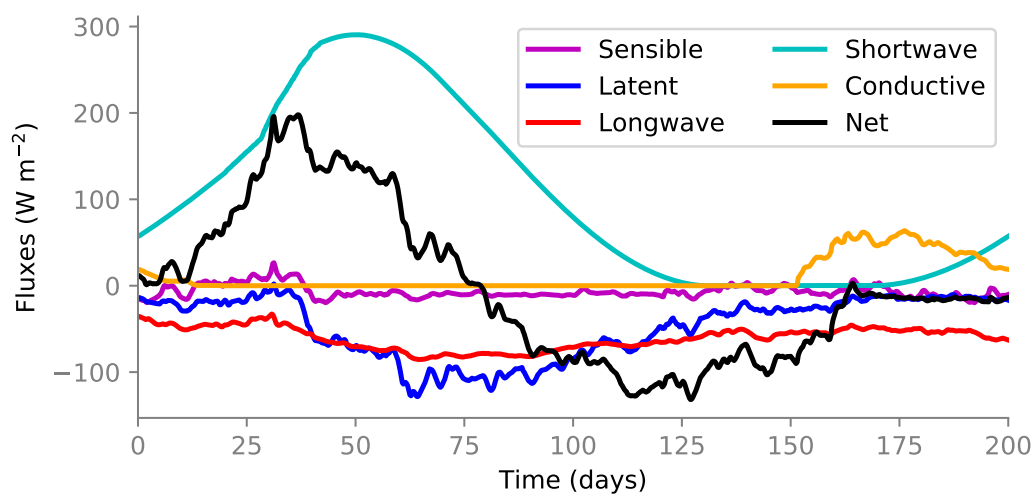


Figure 4.12: Surface energy budget of the warm climate. Positive values indicate a warming effect on the surface temperature.

as the difference between all-sky fluxes and clear-sky fluxes:

$$\text{LWCRE} = (\text{LW}_{all-sky}^{\downarrow} - \text{LW}_{all-sky}^{\uparrow}) - (\text{LW}_{clear}^{\downarrow} - \text{LW}_{clear}^{\uparrow}), \quad (4.12)$$

$$\text{SWCRE} = (\text{SW}_{all-sky}^{\downarrow} - \text{SW}_{all-sky}^{\uparrow}) - (\text{SW}_{clear}^{\downarrow} - \text{SW}_{clear}^{\uparrow}), \quad (4.13)$$

$$\text{CRE} = \text{LWCRE} + \text{SWCRE}. \quad (4.14)$$

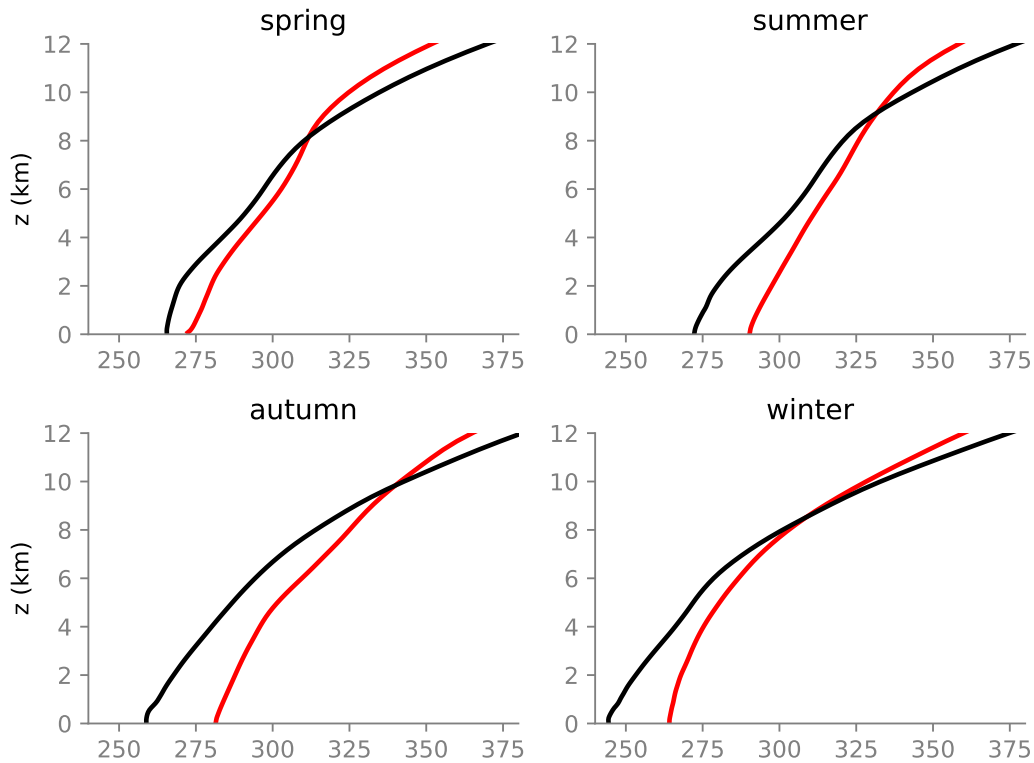


Figure 4.13: Seasonal (50-day averages) domain mean profiles of liquid-ice potential temperature θ_{li} (K) in reference climate (black) and warm climate (red).

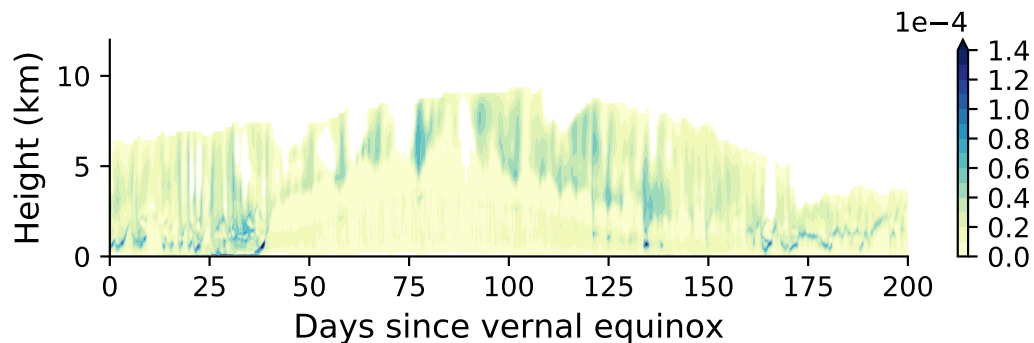


Figure 4.14: Seasonal cycle of domain mean liquid water specific humidity profile (kg kg^{-1}) in warm climate ($1.50\times$ longwave optical thickness).

In order to compare our estimated CRE with observations in Kay & L'Ecuyer [9], we shifted the seasonal cycle so that the start of the time series is equivalent to January.

Figure 4.17 shows the seasonal cycle of CRE in the reference climate. Annual mean CRE is positive at both TOA and surface, indicating that clouds have an overall

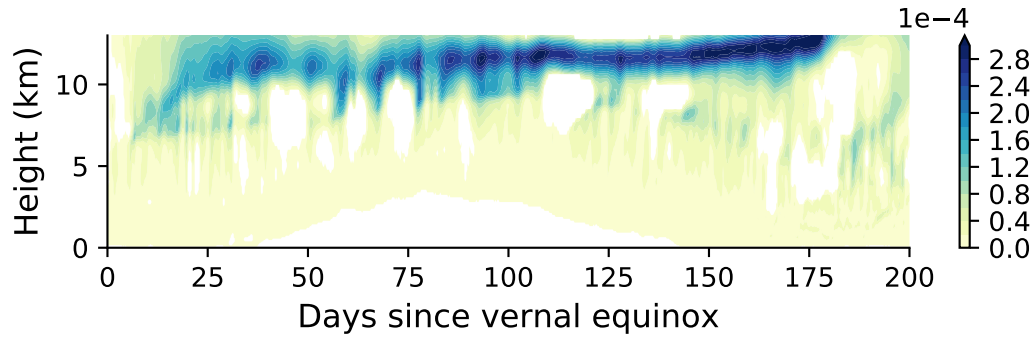


Figure 4.15: Seasonal cycle of domain mean ice water specific humidity profile (kg kg^{-1}) in warm climate ($1.50\times$ longwave optical thickness).

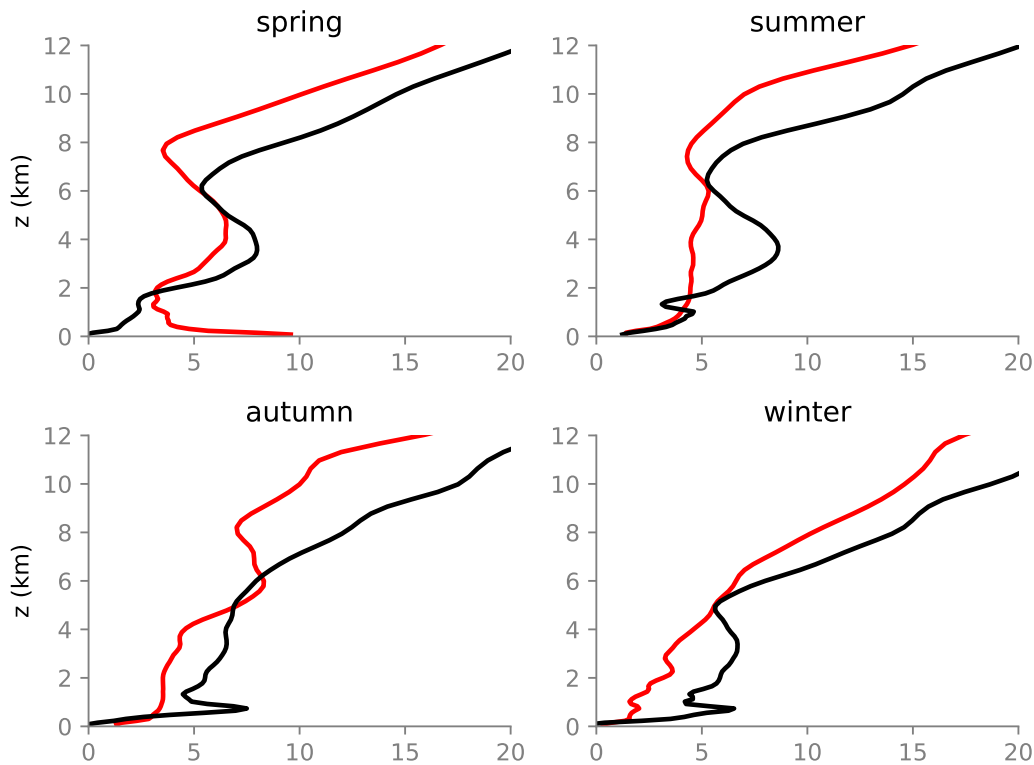


Figure 4.16: Seasonal (50-day averages) domain mean profiles of static stability ($d\theta_{li}/dz$, in K km^{-1}) in reference climate (black) and warm climate (red).

warming effect for both the atmosphere and the surface. The seasonal cycle of CRE is dominated by the pattern in SWCRE in the sense that clouds have a warming effect during polar night, and a cooling effect during summer. At TOA, there is a weak seasonal cycle of LWCRE, where the maximum occurs in summer and minimum in winter. This is consistent with the fact that low-level liquid cloud that is optically

thick is the most prevalent in summer. The SWCRE is strongest in the time of peak insolation, reaching -100 W m^{-2} . At surface, the LWCRE seasonal cycle is muted compared to TOA, while the SWCRE is weaker than at TOA. The net CRE at the surface is stronger than at TOA (20 versus 6 W m^{-2}), suggesting an effective role clouds play in warming the surface.

The same estimation can be done for the warm climate. Figure 4.18 shows the difference between the two climates. At TOA, the annual mean net CRE is 8 W m^{-2} higher in the warm climate than the reference climate. Given an increase of annual mean surface temperature of 14 K, the estimated total cloud radiative feedback parameter is $0.6 \text{ W m}^{-2} \text{ K}^{-1}$. This results from combining a positive longwave feedback of $1.3 \text{ W m}^{-2} \text{ K}^{-1}$ and a negative shortwave feedback of $-0.7 \text{ W m}^{-2} \text{ K}^{-1}$ at TOA. The strength of the cloud feedbacks varies with seasons, where the positive feedback is strongest in winter, and in summer the cloud feedback is negative because changes in SWCRE dominate.

At the surface, the sensitivity is nearly always negative in both LWCRE and SWCRE. This is somewhat surprising, given that in spring and winter, liquid water in low clouds shows an increase in the warm climate. The LWCRE during spring and winter shows a mild decrease, while during autumn a significant decrease in LWCRE is likely associated with reduced low-level cloud liquid. This suggests that the low-level liquid cloud is not the only factor controlling the surface LWCRE, but high cloud and ice cloud also play an important role. During the sunlit period, the shortwave effect becomes stronger so that less shortwave radiation reaches the surface as the climate warms. The difference in CRE at the surface indicates that as the climate warms, the surface warming effect of clouds becomes weaker.

In order to test the robustness of the estimated cloud feedbacks, we vary the longwave optical thickness over a wider range of climates. To shorten the simulations, we remove the seasonal cycle and sea ice in the GCM and LES. We set the insolation to be the equinox value, and allow the surface energy budget in the LES to be interactive instead of prescribed. The rest of the setup remains the same as the seasonal cycle runs. Then we use domain profiles averaged over 20 days of the LES simulations to calculate CRE in RRTMG. Figure 4.19 shows the estimated CRE as a function of SST. At TOA, the CRE changes is dominated by LWCRE. LWCRE increases almost linearly until 280 K ($\alpha = 2.0$), then decreases in the warmest case ($\alpha = 2.5$). SWCRE decreases with SST first, then remains quite constant with SST in the warmer climates. At surface, CRE is again dominated by LWCRE

response. The change in LWCRE is not monotonic, which increases with SST in colder climate, and decreases in warmer climate.

4.5 Discussion

Comparison with Observations

An encouraging result of our experiment is the resemblance of the simulated liquid clouds in the reference climate to observations. Although the model setup here is highly idealized, and many processes are absent, we can still compare the seasonal cycle of clouds and CRE with observations. For example, Cesana *et al.* [67] produced the seasonal cycle of cloud fraction averaged over the Arctic Ocean (70–82°N) based on space-borne lidar-retrieved product CALIPSO-GOCCP. The maximum liquid cloud occurrence is found near the surface from May to September, and the highest extent of liquid cloud reaches about 7.5 km in July. During winter, liquid cloud fraction is lower, but is still persistent below 2 km. Ice cloud fraction is lower than liquid overall, and is zero below 4 km during June to August. The ice cloud maximum occurs at 7 km in winter, while ice cloud reaches as high as 11 km. The observed occurrence of cloud vertical extent and maxima over the Arctic Ocean matches well with the simulated seasonal cycle of clouds in the reference climate (Figure 4.3). This provides some confidence in the physical relevance of our experiments, suggesting the large-scale and surface forcing's role in shaping the seasonal cycle of polar clouds. We also want to stress here that the comparison is a rough first-step toward constraining polar cloud modeling. For example, we cannot compare the cloud fraction directly with the observed cloud fraction, given that the scales and definitions are different in LES and satellite observations. A more sophisticated comparison should involve simulators that convert simulated thermodynamic fields to variables that are directly measured by satellites [27, 89].

We can also compare the integrated cloud condensates with satellite observations over the Arctic Ocean north of 60°N (Figure 2 in Lenaerts *et al.* [90]). The observed LWP ranges from 0.015 to 0.125 kg m⁻², with the maximum occurring during late summer and minimum during winter. Although the maximum LWP during summer in our reference climate is over-estimated (0.16 kg m⁻²), timing of the maximum and minimum is consistent with the observed LWP in polar oceans. Larger discrepancies are found in IWP. The observed IWP over the Arctic Ocean ranges from 0.01 to 0.11 kg m⁻². In the reference climate simulated by LES, IWP ranges from 0.01 to 0.46 kg m⁻², much higher than observed. The seasonal cycle is weak in both observations and our simulation, showing a slightly higher amplitude during winter.

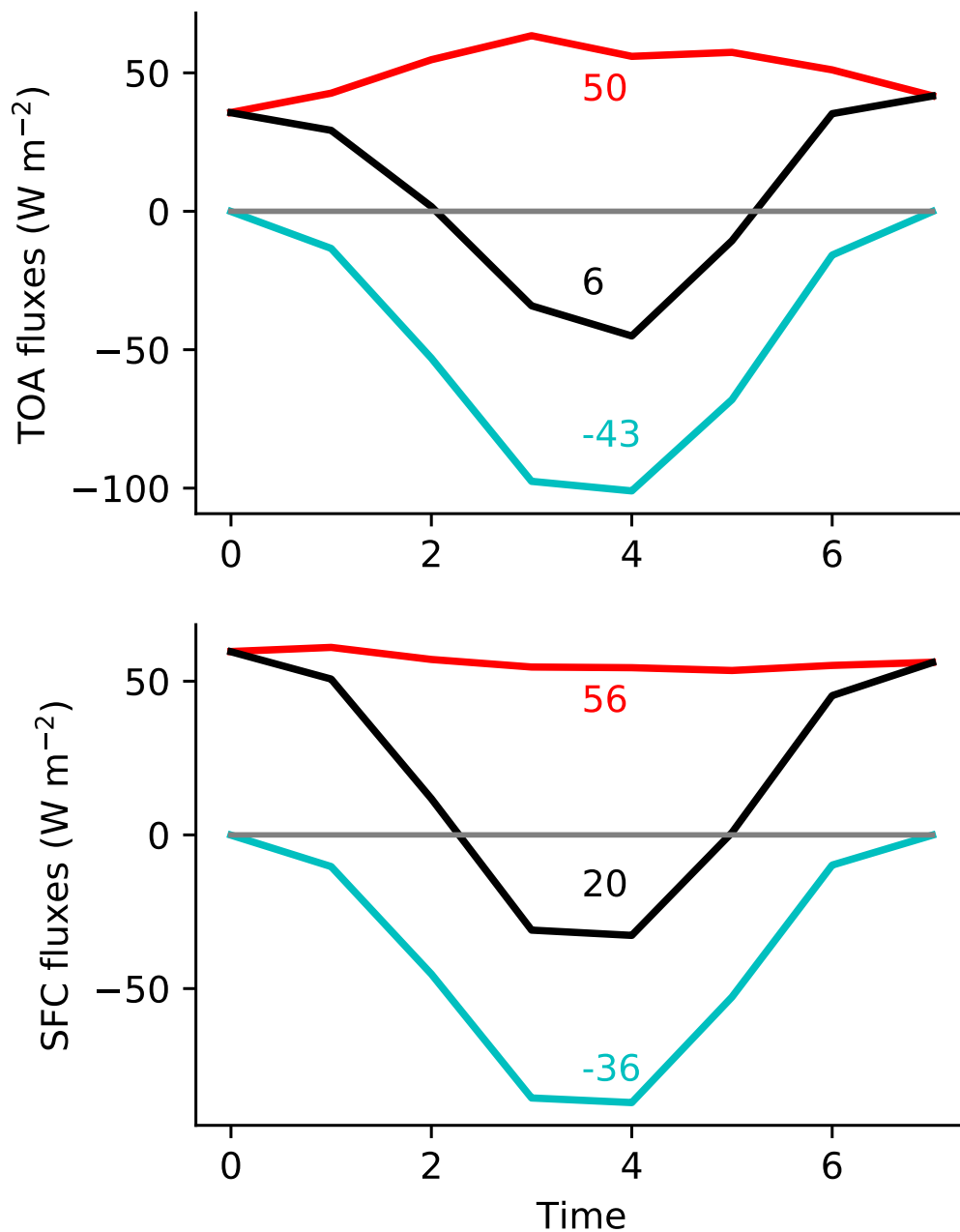


Figure 4.17: Seasonal cycle of cloud radiative effects at (top) top-of-atmosphere and (bottom) surface, estimated off-line with RRTMG and domain mean profiles in the reference climate. Each data point is calculated from a 25-day average. The time axis is shifted so that it is equivalent to a regular calendar year starting from January. Red shows LWCRE, cyan shows SWCRE, and the net CRE is in black. Numbers show the annual mean values of each category.

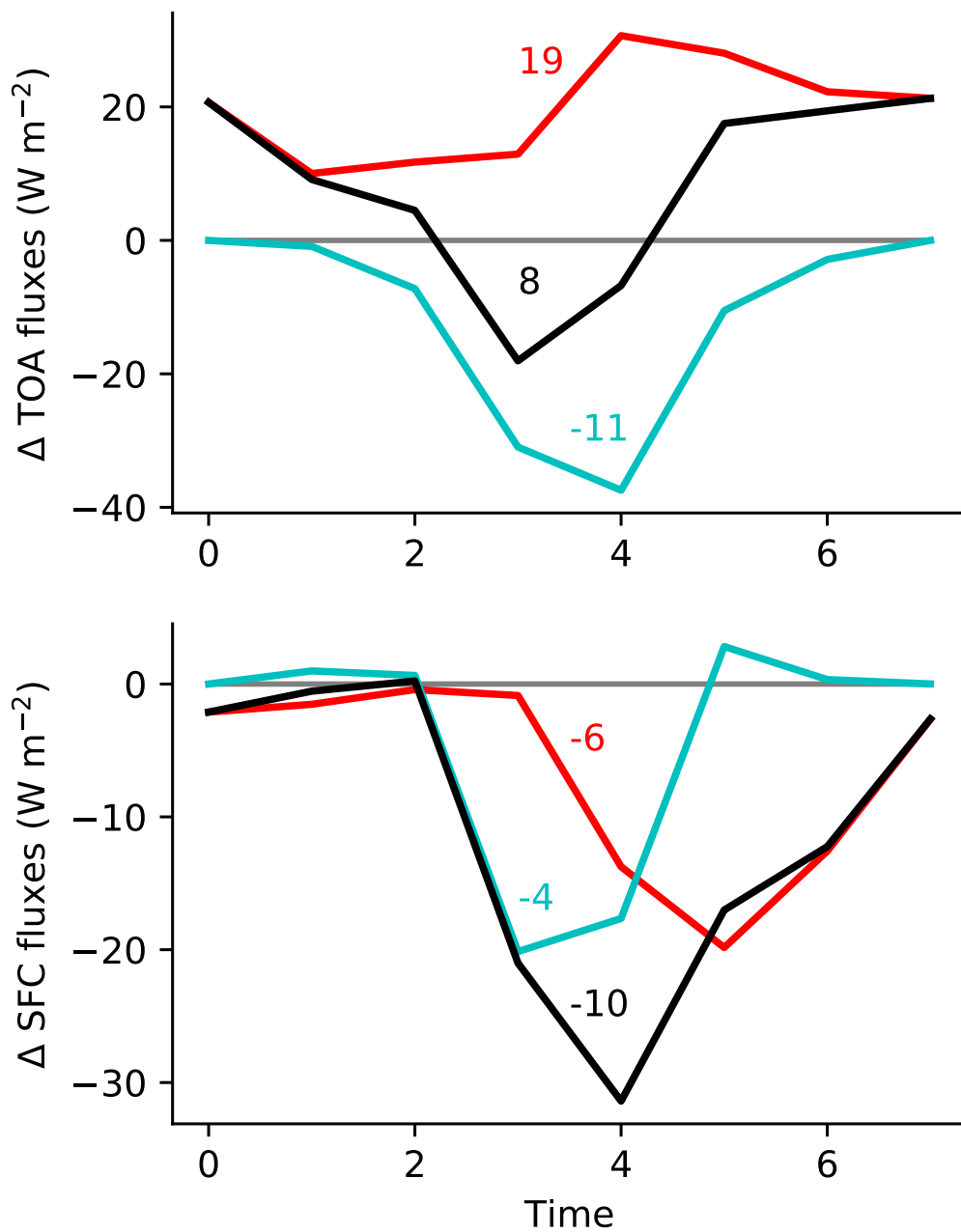


Figure 4.18: Same as Figure 4.17, but showing the difference between the warm and reference climate.

The cloud ice excess in the reference climate may be related to our simple treatment of ice microphysics and an inefficient removal of ice particles at high altitudes. Interestingly, CMIP5 models tend under-estimate IWP[90].

Being aware of the biases in our simulated cloud fields, we can then compare our

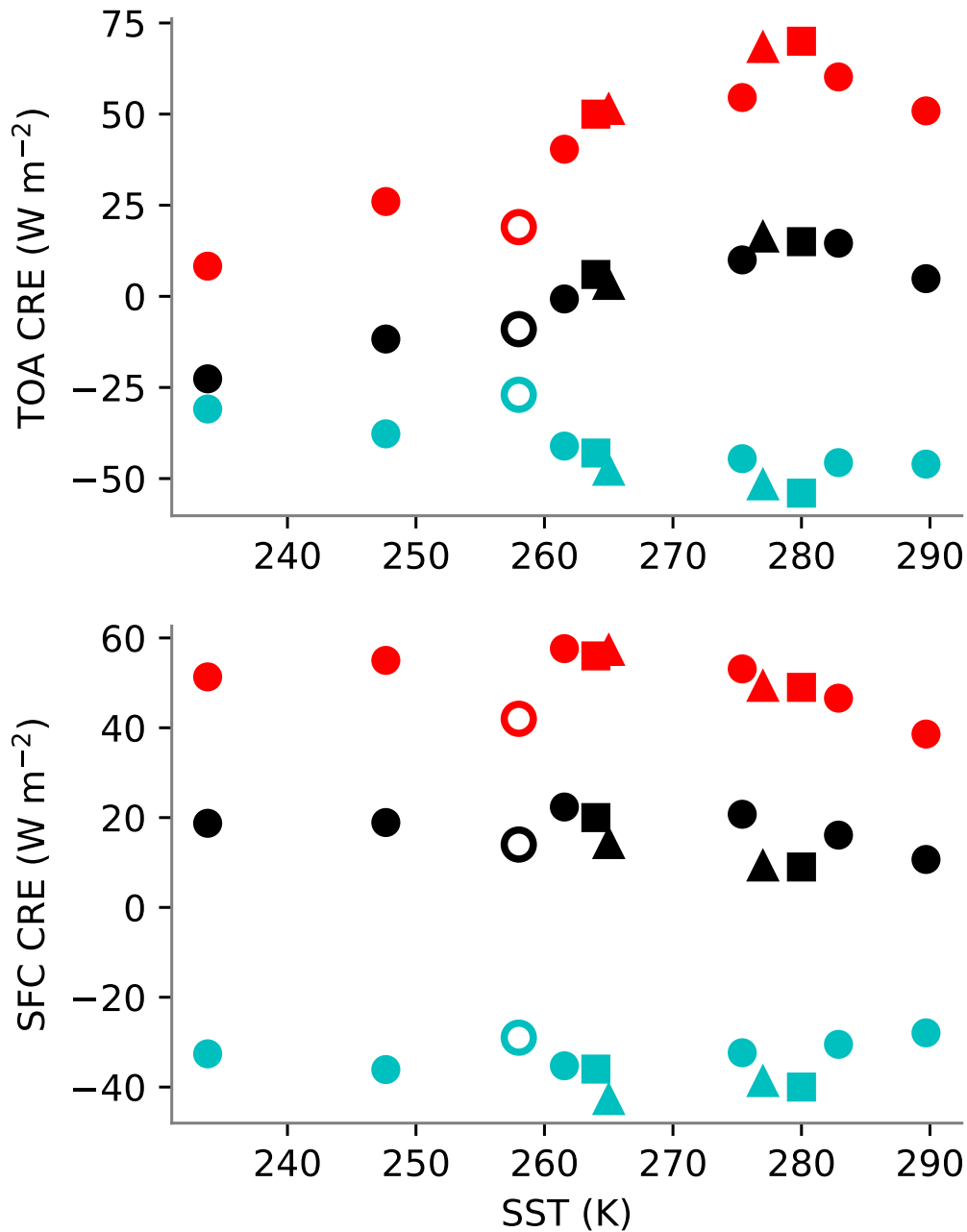


Figure 4.19: Annually mean TOA and surface CRE (black), LWCRE (red), and SWCRE (cyan) plotted against mean SST. Solid circles show equinox simulations with various longwave optical thicknesses from a factor of 0.4 to 2.5. Triangles show the reference and warm climates with seasonal cycle and sea ice. Squares show the reference and warm climates with seasonal cycle without sea ice. Open circles show the observed values averaged over the Arctic Ocean by Kay *et al.* [27].

estimated CRE to observations [9, 27] (Figure 4.19). The TOA CRE is too high in our estimation, with an annual mean of 6 W m^{-2} instead of the observed -9 W m^{-2} . Both the warming effect of LWCRE and cooling effect of SWCRE are over-estimated, but especially in longwave radiation. In observations, the net radiative effect of clouds is to cool the atmosphere instead of to warm as suggested by our LES simulations. At surface, the annual mean CRE agrees on the sign and is close in magnitude (20 W m^{-2} in LES vs 14 W m^{-2} in observations). No doubt that the LWCRE dominates the surface radiative forcing except for the summer months. The observed LWCRE seasonal cycle is weak at TOA and surface, and SWCRE is mainly controlled by insolation. To explain the discrepancies of in CRE is the natural next step for us to improve our understanding of polar cloud dynamics.

Case	Longwave	Shortwave	Net
Sea ice	1.3	-0.7	0.6
No ice	1.4	-0.3	1.1
Equinox	1.1	-0.3	0.8

Table 4.1: Estimated cloud feedback parameters in $\text{W m}^{-2} \text{ K}^{-1}$, using various LES simulations and off-line RRTMG calculations. For the equinox simulations, the warmest climate is excluded for feedback estimation, and all other cases follow a linear CRE relationship with SST (Figure 4.19).

Strengths of the Cloud Feedbacks

We can use the TOA CRE computed off-line and SST changes to infer the cloud feedback strength (Table 4.1). In all cases, the longwave cloud feedback dominates over shortwave, and the net cloud feedback is always positive no matter which set of simulations is used for the estimation. However, the magnitude of the feedback parameters vary with simulations. The largest difference between seasonal cycle simulations with and without sea ice is in the shortwave component. When sea ice is represented in the models, the strength of the shortwave feedback is about twice as large. In the real world, the shortwave radiative effect of clouds tend to be masked by the presence of sea ice. Given that there is no cloud-radiation interactions in the LES, the shortwave cloud feedback from sea ice simulations may be over-estimated. The equinox simulations include a much wider range of climates, but the longwave cloud feedback does not differ too much from the seasonal cycle without sea ice simulations.

In Abbot *et al.* [76], the authors increased the CO_2 concentration in a comprehensive AGCM to 16 times preindustrial level, and produced a similar range of climates as

our equinox simulations. Their estimated winter LW cloud feedback is $0.75 \text{ W m}^{-2} \text{ K}^{-1}$, which is lower than our estimates. When compared to the Arctic cloud feedbacks in CMIP5 models, our estimations are higher in LW cloud feedback (0.2 to $1.0 \text{ W m}^{-2} \text{ K}^{-1}$ in CMIP5) and weaker than most models in the SW cloud feedback (-2.0 to $0.5 \text{ W m}^{-2} \text{ K}^{-1}$ in CMIP5, only one model gives positive SW cloud feedback). Consequently, the net cloud feedback estimated here is at the high end of the CMIP5 range[71].

Surface vs Large-Scale Forcing

Naturally we would like to know what causes the decline of liquid low cloud as the climate warms. Is it the changes in local surface fluxes, or the large-scale forcing associated with a different climate? Although in the summer and autumn, surface heat fluxes especially latent heat flux have increased in the warm climate, relative humidity near the surface is 8% lower. BL is drier as it become more convective in the warm climate. This result is opposite from the local air-sea coupling hypothesis [69, 70], where it is suggested that a stronger air-sea coupling over open water leads to higher liquid cloud amount. Here, the large-scale circulation also changes so that the horizontal advection of temperature is weaker in the warm climate. The low cloud undergoes regime transition from stratiform in the reference climate to cumulus in the warm climate. The BL becomes drier (lower relative humidity) in the warm climate during summer and autumn, consistent with a decrease of low cloud amount during these seasons. The drying is consistent with more rigorous convection and strengthened vertical gradient of specific humidity in the lower troposphere, similar to the response to subtropical low cloud's response in modern GCMs [77, 91].

Preliminary entropy budget analysis suggests that in summer, changes due to radiative cooling destabilize the lower troposphere, and so does increased vertical mixing. Changes due to microphysics and prescribed large-scale forcing have a stabilizing effect on the lower troposphere. In autumn, changes due to large-scale forcing also destabilizes the lower troposphere. More detailed analysis on the moisture budget is needed to better understand cloud changes in a warmer climate.

One should also keep in mind that the climate change forcing here is a strong one, equivalent to abruptly quadrupling CO_2 . This is stronger than the usual GCM climate change forcing (e.g., RCP8.5). We also focus on the equilibrium response instead of the transient response that is more relevant for the air-sea coupling hypothesis.

However, we should still aim to better quantify the roles surface fluxes and large-scale forcing play in governing polar cloud amount.

Limitations and Future Work

The GCM used in the study has a positive relative humidity bias in the polar regions. In the free troposphere, the climatological relative humidity is between 65 to 70% at 70°N. In the idealized GCM, the relative humidity is at least 10% higher. This can lead to a moist bias in the LES, given that our precipitation is not particularly efficient in removing moisture in the free troposphere.

Our use of the simple microphysics scheme may be insufficient in reproducing the observed cloud seasonal cycle, especially in the ice phase. IWP in our simulation is about 4 times the observed IWP maximum. However, given that liquid droplets are more efficient in scattering and absorbing radiation, the over-estimation of ice may not have a first-order effect on TOA CRE. In fact, net CRE calculated without cloud ice differ only in the coldest climate due to total glaciation of cloud (not shown). LWCRE is lower without cloud ice, but the LW cloud feedback is very close to the full calculations.

Although we see a decrease in summer and autumn liquid low clouds with warming, we were not able to quantitatively separate the effects sea ice and large-scale circulation have on the cloud changes. A future experiment would be to exchange the surface forcing and large-scale forcing fields in the two climate. For example, we can run the warm climate with the surface forcing from the reference climate. If increased surface fluxes lead to more low cloud, as it is suggested by the local air-sea coupling hypothesis [70], we would expect decreased low cloud amount. Careful analysis of the heat and moisture budgets is also needed to quantify the role of surface versus large-scale forcings. Furthermore, adding cloud-radiation interactions in both the GCM and LES will allow more realistic calculation of the cloud feedback strength.

4.6 Conclusions

In order to study the response of polar clouds to climate change, we adopted a novel modeling framework that uses GCM output of large-scale advection and surface fluxes variables to drive a LES model. The approach encapsulates components of first-order importance in the polar regions, such as horizontal advection of heat and moisture from lower latitudes, sea ice, and a simple representation of mixed-phase microphysics. We run two climates with seasonal cycle and sea ice by varying the

longwave optical thickness, and compare the changes in cloud properties.

The seasonal cycle of liquid clouds in the reference climate is consistent with observations, mainly with maximum low cloud fraction found during summer and autumn below 2 km. In the warm climate, liquid clouds decrease significantly during summer and autumn, and cloud top is elevated in all seasons. The decreased liquid cloud amount is related to a drier and less statically stable lower troposphere. This is opposite to the instantaneous response of clouds to sea ice loss, as suggested by observational studies [69, 70].

Offline radiative transfer calculations suggest a positive net cloud radiative feedback of $0.6 \text{ W m}^{-2} \text{ K}^{-1}$ from our simulations with sea ice. In particular, longwave cloud radiative effect dominates over shortwave in the annual mean. In the warm climate, the seasonal changes in CRE reinforce the reference climate's CRE annual cycle. Future work includes adding the cloud-radiation interactions. Moreover, detailed budget analysis of entropy and moisture are needed to quantify the contribution from sea ice, local turbulence, and microphysics to cloud changes.

*Chapter 5***CIRCULATION AND MELTWATER DISTRIBUTION IN THE BELLINGSHAUSEN SEA: FROM SHELF BREAK TO COAST**

Zhang, X., Thompson, A. F., Flexas, M. M., Roquet, F. & Bornemann, H. Circulation and meltwater distribution in the Bellingshausen Sea: From shelf break to coast. *Geophysical Research Letters*, 43: 6402-6409. DOI: 10.1002/2016GL068998 (2016).

5.1 Abstract

West Antarctic ice shelves have thinned dramatically over recent decades. Oceanographic measurements that explore connections between offshore warming and transport across a continental shelf with variable bathymetry towards ice shelves are needed to constrain future changes in melt rates. Six years of seal-acquired observations provide extensive hydrographic coverage in the Bellingshausen Sea, where ship-based measurements are scarce. Warm but modified Circumpolar Deep Water floods the shelf and establishes a cyclonic circulation within the Belgica Trough with flow extending towards the coast along the eastern boundaries and returning to the shelf break along western boundaries. These boundary currents are the primary water mass pathways that carry heat towards the coast and advect ice shelf meltwater offshore. The modified Circumpolar Deep Water and meltwater mixtures shoal and thin as they approach the continental slope before flowing westward at the shelf break, suggesting the presence of the Antarctic Slope Current. Constraining meltwater pathways is a key step in monitoring the stability of the West Antarctic Ice Sheet.

5.2 Introduction

The Southern Ocean has experienced substantial changes since the last century, including warming throughout the water column [92] and freshening of bottom water [93–95]. Close to the Antarctic coast, remote observations have shown that basal melt has become the leading process for ice shelf thinning [96] and mass loss [97] in Antarctica. Significant glacier thinning was observed as a consequence of the ice shelf loss [98]. However, the link between ocean warming and accelerated ice shelf basal melt is less clear, mainly due to the lack of observations at high latitudes

and the complicated, bathymetrically-influenced continental shelf circulation.

Various studies have addressed the oceanic forcing on ice shelf basal melt. In the central Amundsen Sea, persistent flow of warm Circumpolar Deep Water (CDW) has been observed on the continental shelf [99–101]. There is strong evidence that shelf water here includes a modified CDW-meltwater mixture [102, 103]. Measurements in the vicinity of ice shelves allow estimations of basal melt rates, such as the Pine Island Ice Shelf [103–105]. There are also detailed studies of the Wilkins Ice Shelf and George VI Ice Shelf in the Bellingshausen Sea (BS) [106, 107]. In the western BS, hydrographic data are limited, although these measurements indicate that warm CDW found over the continental slope in this region is both warming and shoaling over the past two decades [108].

Warm CDW may enter the Bellingshausen Sea (BS) through the Belgica Trough (BT) and the Latady Trough to access the ice shelf cavities (Figure 5.1). Many ice shelves occupy the coast of the BS, all of which show positive basal melt rate [97] and volume loss in the last two decades [109]. The ice shelves east of 80°W have been relatively well-studied and monitored [106, 107, 110]. Less is known about the circulation and melting of the two ice shelves west of 80°W. For example, although the Venable Ice Shelf covers a smaller area, its basal melt rate is higher than that of the more extensive Wilkins Ice Shelf [97]. Numerical simulations have shown high concentration of melt water in the BT from BS ice shelves [111], and a weak cyclonic circulation on the continental shelf [112]. Here, hydrographic data are used to understand both the water modification processes on the shelf and the circulation in the BT.

At the shelf break, the frontal separation of offshore warm, salty CDW and colder, fresher shelf waters is related to the westward circulation of the Antarctic Slope Current (ASC) [113]. The ASC is not apparent along the western side of the Antarctic Peninsula, where the southern boundary of the ACC may flow unimpeded onto the continental shelf. Yet, the ASC is frequently seen in the Amundsen Sea suggesting the ASC's initiation is found somewhere in the BS. Observations of the exact location of the ASC's formation and its subsequent along-stream development are limited.

Although there has been a significant augmentation of oceanic observations in the BS by Argo floats, these hydrographic profiles are mostly north of the continental shelf break, and are limited by the extent of seasonal sea ice. On the continental shelf and especially in the BT, hydrographic data remain limited. Animal-borne

observations have become more prevalent in the last decade, mainly in high latitude regions by instrumented seals. These seals travel great distances in open water and under sea ice as they dive to between 500 and 2000 m depth. Water properties are sampled during the nearly vertical ascent phase of seal dives [114]. Calibrated data collected by the conductivity-temperature-depth satellite relay data loggers (CTD-SRDLs) efficiently contribute to an improved state estimate of the Southern Ocean circulation [115]. While the seal data presented here have irregular spatial and temporal sampling, they are the best available observations that cover, from the shelf break to the coast, a significant part of the BS continental shelf region. They also potentially provide a relatively long time series to examine evolving shelf break properties that shed light on the variability of the ASC in this region. In section 5.3 we describe the hydrographic data; results are presented in section 5.4. In section 5.5 we discuss how offshore properties as well as the continental shelf circulation and bathymetry influence the distribution of the ice shelf meltwater.

5.3 Data

We analyze data from the Marine Mammals Exploring the Oceans Pole to Pole (MEOP-CTD) database [115] (see <http://www.meop.net/>). These data are collected by southern elephant seals (*Mirounga leonina*) and crabeater seals (*Lobodon carcinophaga*) instrumented with CTD-SRDLs at several sites west of the Antarctic Peninsula. The data set provides extensive coverage in the BS region both temporally and spatially (Figure 5.1). The seals are able to dive beneath sea ice and transmit data in open leads when the coastal ocean is almost inaccessible to ships.

All data are subject to temperature and salinity calibration. Following the MEOP standard, calibration was conducted based on historical data in nearby regions [118]. The calibrated data have estimated uncertainties of $\pm 0.02^\circ\text{C}$ for temperature and ± 0.02 psu for salinity.

There are a total of 19,893 seal dives used in the BS region in this study. The data span the years 2007 to 2010 [119, 120], and austral summer of 2013-2014 (Supporting Information Table S1). More than 85% of the data were collected in austral autumn and winter (Figure S1). The data density is the highest on the continental shelf north of the Wilkins Ice Shelf. The coastal and shelf break regions also tend to have higher than average data density (Figure 5.1). While north of the VIS and the Abbot Ice Shelf have the sparsest data coverage on the continental shelf, this data set represents the most comprehensive survey of near-shore water mass

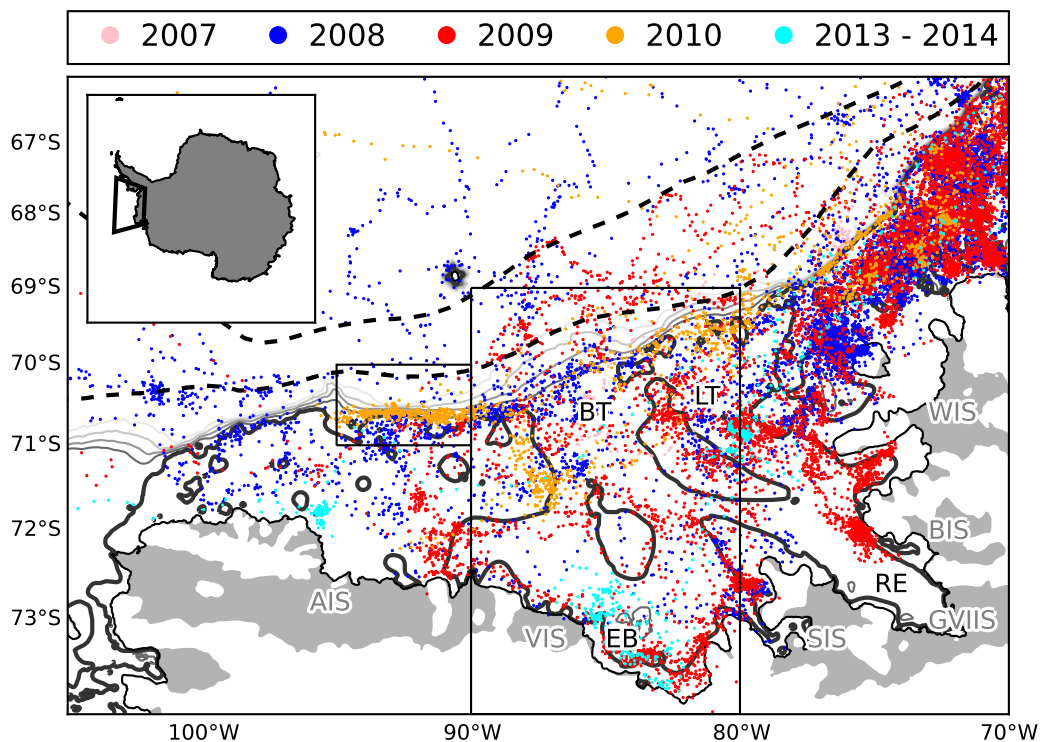


Figure 5.1: Map of western and central Bellingshausen Sea. Dots show the locations of all MEOP-CTD profiles used in this study. Colors indicate the different years. Contours show 0, 500 (thickened), 1000, 1500, 2000, 2500 m isobaths from IBCSO bathymetry [116]. Gray shadings indicate the ice shelves in the region: Abbot Ice Shelf (AIS), Venable Ice Shelf (VIS), Stange Ice Shelf (SIS), George VI Ice Shelf (GVIIS), Bach Ice Shelf (BIS), and Wilkins Ice Shelf (WIS). Other features include: Belgica Trough (BT), Latady Trough (LT), Eltanin Bay (EB), and Ronne Entrance (RE). Dashed lines are the Southern ACC front and the Southern Boundary defined by Orsi *et al.* [117]. The black boxes shows the regions on Figure 5.2 and 5.3. The insert shows the location of the studied region in Antarctica.

properties in this region of the BS.

5.4 Results

The full data set will be used to explore water mass pathways over the continental shelf. First, though, we begin by considering subsets of the data, as hydrographic sections, that show water mass characteristics at the continental shelf break and at the major troughs.

Typical cross-shelf and cross-slope hydrographic sections in the western BS, collected in austral winter 2010, show a surface mixed layer of near-freezing temperature extending to a depth that varies between 100 and 150 m (Figure 5.2).

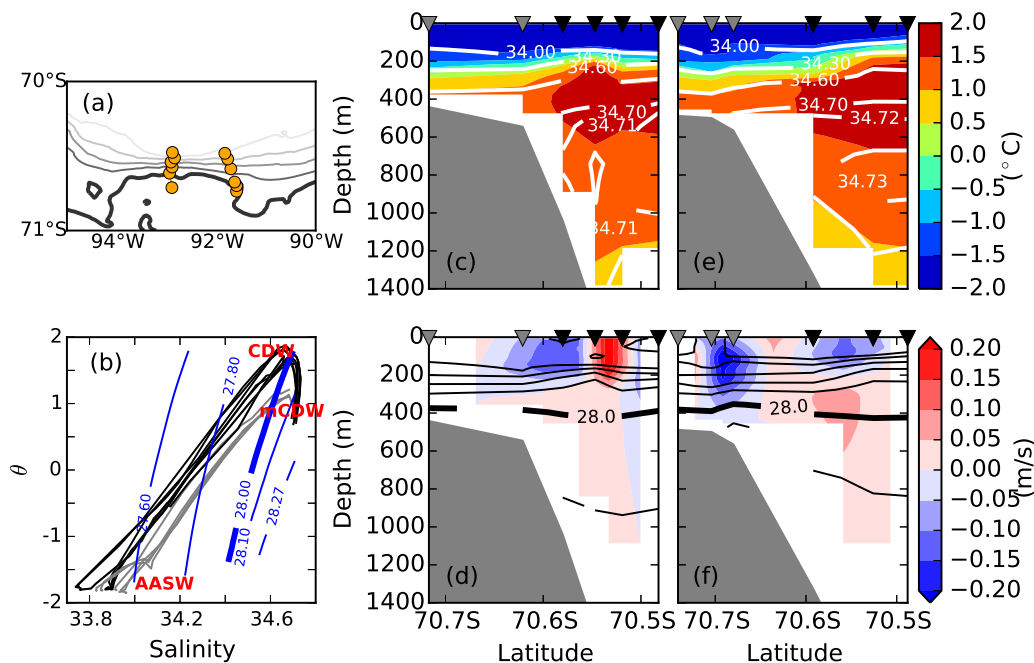


Figure 5.2: Depth-latitude cross-shelf/slope sections at the shelf break. (a) Map of the boxed region on Figure 5.1. (b) θ - S diagram of the sections' profiles, with on shelf ones in grey and offshore in black. The blue lines show select neutral density surfaces. Water masses are labeled in red. See the text for details. (c) Temperature ($^{\circ}\text{C}$, colors) and salinity (contours) for the section near 93°W in August 2010. (d) Geostrophic velocity (m s^{-1} , colors) referenced to the lowest data level and neutral density (kg m^{-3} , contours) for the section near 93°W in August 2010. The contour interval is 0.1 kg m^{-3} . Positive velocity indicates eastward flow. (e) and (f) are the same as (c) and (d), but for the section near 92°W in June 2010. Triangles indicate the latitude of the profiles.

This mixed layer is comprised of the coldest Antarctic Surface Water (AASW, $\gamma^n < 28.00 \text{ kg m}^{-3}$), which extends to a depth of approximately 400 m, consistent with [121]. The warmest and saltiest water mass, Circumpolar Deep Water (CDW, $28.00 < \gamma^n < 28.27 \text{ kg m}^{-3}$), lies offshore between 400 m and 800 m. Offshore, the θ_{max} associated with Upper CDW is $\sim 2^{\circ}\text{C}$ and the S_{max} associated with Lower CDW is $\sim 34.73 \text{ psu}$. This distribution agrees with the climatological position of the Southern Boundary of ACC [117], found just offshore of the continental shelf break. Our dataset does not contain AABW ($\gamma^n > 28.27 \text{ kg m}^{-3}$, $\theta > -1.85^{\circ}\text{C}$).

The neutral density surfaces in Figure 5.2 reflect a vertically-sheared geostrophic flow along the shelf break under the assumption of thermal wind balance. It is not possible to determine a reference velocity directly from the seal data, but we

choose to reference to the bottom since there is no evidence of a dense water outflow over the shelf that would give rise to strong bottom currents. There may still be a barotropic component of the flow that is not resolved. Assuming no motion at the bottom, the shear gives rise to a westward flow near the surface at the shelf break with weaker velocities at depth and a weak eastward current further offshore.

Over the continental shelf, the θ_{max} and S_{max} of the CDW are reduced. This modified CDW (mCDW) is both colder and fresher than the CDW found offshore (Figure 5.2b). Yet temperatures as warm as 1°C extend onshore, past the shelf break, and spread over the continental shelf. To investigate the on-shelf distribution of mCDW, we consider five synoptic hydrographic sections (e.g., nearly consecutive seal dives) that cross the BT, starting near the shelf break and moving towards the coast (Figure 5.3). Although these sections are from different time periods, some general trends are common below the thermocline.

Water warmer than 1°C is always present at depth. Cross-trough (East-West) gradients of θ and S are observed in every section, although the gradient weakens closer to the coast. Additional modifications are found in the along-trough direction. The temperature of the θ_{max} , warmest at the continental shelf break ($\theta \sim 1.4^\circ\text{C}$), is found at ~ 400 m, with its salinity maximum at ~ 700 m. Moving closer to the coast, the θ_{max} is confined to the eastern side of the BT (Figure 5.3a-d). At the western side of the BT, the mid-depth temperature maximum is eroded. The east-west difference in water mass characteristics suggests a cyclonic boundary current system within the trough with mCDW entering at the shelf break. This mCDW is modified slightly by mixing along the trough, but most of the modification occurs close to the coast. This can be seen in sections (e) and (f), which show a complete erosion of the mid-depth θ_{max} (Figure 5.3f). We also see a modification in salinity along the eastern boundary of the trough, however, given the instrumental uncertainty of 0.02 psu, the signal is marginal.

The contribution of ice shelf meltwater on mCDW is analyzed using the Gade line, defined as [102, 104, 122]

$$\theta(S) = \theta_{ocean} + L_f(1 - S_{ocean}/S)/C_p, \quad (5.1)$$

where $L_f = 334 \text{ kJ kg}^{-1}$ is the latent heat of fusion, $C_p = 3.97 \text{ kJ kg}^{-1} \text{ K}^{-1}$ is specific heat of sea water, and $\theta_{ocean} = 1.2 \pm 0.1^\circ\text{C}$, $S_{ocean} = 34.7$ psu are used as the characteristic θ and S for mCDW on shelf. By definition, θ - S values that lie along the Gade line obtain their characteristics from a mixture of ice shelf water

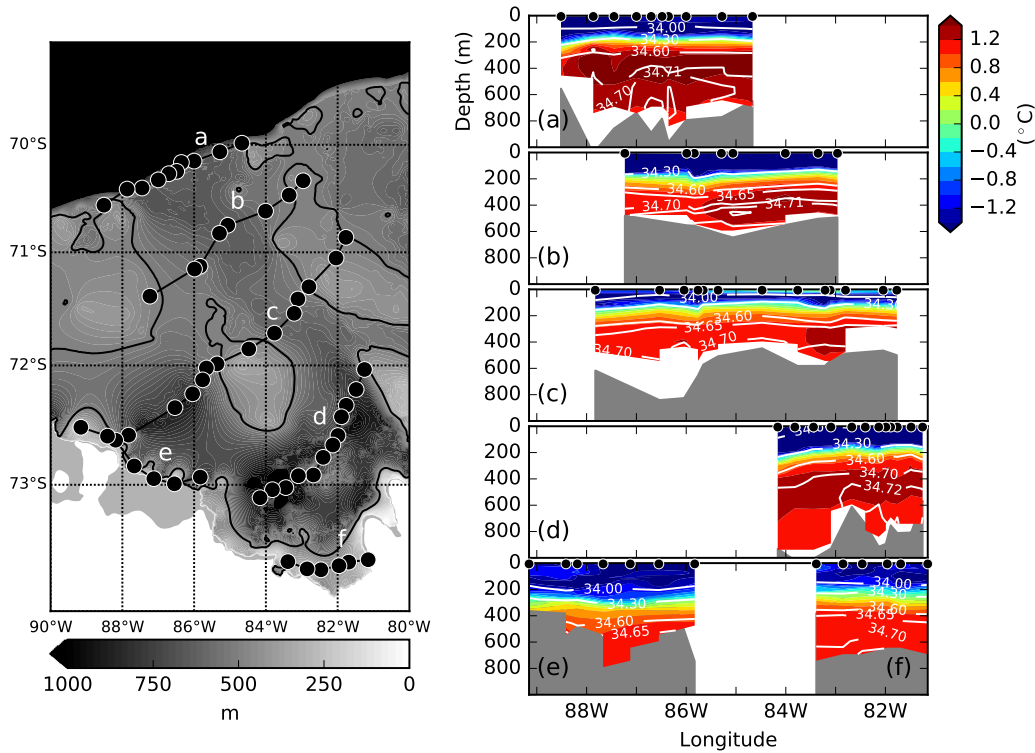


Figure 5.3: (Left) Depth of the Belgica Trough (m) and position of synoptic seal sections. The background shading of the map only shows bathymetry shallower than 1000 m, with the 500 m bathymetry highlighted in black line. Black circles indicate profile locations. (Right) Potential temperature ($^{\circ}\text{C}$, colors) and salinity (contours) sections in the Belgica Trough. Sections (a)–(f) were taken in 04/2010, 12/2013, 02/2008, 12/2013, 03/2008, and 03/2009, respectively.

and mCDW, which we refer to as the meltwater mixture. Shallow casts are removed from this analysis. To allow some variations of the water properties, we define a Gade envelope to determine whether a profile contains meltwater mixture.

Two criteria are defined to determine whether an individual profile “falls within the Gade envelope”: 1) In the depth range between $\theta = 0.9^{\circ}\text{C}$ and θ_{max} , the slope in θ - S space must be equal to $3.5 \pm 0.1^{\circ}\text{C} (\text{psu})^{-1}$. This θ range is chosen so that the analysis focuses on water properties at the base of the thermocline, which are comparable to the draft of nearby ice shelves. The Gade line is approximately linear in this temperature range. Additionally, the slope is independent of the MCDW properties, or the choice of θ_{ocean} and S_{ocean} in equation (5.1). 2) At the depth where $S = 34.65$ psu, we require $1.05 < \theta < 1.15^{\circ}\text{C}$. This allows for some θ - S variation of the mCDW. Both conditions (1) and (2) need to be satisfied. Broadening the Gade envelope allows more dives to meet the meltwater criteria; however, our

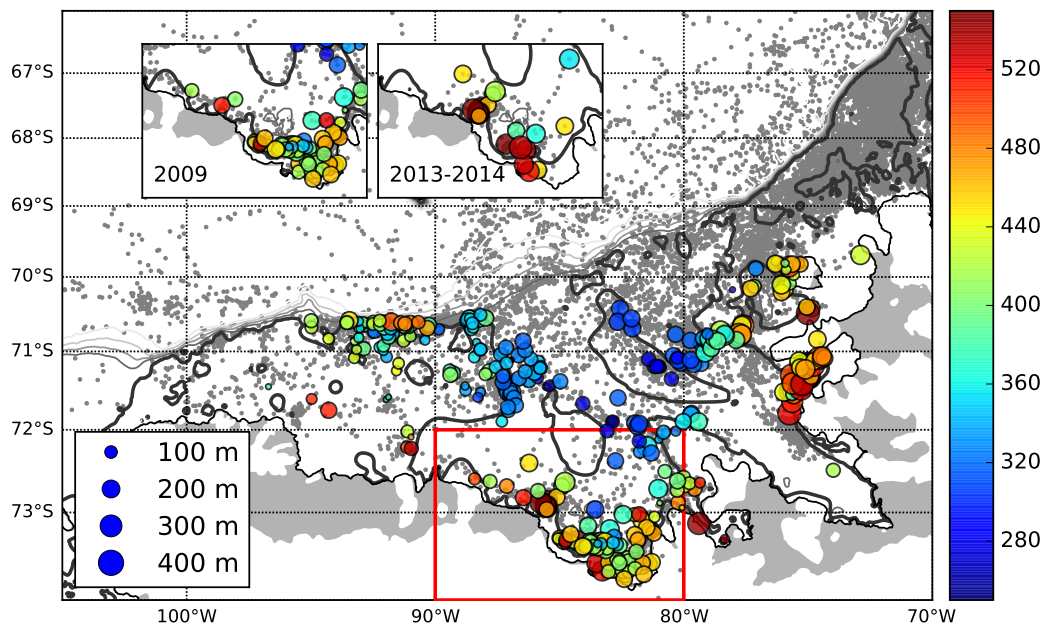


Figure 5.4: Map of all casts that do (color) and do not (grey) fall within the Gade envelope; see Appendix A for Gade envelope criteria. Shallow casts are removed from Gade envelope analysis. The color indicates the mean meltwater mixture layer depth (m), and the sizes of the circles show the meltwater mixture layer thickness. The inserts show the Eltanin Bay region (red box) in 2009 and winter 2013-2014.

sensitivity analysis to the size of the envelope did not show a qualitative difference in the geographic distribution of the meltwater mixture.

Figure 5.4 shows the locations of all dives that contain a portion of the water column falling within the Gade envelope. These dives are found predominantly west of the Wilkins Ice Shelf, in the Latady Trough, along the western boundary of the BT, along the continental shelf break west of the BT, and in Eltanin Bay. The thickness of this meltwater mixture layer, indicated by symbol size in Figure 5.4, is typically between 100 and 200 m. The mean depth of that layer, indicated by colors in Figure 5.4, varies between 250 and 550 m. The deepest meltwater layer is found near the coast, adjacent to the Wilkins Ice Shelf and in the Eltanin Bay (Figure 5.4). The meltwater mixture, which occupies a range of densities between 27.9 to 28.1 kg m⁻³ (Figure S2), gradually shoals as it extends towards the shelf break along the western side of the troughs. This mixture is then found at progressively deeper depths moving to the west along the continental slope west of the BT.

5.5 Discussion

The high-density of seal data allows detailed observations of the circulation and water mass structure over the entire continental shelf of the BS; we focus on characteristics in the BT, the main shelf break canyon in the western BS [123].

Multiple synoptic sections across the shelf break indicate the presence of a shelf break current. The resolution of the seal data is relatively coarse compared to the typical scale of the ASC, which is often comparable to the Rossby radius of deformation, ~ 10 km. Nevertheless, the water mass distribution is indicative of a coherent ASC that is at least partially effective in separating offshore and onshore water. This is supported by Figures 5.2b,c,e and Figure 5.3a, which show that the offshore θ_{max} is at depths shallower than the continental shelf. Yet, water over the shelf is always modified from the offshore CDW properties. This modification is indicative of the Antarctic Slope Front (ASF) [113], which may indicate that the ASC is not limited to the “downstream” (western) side of the BT. This is consistent with the hydrographic sections shown by Talbot [124] and Jenkins & Jacobs [107].

The seal data moves the eastern-most observation of the ASC/ASF system from the Amundsen Sea, e.g. [102], into the BS, suggesting that the origin lies closer to the West Antarctic Peninsula than previously suggested. Unlike in the Ross or Weddell Seas, where the ASC arises due to persistent along-slope easterly winds [125], in the BS a low pressure system centered at 83°W generates predominantly southerly winds west of the BT [112]. Therefore other mechanisms may give rise to this frontal structure, including frictional processes [126], the effects of tides [127], and eddy-induced transport of CDW onto the continental shelf [128].

Onshore of the shelf-break, the appearance of the warmest waters along the eastern boundary of the BT points to the importance of the trough in generating an on-shore heat flux. Two-dimensional idealizations of the overturning circulation have been used to suggest the importance of an eddy transport of heat and mass over the continental slope and shelf in the Weddell Sea [128]. However, a closed, two-dimensional overturning circulation in the BS is likely an overly simplified picture in the absence of a deep outflow of AABW.

At 72°S , θ_{max} differs as much as 0.2°C across the trough (Figure 5.3c). This difference is reduced to 0.05°C near the coast, where water warmer than 1.2°C is no longer detected (Figure 5.3e, f). This pattern is consistent with a cyclonic circulation, confined to narrow boundary currents. Warm and salty mCDW enters the BT via the eastern boundary, where it entrains the cold and fresher water, then

exits via the western boundary. Although modification could occur due to ice shelf meltwater, sea ice formation, or vertical mixing with Winter Water (WW) above the thermocline, our observations show that the most intense modification occurs below WW near the coast. Therefore, meltwater makes the greatest contribution to modification in the BT. A careful examination of the vertical distribution of meltwater mixture shows that the θ_{min} of the WW layer is always more than 100 m above the upper boundary of the meltwater layer; the mean separation is 206 m (Figure S3). Sea ice formation is another potential contributor to water mass modification, however, Talbot [124] showed that winter formation of sea ice in the Bellingshausen Sea does not produce water dense enough to sink beneath the intruding CDW.

A striking feature of Figure 5.4 is that in addition to the near-coast profiles containing deep and thick meltwater layers, the highest density of meltwater away from the coast is confined to the western boundaries of the troughs. In particular, a pathway along the western side of the BT, starting at 72°S, flows towards the shelf break and then extends west as far as 95°W. Moving along this pathway, the meltwater mixture becomes deeper, especially upon leaving the BT. This may indicate an offshore export of the meltwater due to bottom Ekman layer dynamics [126]. We acknowledge that the distribution of the observations varies from year to year (see Figure 5.1), although there are regions that contain data from more than one year. This inhomogeneous sampling could contribute to the observed meltwater distribution in Figure 5.4 if there is interannual variability in meltwater concentrations.

Identifying the exact source of meltwater is beyond the scope of this paper, however, the meltwater mixture distributions suggest possible sources of ice shelf meltwater in this region. Section (e) of Figure 5.3 sits in front of Venable Ice Shelf and is a source of meltwater as indicated in Figure 5.4. Preliminary estimation suggests the highest meltwater fraction occurs in front of Venable Ice Shelf as well (not shown). The section near the coast in Eltanin Bay (Figure 5.3f) also shows a large proportion of meltwater. This meltwater could originate from the Venable Ice Shelf since the easternmost extent of this ice shelf lies to the east of a ridge that defines the northwestern boundary of the deep Eltanin Bay. Additionally, a westward coastal current may carry meltwater from ice shelves east of BT to Eltanin Bay [129].

The non-uniform sampling by the seals between different years makes it difficult to infer trends in meltwater discharge rates. However, near the coast temporal variability is observed with a deeper and thicker meltwater layer in 2013-2014, as

compared to 2009 (Figure 5.4 inserts). Away from the coast, the meltwater layer becomes shallower within the BT, most likely due to mixing with overlying waters. The deepest meltwater at the shelf break, west of 90°W, all came from a single year, 2010. During 2010 there were no near-coast profiles collected by the seals, therefore, we are unable to document whether this corresponds to interannual variability in meltwater discharge rates.

5.6 Conclusions

Nearly 20,000 hydrographic profiles from instrumented seals collected between 2007 and 2014 were analyzed to highlight spatial patterns in circulation pathways and meltwater contributions in the western Bellingshausen Sea. Warm modified Circumpolar Deep Water (mCDW) 3°C above the freezing point is found on the continental shelf and extends to the coast in a narrow eastern boundary current, accompanied by cooling and freshening of the temperature and salinity maxima, respectively. Western boundary currents in troughs entrain ice-shelf meltwater near the coast and carry the mCDW-meltwater mixture to the shelf break. This comprehensive data set highlights the importance of boundary currents in (i) modifying CDW across an established shelf-break frontal system, (ii) delivering warm water towards the major ice shelves, and (iii) exporting meltwater mixtures towards the open ocean and potentially westward towards the Amundsen Sea within the Antarctic Slope Current. The distribution of meltwater mixtures supports the high basal melt rate and thinning of Venable Ice Shelf detected by satellite observations, but more importantly, emphasizes the need to monitor finescale ocean circulation features to understand future changes in the West Antarctic Ice Sheet.

[Supporting Information of this article can be found at <https://agupubs.onlinelibrary.wiley.com/doi/abs/10.1002/2016GL068998>.]

Chapter 6

CONCLUSIONS

This thesis explores the dynamics of polar clouds using a large eddy simulation model.

Chapter 2 focuses on a simple Arctic boundary layer cloud case ISDAC, where a persistent stratocumulus was observed over sea ice during polar night. We conducted idealized climate change experiments by varying the boundary layer temperature, cloud-top inversion strength, and free tropospheric relative humidity. The experiments are motivated by the surface intensified warming projected in climate models in the Arctic. We found the condensed water path to increase with boundary layer temperature and free-tropospheric relative humidity, but to decrease with inversion strength. These changes are indicative of a positive longwave cloud feedback at TOA, and the feedback strength depends on the inversion strength. The results simulated by the LES are largely reproduced by a mixed-layer model, and thus we could extend the mixed-layer theory toward explaining BL cloud sensitivities in the high latitudes under suitable conditions.

Chapter 3 further validates the LES model with two Arctic model intercomparison cases. The SHEBA study involves a thin cloud layer with light snow and weak surface fluxes. In the observation, the BL shallows and the cloud thins during the course of 12 hours. The prescribed forcing that warms and moistens the BL results in a thickened cloud in our LES. Although our results are within the LES intercomparison range, the condensed water path is overestimated compared to observations. The cloud in M-PACE is thicker than in SHEBA, and produces a significant amount of snow. Our simulated liquid water path is within the observed range, and our model even outperforms some models with more complex microphysical schemes. The accretion of snow, a process that is not active in SHEBA and ISDAC, is active during M-PACE. Overall, the LES is able to capture the main features of Arctic BL clouds, though further development on the microphysical scheme is needed to better simulate the vertical structure of ice condensates.

Chapter 4 presents a novel study using an idealized GCM to provide large-scale forcing for the LES in the polar region. Both the GCM and LES have a seasonal cycle and a simple thermodynamic sea ice model. The forcing from the GCM output

includes horizontal and vertical advection of temperature and specific humidity, as well as surface fluxes. In the reference climate, our LES simulates a seasonal cycle of liquid cloud that resembles observations. Cloud liquid water maximum is found near the surface during summer and autumn, and liquid cloud persists throughout the year. In the warm climate, the summer-autumn liquid layer is weakened and elevated, and there is a significant increase of liquid water during spring and winter in the BL. Offline estimation of cloud radiative effects suggests a positive cloud radiative feedback which is dominated by longwave feedback. The feedback parameter is larger than what modern GCMs suggest, and thus the difference in the feedback strengths could depend on processes that are not represented in our setup.

The natural next step is to conduct GCM forcing experiments with cloud radiative feedbacks in both GCM and LES, so that the cloud feedback strength will have more real-world relevance. For instance, longwave cooling at the cloud top is needed to maintain a strong cloud-top temperature inversion, which is not found in our LES results. The shortwave masking effect of clouds over sea ice may significantly alter the surface energy budget during spring, summer, and autumn. A version of the idealized GCM with clouds and more advanced radiative transfer is under development. This will allow us to include cloud-radiation interactions in the modeling framework in the future.

Chapter 5 addresses a different aspect of the polar climate. We conducted an oceanic study on the circulation on the continental shelf of western Bellingshausen Sea, Antarctica. We use temperature and salinity profiles collected by instrumented seals in the Southern Ocean to highlight the circulation pathways and meltwater contributions near ice shelves that experience high basal melt rates. We found that the western boundary currents entrain ice-shelf meltwater near the coast, and carry it from the troughs to the shelf break. It provides observational evidence of rapid oceanic changes that contribute to the mass loss of the West Antarctic Ice Sheet.

BIBLIOGRAPHY

1. Schneider, T. & Held, I. M. Discriminants of Twentieth-Century Changes in Earth Surface Temperatures. *Journal of Climate* **14**, 249–254 (2001).
2. Serreze, M. C., Barrett, A. P. & Stroeve, J. Recent changes in tropospheric water vapor over the Arctic as assessed from radiosondes and atmospheric reanalyses. *Journal of Geophysical Research: Atmospheres* **117**. D10104. ISSN: 2156-2202. doi:[10.1029/2011JD017421](https://doi.org/10.1029/2011JD017421). <<http://dx.doi.org/10.1029/2011JD017421>> (2012).
3. Cohen, J. *et al.* Recent Arctic amplification and extreme mid-latitude weather. *Nature Geoscience* **7**, 627–637 (2014).
4. Stroeve, J. C. *et al.* The Arctic’s rapidly shrinking sea ice cover: a research synthesis. *Climatic Change* **110**, 1005–1027. ISSN: 1573-1480 (Feb. 2012).
5. Pritchard, H. D. *et al.* Antarctic ice-sheet loss driven by basal melting of ice shelves. *Nature* **484**, 502–505. ISSN: 0028-0836, 1476-4687 (Apr. 2012).
6. Manabe, S. & Wetherald, R. T. The Effects of Doubling the CO₂ Concentration on the climate of a General Circulation Model. *Journal of the Atmospheric Sciences* **32**, 3–15 (1975).
7. Holland, M. M. & Bitz, C. M. Polar amplification of climate change in coupled models. *Climate Dynamics* **21**, 221–232. ISSN: 1432-0894 (2003).
8. Serreze, M. C. & Barry, R. G. Processes and impacts of Arctic amplification: A research synthesis. en. *Global and Planetary Change* **77**, 85–96. ISSN: 09218181 (May 2011).
9. Kay, J. E. & L’Ecuyer, T. Observational constraints on Arctic Ocean clouds and radiative fluxes during the early 21st century. *Journal of Geophysical Research: Atmospheres* **118**, 7219–7236. ISSN: 2169-8996 (2013).
10. Blossey, P. N. *et al.* Marine low cloud sensitivity to an idealized climate change: The CGILS LES intercomparison. *Journal of Advances in Modeling Earth Systems* **5**, 234–258 (2013).
11. Bretherton, C. S., Blossey, P. N. & Jones, C. R. Mechanisms of marine low cloud sensitivity to idealized climate perturbations: A single-LES exploration extending the CGILS cases: LES OF BOUNDARY-LAYER CLOUD FEEDBACK. en. *Journal of Advances in Modeling Earth Systems* **5**, 316–337. ISSN: 19422466 (June 2013).
12. Tan, Z., Schneider, T., Teixeira, J. & Pressel, K. G. Large-eddy simulation of subtropical cloud-topped boundary layers: 1. A forcing framework with closed surface energy balance. *Journal of Advances in Modeling Earth Systems*. ISSN: 1942-2466. doi:[10.1002/2016MS000655](https://doi.org/10.1002/2016MS000655). <<http://dx.doi.org/10.1002/2016MS000655>> (2016).

13. Tan, Z., Schneider, T., Teixeira, J. & Pressel, K. G. Large-eddy simulation of subtropical cloud-topped boundary layers: 2. Cloud response to climate change. *Journal of Advances in Modeling Earth Systems*. ISSN: 1942-2466. doi:[10.1002/2016MS000804](https://doi.org/10.1002/2016MS000804). <<http://dx.doi.org/10.1002/2016MS000804>> (2017).
14. Lilly, D. K. Models of cloud-topped mixed layers under a strong inversion. *Quarterly Journal of the Royal Meteorological Society* **94**, 292–309. ISSN: 1477-870X (1968).
15. Pressel, K. G., Kaul, C. M., Schneider, T., Tan, Z. & Mishra, S. Large-eddy simulation in an anelastic framework with closed water and entropy balances. *Journal of Advances in Modeling Earth Systems*. doi:[10.1002/2015MS000496](https://doi.org/10.1002/2015MS000496). <<http://dx.doi.org/10.1002/2015MS000496>> (2015).
16. Curry, J. A., Schramm, J. L., Rossow, W. B. & Randall, D. Overview of Arctic Cloud and Radiation Characteristics. *Journal of Climate* **9**, 1731–1764 (1996).
17. Tjernström, M. & Graversen, R. G. The vertical structure of the lower Arctic troposphere analysed from observations and the ERA-40 reanalysis. *Quarterly Journal of the Royal Meteorological Society* **135**, 431–443. ISSN: 1477-870X (2009).
18. Wang, X. & Key, J. R. Arctic Surface, Cloud, and Radiation Properties Based on the AVHRR Polar Pathfinder Dataset. Part II: Recent Trends. *Journal of Climate* **18**, 2575–2593 (2005).
19. Intrieri, J. M., Shupe, M. D., Uttal, T. & McCarty, B. J. An annual cycle of Arctic cloud characteristics observed by radar and lidar at SHEBA. *Journal of Geophysical Research: Oceans* **107**, SHE 5-1–SHE 5-15. ISSN: 2156-2202 (2002).
20. Cox, C. J. *et al.* The Role of Springtime Arctic Clouds in Determining Autumn Sea Ice Extent. *Journal of Climate* **29**, 6581–6596 (2016).
21. Screen, J. A., Deser, C. & Simmonds, I. Local and remote controls on observed Arctic warming. *Geophysical Research Letters* **39**. L10709. ISSN: 1944-8007. doi:[10.1029/2012GL051598](https://doi.org/10.1029/2012GL051598) (2012).
22. Serreze, M. C., Barrett, A. P., Stroeve, J. C., Kindig, D. N. & Holland, M. M. The emergence of surface-based Arctic amplification. *The Cryosphere* **3**, 11–19 (2009).
23. Sherwood, S. C. *et al.* Relative humidity changes in a warmer climate. *Journal of Geophysical Research: Atmospheres* **115**. D09104. ISSN: 2156-2202. doi:[10.1029/2009JD012585](https://doi.org/10.1029/2009JD012585). <<http://dx.doi.org/10.1029/2009JD012585>> (2010).

24. Wetherald, R. T. & Manabe, S. The effects of changing the solar constant on the climate of a general circulation model. *J. Atmos. Sci.* **32**, 2044–2059 (1975).
25. Graverson, R. G. & Wang, M. Polar amplification in a coupled climate model with locked albedo. *Climate Dynamics* **33**, 629–643. ISSN: 1432-0894 (2009).
26. Pithan, F. & Mauritsen, T. Arctic amplification dominated by temperature feedbacks in contemporary climate models. *Nature Geoscience* **7**, 181–184 (2014).
27. Kay, J. E. *et al.* Recent Advances in Arctic Cloud and Climate Research. *Current Climate Change Reports* **2**, 159–169. ISSN: 2198-6061 (2016).
28. Vavrus, S., Waliser, D., Schweiger, A. & Francis, J. Simulations of 20th and 21st century Arctic cloud amount in the global climate models assessed in the IPCC AR4. *Climate Dynamics* **33**, 1099. ISSN: 1432-0894 (2009).
29. Karlsson, J. & Svensson, G. Consequences of poor representation of Arctic sea-ice albedo and cloud-radiation interactions in the CMIP5 model ensemble. *Geophysical Research Letters* **40**, 4374–4379. ISSN: 1944-8007 (2013).
30. Savre, J., Ekman, A. M. L., Svensson, G. & Tjernström, M. Large-eddy simulations of an Arctic mixed-phase stratiform cloud observed during ISDAC: sensitivity to moisture aloft, surface fluxes and large-scale forcing. *Quarterly Journal of the Royal Meteorological Society* **141**, 1177–1190. ISSN: 1477-870X (2015).
31. Solomon, A. *et al.* The Sensitivity of Springtime Arctic Mixed-Phase Stratocumulus Clouds to Surface-Layer and Cloud-Top Inversion-Layer Moisture Sources. *Journal of the Atmospheric Sciences* **71**, 574–595 (2014).
32. Ovchinnikov, M. *et al.* Intercomparison of large-eddy simulations of Arctic mixed-phase clouds: Importance of ice size distribution assumptions. *Journal of Advances in Modeling Earth Systems* **6**, 223–248. ISSN: 1942-2466 (2014).
33. Dal Gesso, S., Siebesma, A. P., de Roode, S. R. & van Wessem, J. M. A mixed-layer model perspective on stratocumulus steady states in a perturbed climate. *Quarterly Journal of the Royal Meteorological Society* **140**, 2119–2131. ISSN: 1477-870X (2014).
34. Van der Dussen, J. J., de Roode, S. R., Dal Gesso, S. & Siebesma, A. P. An LES model study of the influence of the free tropospheric thermodynamic conditions on the stratocumulus response to a climate perturbation. *Journal of Advances in Modeling Earth Systems* **7**, 670–691. ISSN: 1942-2466 (2015).
35. Bretherton, C. S. & Wyant, M. C. Moisture Transport, Lower-Tropospheric Stability, and Decoupling of Cloud-Topped Boundary Layers. *Journal of the Atmospheric Sciences* **54**, 148–167 (1997).

36. De Roode, S. R. *et al.* A mixed-layer model study of the stratocumulus response to changes in large-scale conditions. *Journal of Advances in Modeling Earth Systems* **6**, 1256–1270. ISSN: 1942-2466 (2014).
37. Pressel, K. G., Mishra, S., Schneider, T., Kaul, C. M. & Tan, Z. Numerics and subgrid-scale modeling in large eddy simulations of stratocumulus clouds. *Journal of Advances in Modeling Earth Systems*. ISSN: 1942-2466. doi:[10.1002/2016MS000778](https://doi.org/10.1002/2016MS000778). <<http://dx.doi.org/10.1002/2016MS000778>> (2017).
38. Kaul, C. M., Teixeira, J. & Suzuki, K. Sensitivities in Large-Eddy Simulations of Mixed-Phase Arctic Stratocumulus Clouds Using a Simple Microphysics Approach. *Monthly Weather Review* **143**, 4393–4421 (2015).
39. Grabowski, W. W. Toward Cloud Resolving Modeling of Large-Scale Tropical Circulations: A Simple Cloud Microphysics Parameterization. *Journal of the Atmospheric Sciences* **55**, 3283–3298 (1998).
40. De Boer, G., Eloranta, E. W. & Shupe, M. D. Arctic Mixed-Phase Stratiform Cloud Properties from Multiple Years of Surface-Based Measurements at Two High-Latitude Locations. *Journal of the Atmospheric Sciences* **66**, 2874–2887 (2009).
41. Morrison, H., Zuidema, P., McFarquhar, G. M., Bansemer, A. & Heymsfield, A. J. Snow microphysical observations in shallow mixed-phase and deep frontal Arctic cloud systems. *Quarterly Journal of the Royal Meteorological Society* **137**, 1589–1601. ISSN: 1477-870X (2011).
42. Straka, J. M. *Cloud and Precipitation Microphysics: Principles and Parameterizations* doi:[10.1017/CB09780511581168](https://doi.org/10.1017/CB09780511581168) (Cambridge University Press, 2009).
43. Iacono, M. J. *et al.* Radiative forcing by long-lived greenhouse gases: Calculations with the AER radiative transfer models. *Journal of Geophysical Research: Atmospheres* **113**. D13103. ISSN: 2156-2202. doi:[10.1029/2008JD009944](https://doi.org/10.1029/2008JD009944). <<http://dx.doi.org/10.1029/2008JD009944>> (2008).
44. Martin, G. M., Johnson, D. W. & Spice, A. The Measurement and Parameterization of Effective Radius of Droplets in Warm Stratocumulus Clouds. *Journal of the Atmospheric Sciences* **51**, 1823–1842 (1994).
45. Boudala, F. S., Isaac, G. A., Fu, Q. & Cober, S. G. Parameterization of effective ice particle size for high-latitude clouds. *International Journal of Climatology* **22**, 1267–1284. ISSN: 1097-0088 (2002).
46. Mellado, J. P. Cloud-Top Entrainment in Stratocumulus Clouds. *Annual Review of Fluid Mechanics* **49**, 145–169 (2017).

47. Moeng, C.-H. Entrainment Rate, Cloud Fraction, and Liquid Water Path of PBL Stratocumulus Clouds. *Journal of the Atmospheric Sciences* **57**, 3627–3643 (2000).
48. Moeng, C.-H., Sullivan, P. P. & Stevens, B. Including Radiative Effects in an Entrainment Rate Formula for Buoyancy-Driven PBLs. *Journal of the Atmospheric Sciences* **56**, 1031–1049 (1999).
49. Stevens, B. Bulk boundary-layer concepts for simplified models of tropical dynamics. *Theor. Comput. Fluid Dyn.* **20**, 279–304 (2006).
50. Tripoli, G. J. & Cotton, W. R. The Use of Ice-Liquid Water Potential Temperature as a Thermodynamic Variable In Deep Atmospheric Models. *Monthly Weather Review* **109**, 1094–1102 (1981).
51. Klein, S. A. & Hartmann, D. L. The Seasonal Cycle of Low Stratiform Clouds. *Journal of Climate* **6**, 1587–1606 (1993).
52. McFarquhar, G. M. *et al.* Indirect and Semi-direct Aerosol Campaign. *Bulletin of the American Meteorological Society* **92**, 183–201 (2011).
53. Fan, J. *et al.* Representation of Arctic mixed-phase clouds and the Wegener-Bergeron-Findeisen process in climate models: Perspectives from a cloud-resolving study. *Journal of Geophysical Research: Atmospheres* **116**. D00T07. ISSN: 2156-2202. doi:[10.1029/2010JD015375](https://doi.org/10.1029/2010JD015375). <<http://dx.doi.org/10.1029/2010JD015375>> (2011).
54. Savre, J., Ekman, A. M. L. & Svensson, G. Technical note: Introduction to MIMICA, a large-eddy simulation solver for cloudy planetary boundary layers. *Journal of Advances in Modeling Earth Systems* **6**, 630–649. ISSN: 1942-2466 (2014).
55. Fridlind, A. M. & Ackerman, A. S. in *Mixed-Phase Clouds* (ed Andronache, C.) 153–183 (Elsevier, 2018). ISBN: 978-0-12-810549-8. doi:[10.1016/B978-0-12-810549-8.00007-6](https://doi.org/10.1016/B978-0-12-810549-8.00007-6). <<https://www.sciencedirect.com/science/article/pii/B9780128105498000076>>.
56. Stull, R. B. in *An Introduction to Boundary Layer Meteorology* (ed Stull, R. B.) DOI: 10.1007/978-94-009-3027-8_13, 545–585 (Springer Netherlands, Dordrecht, 1988). ISBN: 978-94-009-3027-8. <https://doi.org/10.1007/978-94-009-3027-8_13>.
57. Sedlar, J. & Tjernström, M. Stratiform Cloud—Inversion Characterization During the Arctic Melt Season. *Boundary-Layer Meteorology* **132**, 455–474. ISSN: 1573-1472 (2009).
58. Rieck, M., Nuijens, L. & Stevens, B. Marine Boundary Layer Cloud Feedbacks in a Constant Relative Humidity Atmosphere. *Journal of the Atmospheric Sciences* **69**, 2538–2550 (2012).
59. Deardorff, J. W. Cloud Top Entrainment Instability. *Journal of the Atmospheric Sciences* **37**, 131–147 (1980).

60. Wood, R. Stratocumulus Clouds. *Monthly Weather Review* **140**, 2373–2423 (2012).
61. Morrison, H. *et al.* Intercomparison of model simulations of mixed-phase clouds observed during the ARM Mixed-Phase Arctic Cloud Experiment. II: Multilayer cloud. en. *Quarterly Journal of the Royal Meteorological Society* **135**, 1003–1019. ISSN: 00359009, 1477870X (Apr. 2009).
62. Klein, S. A. *et al.* Intercomparison of model simulations of mixed-phase clouds observed during the ARM Mixed-Phase Arctic Cloud Experiment. I: single-layer cloud. en. *Quarterly Journal of the Royal Meteorological Society* **135**, 979–1002. ISSN: 00359009, 1477870X (Apr. 2009).
63. Manabe, S. & Stouffer, R. J. Sensitivity of a global climate model to an increase of CO₂ concentration in the atmosphere. *Journal of Geophysical Research: Oceans* **85**, 5529–5554. ISSN: 2156-2202 (1980).
64. Stroeve, J., Holland, M. M., Meier, W., Scambos, T. & Serreze, M. Arctic sea ice decline: Faster than forecast: ARCTIC ICE LOSS-FASTER THAN FORECAST. en. *Geophysical Research Letters* **34**. ISSN: 00948276. doi:10.1029/2007GL029703. <<http://doi.wiley.com/10.1029/2007GL029703>> (visited on 03/16/2018) (May 2007).
65. Winton, M. Does the Arctic sea ice have a tipping point? en. *Geophysical Research Letters* **33**. ISSN: 0094-8276. doi:10.1029/2006GL028017. <<http://doi.wiley.com/10.1029/2006GL028017>> (visited on 04/07/2018) (Dec. 2006).
66. Beesley, J. A. & Moritz, R. E. Toward an Explanation of the Annual Cycle of Cloudiness over the Arctic Ocean. en. *Journal of Climate* **12**, 395–415. ISSN: 0894-8755, 1520-0442 (Feb. 1999).
67. Cesana, G., Kay, J. E., Chepfer, H., English, J. M. & de Boer, G. Ubiquitous low-level liquid-containing Arctic clouds: New observations and climate model constraints from CALIPSO-GOCCP. en. *Geophysical Research Letters* **39**. ISSN: 00948276. doi:10.1029/2012GL053385. <<http://doi.wiley.com/10.1029/2012GL053385>> (visited on 12/21/2017) (Oct. 2012).
68. Wall, C. J., Kohyama, T. & Hartmann, D. L. Low-Cloud, Boundary Layer, and Sea Ice Interactions over the Southern Ocean during Winter. en. *Journal of Climate* **30**, 4857–4871. ISSN: 0894-8755, 1520-0442 (July 2017).
69. Kay, J. E. & Gettelman, A. Cloud influence on and response to seasonal Arctic sea ice loss. en. *Journal of Geophysical Research* **114**. ISSN: 0148-0227. doi:10.1029/2009JD011773. <<http://doi.wiley.com/10.1029/2009JD011773>> (visited on 12/21/2017) (Sept. 2009).

70. Morrison, A. L., Kay, J. E., Chepfer, H., Guzman, R. & Yettella, V. Isolating the Liquid Cloud Response to Recent Arctic Sea Ice Variability Using Spaceborne Lidar Observations. en. *Journal of Geophysical Research: Atmospheres* **123**, 473–490. ISSN: 2169897X (Jan. 2018).
71. Zelinka, M. D. & Hartmann, D. L. Climate Feedbacks and Their Implications for Poleward Energy Flux Changes in a Warming Climate. en. *Journal of Climate* **25**, 608–624. ISSN: 0894-8755, 1520-0442 (Jan. 2012).
72. Pithan, F., Medeiros, B. & Mauritsen, T. Mixed-phase clouds cause climate model biases in Arctic wintertime temperature inversions. *Climate Dynamics* **43**, 289–303. ISSN: 1432-0894 (2014).
73. Abbot, D. S. & Tziperman, E. A high-latitude convective cloud feedback and equable climates. en. *Quarterly Journal of the Royal Meteorological Society* **134**, 165–185. ISSN: 00359009, 1477870X (Jan. 2008).
74. Abbot, D. S. & Tziperman, E. Sea ice, high-latitude convection, and equable climates. en. *Geophysical Research Letters* **35**. ISSN: 0094-8276. doi:[10.1029/2007GL032286](https://doi.org/10.1029/2007GL032286). <<http://doi.wiley.com/10.1029/2007GL032286>> (visited on 12/21/2017) (Feb. 2008).
75. Abbot, D. S., Walker, C. C. & Tziperman, E. Can a Convective Cloud Feedback Help to Eliminate Winter Sea Ice at High CO₂ Concentrations? en. *Journal of Climate* **22**, 5719–5731. ISSN: 0894-8755, 1520-0442 (Nov. 2009).
76. Abbot, D. S., Huber, M., Bousquet, G. & Walker, C. C. High-CO₂ cloud radiative forcing feedback over both land and ocean in a global climate model. en. *Geophysical Research Letters* **36**. ISSN: 0094-8276. doi:[10.1029/2008GL036703](https://doi.org/10.1029/2008GL036703). <<http://doi.wiley.com/10.1029/2008GL036703>> (visited on 12/21/2017) (Mar. 2009).
77. Brient, F. *et al.* Shallowness of tropical low clouds as a predictor of climate models' response to warming. en. *Climate Dynamics* **47**, 433–449. ISSN: 0930-7575, 1432-0894 (July 2016).
78. Frierson, D. M. W., Held, I. M. & Zurita-Gotor, P. A gray-radiation aquaplanet moist GCM. Part I: Static stability and eddy scale. en. *Journal of the Atmospheric Sciences* **63**, 2548–2566. ISSN: 0022-4928, 1520-0469 (Oct. 2006).
79. Frierson, D. M. W., Held, I. M. & Zurita-Gotor, P. A gray-radiation aquaplanet moist GCM. Part II: Energy transports in altered climates. en. *Journal of the Atmospheric Sciences* **64**, 1680–1693. ISSN: 0022-4928, 1520-0469 (May 2007).
80. O’Gorman, P. A. & Schneider, T. The hydrological cycle over a wide range of climates simulated with an idealized GCM. en. *Journal of Climate* **21**, 3815–3832. ISSN: 0894-8755, 1520-0442 (Aug. 2008).

81. Levine, X. J. & Schneider, T. Response of the Hadley Circulation to Climate Change in an Aquaplanet GCM Coupled to a Simple Representation of Ocean Heat Transport. en. *Journal of the Atmospheric Sciences* **68**, 769–783. ISSN: 0022-4928, 1520-0469 (Apr. 2011).
82. Kaspi, Y. & Schneider, T. The Role of Stationary Eddies in Shaping Midlatitude Storm Tracks. en. *Journal of the Atmospheric Sciences* **70**, 2596–2613. ISSN: 0022-4928, 1520-0469 (Aug. 2013).
83. Merlis, T. M. & Schneider, T. Changes in Zonal Surface Temperature Gradients and Walker Circulations in a Wide Range of Climates. en. *Journal of Climate* **24**, 4757–4768. ISSN: 0894-8755, 1520-0442 (Sept. 2011).
84. Bordoni, S. & Schneider, T. Monsoons as eddy-mediated regime transitions of the tropical overturning circulation. en. *Nature Geoscience* **1**, 515–519. ISSN: 1752-0894, 1752-0908 (Aug. 2008).
85. Semtner, A. J. A Model for the Thermodynamic Growth of Sea Ice in Numerical Investigations of Climate. en. *Journal of Physical Oceanography* **6**, 379–389. ISSN: 0022-3670, 1520-0485 (May 1976).
86. Randall, D. A. & Cripe, D. G. Alternative methods for specification of observed forcing in single-column models and cloud system models. en. *Journal of Geophysical Research: Atmospheres* **104**, 24527–24545. ISSN: 01480227 (Oct. 1999).
87. Sekhon, R. S. & Srivastava, R. C. Snow Size Spectra and Radar Reflectivity. en. *Journal of the Atmospheric Sciences* **27**, 299–307. ISSN: 0022-4928, 1520-0469 (Mar. 1970).
88. Persson, P. O. G. Measurements near the Atmospheric Surface Flux Group tower at SHEBA: Near-surface conditions and surface energy budget. en. *Journal of Geophysical Research* **107**. ISSN: 0148-0227. doi:[10.1029/2000JC000705](https://doi.org/10.1029/2000JC000705). <<http://doi.wiley.com/10.1029/2000JC000705>> (visited on 12/21/2017) (2002).
89. Chepfer, H. *et al.* Use of CALIPSO lidar observations to evaluate the cloudiness simulated by a climate model. en. *Geophysical Research Letters* **35**. ISSN: 0094-8276. doi:[10.1029/2008GL034207](https://doi.org/10.1029/2008GL034207). <<http://doi.wiley.com/10.1029/2008GL034207>> (visited on 04/17/2018) (Aug. 2008).
90. Lenaerts, J. T. M., VanTricht, K., Lhermitte, S. & L'Ecuyer, T. S. Polar clouds and radiation in satellite observations, reanalyses, and climate models. en. *Geophysical Research Letters* **44**, 3355–3364. ISSN: 00948276 (Apr. 2017).
91. Sherwood, S. C., Bony, S. & Dufresne, J.-L. Spread in model climate sensitivity traced to atmospheric convective mixing. en. *Nature* **505**, 37–42. ISSN: 0028-0836, 1476-4687 (Jan. 2014).
92. Gille, S. T. Decadal-scale temperature trends in the Southern Hemisphere ocean. *J. Clim.* **21**, 4749–4765 (2008).

93. Rintoul, S. R. Rapid freshening of Antarctic Bottom Water formed in the Indian and Pacific oceans. *Geophys. Res. Lett.* **34**. L06606. doi:[10.1029/2006GL028550](https://doi.org/10.1029/2006GL028550) (2007).
94. Aoki, S., Rintoul, S. R., Ushio, S., Watanabe, S. & Bindoff, N. L. Freshening of the Adélie Land Bottom Water near 140°E. *Geophys. Res. Lett.* **32**. L23601. doi:[10.1029/2005GL024246](https://doi.org/10.1029/2005GL024246) (2005).
95. Purkey, S. G. & Johnson, G. C. Antarctic Bottom Water Warming and Freshening: Contributions to Sea Level Rise, Ocean Freshwater Budgets, and Global Heat Gain. *J. Clim.* **26**, 6105–6122 (2015/04/12 2013).
96. Pritchard, H. *et al.* Antarctic ice-sheet loss driven by basal melting of ice shelves. *Nature* **484**, 502–505 (2012).
97. Rignot, E., Jacobs, S., Mouginot, J. & Scheuchl, B. Ice-shelf melting around Antarctica. *Science* **341**, 266–270 (2013).
98. Wouters, B. *et al.* Dynamic thinning of glaciers on the Southern Antarctic Peninsula. *Science* **348**, 899–903 (2015).
99. Arneborg, L., Wåhlin, A., Björk, G., Liljebladh, B. & Orsi, A. Persistent inflow of warm water onto the central Amundsen shelf. *Nat. Geosci.* **5**, 876–880 (2012).
100. Wåhlin, A. *et al.* Variability of Warm Deep Water Inflow in a Submarine Trough on the Amundsen Sea Shelf. *J. Phys. Oceanogr.* **43**, 2054–2070 (2013).
101. Walker, D. P., Jenkins, A., Assmann, K. M., Shoosmith, D. R. & Brandon, M. A. Oceanographic observations at the shelf break of the Amundsen Sea, Antarctica. *J. Geophys. Res.* **118**, 2906–2918 (2013).
102. Wåhlin, A., Yuan, X., Björk, G. & Nohr, C. Inflow of Warm Circumpolar Deep Water in the Central Amundsen Shelf. *J. Phys. Oceanogr.* **40**, 1427–1434 (2010).
103. Nakayama, Y., Schröder, M. & Hellmer, H. H. From circumpolar deep water to the glacial meltwater plume on the eastern Amundsen Shelf. *Deep Sea Res. Part I* **77**, 50–62 (2013).
104. Jenkins, A. The impact of melting ice on ocean waters. *J. Phys. Oceanogr.* **29**, 2370–2381 (1999).
105. Dutrieux, P. *et al.* Strong Sensitivity of Pine Island Ice-Shelf Melting to Climatic Variability. *Science* **343**, 174–178 (2014).
106. Padman, L. *et al.* Oceanic controls on the mass balance of Wilkins Ice Shelf, Antarctica. *J. Geophys. Res.* **117**. C01010. doi:[10.1029/2011JC007301](https://doi.org/10.1029/2011JC007301) (2012).

107. Jenkins, A. & Jacobs, S. Circulation and melting beneath George VI Ice Shelf, Antarctica. *J. Geophys. Res.* **113**. C04013. doi:[10.1029/2007JC004449](https://doi.org/10.1029/2007JC004449) (2008).
108. Schmidtko, S., Heywood, K. J., Thompson, A. F. & Aoki, S. Multidecadal warming of Antarctic waters. *Science* **346**, 1227–1231 (2014).
109. Paolo, F. S., Fricker, H. A. & Padman, L. Volume loss from Antarctic ice shelves is accelerating. *Science* **348**, 327–331 (2015).
110. Jacobs, S. S., Hellmer, H. H. & Jenkins, A. Antarctic ice sheet melting in the Southeast Pacific. *Geophys. Res. Lett.* **23**, 957–960 (1996).
111. Nakayama, Y., Timmermann, R., Rodehacke, C. B., Schröder, M. & Hellmer, H. H. Modeling the spreading of glacial meltwater from the Amundsen and Bellingshausen Seas. *Geophys. Res. Lett.* **41**, 7942–7949 (2014).
112. Holland, P. R., Jenkins, A. & Holland, D. M. Ice and ocean processes in the Bellingshausen Sea, Antarctica. *J. Geophys. Res.* **115**. C05020. doi:[10.1029/2008JC005219](https://doi.org/10.1029/2008JC005219) (2010).
113. Jacobs, S. S. On the nature and significance of the Antarctic Slope Front. *Mar. Chem.* **35**, 9–24 (1991).
114. Boehme, L. *et al.* Technical Note: Animal-borne CTD-Satellite Relay Data Loggers for real-time oceanographic data collection. *Ocean Science* **5**, 685–695 (2009).
115. Roquet, F. *et al.* Estimates of the Southern Ocean general circulation improved by animal-borne instruments. *Geophys. Res. Lett.* **40**, 6176–6180 (2013).
116. Arndt, J. E. *et al.* The International Bathymetric Chart of the Southern Ocean (IBCSO) Version 1.0—A new bathymetric compilation covering circum-Antarctic waters. *Geophys. Res. Lett.* **40**, 3111–3117 (2013).
117. Orsi, A. H., Whitworth III, T. & Nowlin Jr, W. D. On the meridional extent and fronts of the Antarctic Circumpolar Current. *Deep Sea Res. Part I* **42**, 641–673 (1995).
118. Roquet, F. *et al.* Delayed-Mode Calibration of Hydrographic Data Obtained from Animal-Borne Satellite Relay Data Loggers. *J. Atm. Ocean. Tech.* **28**, 787–801 (2011).
119. Costa, D. P., Klinck, J. M., Hofmann, E. E., Dinniman, M. S. & Burns, J. M. Upper ocean variability in west Antarctic Peninsula continental shelf waters as measured using instrumented seals. *Deep Sea Res. Part II* **55**, 323–337 (2008).
120. McIntyre, T. *et al.* Environmental influences on the at-sea behaviour of a major consumer, *Mirounga leonina*, in a rapidly changing environment. *Polar Res.* **33**. 23808. doi:[10.3402/polar.v33.23808](https://doi.org/10.3402/polar.v33.23808) (2014).

121. Whitworth, T., Orsi, A. H., Kim, S.-J., Nowlin, W. D. & Locarnini, R. A. in *Ocean, Ice, and Atmosphere: Interactions at the Antarctic Continental Margin* (eds S. S. Jacobs and R. F. Weiss) 1–27 (American Geophysical Union, Washington, D. C., 1998). doi:[10.1029/AR075p0001](https://doi.org/10.1029/AR075p0001).
122. Gade, H. G. Melting of ice in sea water: A primitive model with application to the Antarctic ice shelf and icebergs. *J. Phys. Oceanogr.* **9**, 189–198 (1979).
123. Graham, A. G., Nitsche, F. & Larter, R. D. An improved bathymetry compilation for the Bellingshausen Sea, Antarctica, to inform ice-sheet and ocean models. *The Cryosphere* **5**, 95–106 (2011).
124. Talbot, M. H. Oceanic environment of George VI ice shelf, Antarctic Peninsula. *Annals of glaciology* **11**, 161–164 (1988).
125. Gill, A. Circulation and bottom water production in the Weddell Sea. *Deep Sea Res.* **20**, 111–140 (1973).
126. Wählin, A. *et al.* Some implications of Ekman layer dynamics for cross-shelf exchange in the Amundsen Sea. *J. Phys. Oceanogr.* **42**, 1461–1474 (2012).
127. Flexas, M. M., Schodlok, M. P., Padman, L., Menemenlis, D. & Orsi, A. H. Role of tides on the formation of the Antarctic Slope Front at the Weddell-Scotia Confluence. *J. Geophys. Res.* **120**, 3658–3680. ISSN: 2169-9291 (2015).
128. Thompson, A. F., Heywood, K. J., Schmidtko, S. & Stewart, A. L. Eddy transport as a key component of the Antarctic overturning circulation. *Nat. Geosci.* **7**, 879–884 (Dec. 2014).
129. Moffat, C., Beardsley, R. C., Owens, B. & Van Lipzig, N. A first description of the Antarctic Peninsula Coastal Current. *Deep Sea Res. Part II* **55**, 277–293 (2008).